Navigating the Landscape of Compactified String Theory with Experimental Data

by

Bob Zheng

A dissertation submitted in partial fulfillment
of the requirements for the degree of
Doctor of Philosophy
(Physics)
in the University of Michigan
2016

Doctoral Committee:

Professor Gordon L. Kane, Chair
Professor Daniel M. Burns Jr.
Professor Henriette Elvang
Professor Aaron T. Pierce
Professor Thomas A. Schwarz

Dedication

Dedicated to my parents.

TABLE OF CONTENTS

Dedication . . . . **ii**

List of Figures . . . . **v**

List of Tables . . . . **viii**

List of Appendices . . . . **ix**

Abstract . . . . **x**

Chapter

1 Introduction **1**

1.1 Preamble: The Standard Model and Beyond 1
1.2 An Overview of String Phenomenology 3
  1.2.1 Extra Dimensions and Moduli Stabilizaion 4
  1.2.2 Navigating the String Landscape 6
1.3 An Outline of this Thesis 7

2 Moduli Stabilization in the G_2-MSSM **10**

2.1 A Crash Course in Supersymmetry 10
  2.1.1 The Minimal Supersymmetric Standard Model 11
  2.1.2 $SU(5)$ Grand Unification 15
  2.1.3 Supersymmetry Breaking 15
2.2 Moduli Stabilization and Supersymmetry Breaking in the G_2-MSSM . . . 16
  2.2.1 Moduli and Matter Kahler Potential 16
  2.2.2 Moduli Superpotential 17
  2.2.3 Moduli Stabilization and Determining $M_{3/2}$ 19
  2.2.4 Hierarchy between Gaugino Masses and $M_{3/2}$ 23

3 Collider Predictions of the G_2-MSSM **25**

3.1 Theoretical Framework 26
  3.1.1 Imposing Constraints: EWSB and the Higgs Mass 28
  3.1.2 Obtaining a Benchmark Spectrum 28
3.2 The spectrum and the branching ratios 32
3.3 LHC-14 Predictions 34
3.4 Future Collider Predictions 35
3.5 Conclusion 37

4 Future Collider Probes of String Compactifications **39**
4.1 General Methodology 40
4.1.1 Simplified Models 41
4.2 Squark-Gluino Associated Production 42
4.3 Squark-Wino and Squark-Bino Associated Production 45
4.4 Summary 48
5 Dark Sector Dark Matter in String Compactifications **50**
5.1 Overview of Two-Sectors - Models and Cosmology 52
5.1.1 Cosmological Evolution 53
5.2 Solution of the Boltzmann Equations and the Dark Matter Abundance . . 57
5.2.1 Useful Approximations 57
5.2.1.1 Approximate solutions for Φ, R and R' 57
5.2.1.2 Temperature-scale factor relation and the “maximum” temperature 58
5.2.1.3 Approximate solution for X 60
5.2.2 Classifying Production Mechanisms for Relic Dark Matter 63
5.2.3 Efficient Annihilation at T'_D: $\langle\sigma v\rangle' > \langle\sigma v\rangle'_c$ 65
5.2.3.1 Non-relativistic quasi-static equilibrium 65
5.2.3.2 Standard freezeout during radiation domination 66
5.2.4 Inefficient Annihilation at T'_D: $\langle\sigma v\rangle' < \langle\sigma v\rangle'_c$ 68
5.2.4.1 Non-relativistic freezeout during modulus domination . . 69
5.2.4.2 Non-relativistic and relativistic inverse annihilation . . . 70
5.2.5 Summary of Results 73
5.2.5.1 Reducing to a Single Sector 75
5.3 Implications for UV-motivated Supersymmetric Theories 76
5.4 Experimental/Observational Consequences 79
5.4.1 Cosmological/Astrophysical Effects 81
5.4.2 Prospects for the Framework 83
5.5 Summary and Future Directions 86
6 Conclusion **90**

Appendices **92**

Bibliography **106**

LIST OF FIGURES

2.1 One-loop contribution to the Higgs mass involving the top and stops. 14

3.1 **Upper Figure**: The dark gray surface shows the slice of $M_{3/2}, c, \mu/M_{3/2}$ parameter space which satisfies EWSB, while red points also satisfy the Higgs mass constraint $M_h = 125.2 \pm 0.4$ GeV. The blue shaded region corresponds to points which are inconsistent with $\mu/M_{3/2} \lesssim 0.1$; see the Appendix for further discussion. In these plots, μ is defined at the renormalization scale $Q^2 = m_{\tilde{t}_1} m_{\tilde{t}_2}$. The mesh lines are added for perspective, and do not have any physical significance. **Lower Figure**: A projection of the upper figure onto the $M_{3/2} - \mu/M_{3/2}$ plane. 29

3.2 Gluino mass vs $M_{3/2}$ for points which satisfy EWSB and Higgs mass constraints, i.e. the red points in Figure 3.1. 32

3.3 Spectrum given GUT scale input values calculated from the theory for the central value $M_{3/2} = 35\,\mathrm{TeV}$. This spectrum has the GUT scale inputs $m_0 \approx$ 24 TeV and $A_0 \approx$ 25 TeV, where m_0 and A_0 are respectively the universal scalar mass and soft-breaking trilinear. The GUT scale gaugino masses are $M_1 = -1020\,\mathrm{GeV}$, $M_2 = -730\,\mathrm{GeV}$, $M_3 = -590\,\mathrm{GeV}$. Details on how this spectrum was derived are presented in Section 3.1. For the gaugino masses and trilinear, we take the sign convention opposite to that of `SOFTSUSY` . This relative sign affects the 2-loop term in the gaugino mass RGE's which is proportional to A_t. 33

3.4 Dominant Feynman graph for stop associated production by gluon splitting. . . 36

4.1 Experimental reach for squark-gluino associated production at a 100 TeV proton collider with 3 ab^{-1} integrated luminosity, for spectra with a ~ 100 GeV LSP mass. The solid, long dashed and short dashed lines are for and $5,\ 10,\ 15\%$ systematic uncertainty for the signal respectively. Blue lines indicate 5σ discovery reach and red lines indicate 95% exclusion limits. We assume 20% systematic uncertainty in the background. 43

4.2 Experimental reach for squark-gluino associated production at a 100 TeV proton collider with 3 ab^{-1} integrated luminosity for spectra with $m_{\tilde{g}} - m_{\chi_1^0} = 15$ GeV. The different lines follow the conventions of Fig. 4.1. We assume 20% systematic uncertainty in the background. 44

4.3 Experimental reach for squark-Wino LSP associated production at a 100 TeV proton collider with 3 ab^{-1} integrated luminosity. The solid, long dashed and short dashed lines are for $1,\ 2,\ 3\%$ systematic uncertainty for the background respectively. Blue lines indicate 5σ discovery reach and red lines indicate 95% exclusion limits. We do not consider the grey shaded region ($m_{\tilde{q}} - m_{\tilde{W}} < 1$ TeV) for reasons given in the text. We assume 10% systematic uncertainty for the signal. 46

4.4 Experimental reach for squark-Bino LSP associated production at a 100 TeV proton collider with 3 ab^{-1} integrated luminosity. The solid, long dashed and short dashed lines are for and $0.5,\ 1,\ 1.5\%$ systematic uncertainty for the background respectively. Blue lines indicate 5σ discovery reach and red lines indicate 95% exclusion limits. We do not consider the region ($m_{\tilde{q}} - m_{\tilde{B}} < 1$ TeV) for reasons given in the text. We assume 10% systematic uncertainty in the signal. 47

4.5 Experimental reach for squark-Wino associated production at a 100 TeV proton collider with 3 ab^{-1} integrated luminosity. Solid lines indicate 5σ discovery reach, and dotted lines indicate 95% exclusion limits. Blue curves correspond to a Wino LSP, while the green (red) curves correspond to a Wino NLSP with $M_{\rm NLSP} - M_{\rm LSP} = 200$ GeV ($M_{LSP} \sim 100$ GeV). The results are applicable for both Bino- and Higgsino-like LSP. We do not consider the grey shaded region ($m_{\tilde{q}} - m_{\tilde{W}} < 1$ TeV) for reasons given in the text. We assume 1% systematic uncertainty in the background and 10% in the signal. 48

5.1 Schematic representation of the Two-sector Framework under consideration. . 53

5.2 Plots of the exact solutions for $Y = \Phi$, R and X (normalized to their maximum values) as functions of the scale factor A. We have taken $H_I = 10^{15}\Gamma_\phi$, $B_X = 0.1$, $\langle\sigma v\rangle = 10^{-7}$ GeV^{-2} and $\Gamma_X = 10^{-5}$ GeV. All other parameters taken to their benchmark values (5.5). The dashed vertical line represents the scale factor $A = A_D$ defined in (5.21), which characterizes the transition between a modulus dominated and a radiation dominated universe. 62

5.3 Plot of the exact solution of the Boltzmann equations for X' (normalized to its maximum value) as a function of the scale factor A corresponding to the $QSE_{\rm nr}$ mechanism. We have taken $H_I = 10^{15}\Gamma_\phi$, $\langle\sigma v\rangle' = 10^{-6}\,$GeV^{-2} and $M_{X'} = 10$ GeV, with all other parameters set to the benchmark values (5.5). We have also plotted $X'_{\rm crit}$ (5.32) and $X'_{\rm QSE}$ (5.33). The horizontal dashed line corresponding to $A = A_c$ is determined by solving the transcendental equation (5.37) for A_c. 66

5.4 Plot of the exact solution for X' (normalized to its maximum value) as a function of the scale factor A corresponding to the $FO^{\rm mod}_{\rm nr}$ mechanism. We have taken $H_I = 10^{15}\Gamma_\phi$, $\langle\sigma v\rangle' = 10^{-6}\,$GeV^{-2}, $M_{X'} = 10$ GeV as in Figure 5.3, but have instead chosen $B_{tot} = 0$ so that the QSE condition is not satisfied, see (5.35). All other parameters set to benchmark values (5.5). For comparison we have also plotted the comoving X' equilibrium number density X'_{eq}. 69

5.5 Plot of the exact solution of the Boltzmann equations for X' (normalized to its maximum value) as a function of the scale factor A corresponding to the $IA_{\rm nr}$ and $IA_{\rm r}$ mechanisms. We have chosen $\langle\sigma v\rangle' = 10^{-16}\,{\rm GeV}^{-2}$, $M_{X'} = 10$ GeV for $IA_{\rm nr}$, and $\langle\sigma v\rangle' = 10^{-16}\,{\rm GeV}^{-2}$, $M_{X'} = 10^{-4}$ GeV for $IA_{\rm r}$, with $B_{tot} = 0$ and $H_I = 10^{15}\Gamma_\phi$; all other parameters taken to their benchmark values (5.5). . 71

5.6 Left column: scan of the $\langle\sigma v\rangle'$, $M_{X'}$ parameter space with $T_{RH} = 10$ MeV, $m_\phi = 50$ TeV, and various values of B_{tot}. Right column: similar plots with $T_{RH} = 100$ MeV, $m_\phi = 150$ TeV. All other parameters are fixed to the benchmark values (5.5). Solid (dashed) contours correspond to $\Omega_{DM}h^2 = 0.12\,(0.012)$. Green, blue and gray regions represent $\Omega_{DM}h^2 < 0.012$, $0.012 < \Omega_{DM}h^2 < 0.12$ and $0.12 < \Omega_{DM}h^2$. 77

5.7 Hierarchies among the cosmological length scales L_{fs}, L_d, L_{RH} shown in the $M_{X'} - T'_{KD}$ plane, assuming $T'_{kd} < T'_D$. The pink region corresponds to $L_d > L_{fs}$, the green region corresponds to $L_{fs} > L_d$, the blue region corresponds to $L_{RH} > L_{cut}$, and the brown region corresponds to $L_{cut} > 1$ Mpc. The other relevant parameters are set to their benchmark values, see (5.5). 85

5.8 Plot of the free-streaming length L_{fs} in Mpc. The blue lines correspond to DM produced predominantly via inverse annihilations, while the black lines correspond to DM produced predominantly via modulus decay. The solid lines were obtained for $T_{RH} = 10$ MeV, $m_\phi = 50$ TeV while the dashed lines were obtained for $T_{RH} = 100$ MeV, $m_\phi = 150$ TeV. The other relevant parameters are chosen as in (5.5). 87

E.1 Top: $\Omega_{DM}h^2$ as a function of $\langle\sigma v\rangle'$ for $M_{X'} = 10$ GeV and $B_{\rm tot} = 0.1$. The green curve shows the numerical solution, while the black curve shows the approximate $QSE_{\rm nr}$ solution (5.35). The vertical dashed line represents $\langle\sigma v\rangle' = \langle\sigma v\rangle'_c$ as defined in (5.35), while the horizontal dashed line shows represents the modulus decay contribution given in (5.43), which is valid for $\langle\sigma v\rangle' < \langle\sigma v\rangle'_c$. Bottom: the ratio of the approximate result for $QSE_{\rm nr}$ to the exact result. 101

E.2 Top: $\Omega_{DM}h^2$ as a function of $\langle\sigma v\rangle'$ for $M_{X'} = 10$ GeV and $B_{\rm tot} = 0$. Bottom: similar plot for $M_{X'} = 10^{-6}$ GeV and $B_{\rm tot} = 0$. The green curves show the numerical solution, the red curve shows the approximation for $IA_{\rm nr}$ (top) and $IA_{\rm r}$ (bottom), while the black curve shows the approximation for $FO^{\rm mod}_{\rm nr}$ (top) and $FO^{\rm rad}_{\rm nr}$ (bottom). In the left plot the vertical dashed line represents $\langle\sigma v\rangle' = \langle\sigma v\rangle'_0$, defined in (5.46), while in the bottom plot the vertical line represents $\langle\sigma v\rangle' = \langle\sigma v\rangle'_c$ in the case where $M_{X'} < T'_D$ (see (5.35)). The dashed horizontal line in the bottom plot shows the approximate solution for $FO^{\rm rad}_{\rm r}$. 102

LIST OF TABLES

2.1 Taxonomy and nomenclature of particles in the MSSM. 12

3.1 Branching ratios of gluino, neutralinos and charginos. The numbers don't add to 100 in the case of the χ_4^0 branching ratios due to rounding errors. 34

4.1 Simplified models considered in this chapter. 41

5.1 Summary of the different parametric regimes for $\Omega_{DM}h^2$ as discussed in Section 5.2.2. The quantity $\langle \sigma v \rangle_c'$ is defined in (5.35) and $\langle \sigma v \rangle_0'$ in (5.46). The temperatures $T'_{\max}$ is defined in (5.18), T'_D in (5.20), and T'_{FO} above (5.44). . . 73

LIST OF APPENDICES

A Constraints from EWSB and M_h **92**

B Event generation **94**

C Justification of Approximations for R, R' **95**

D A Very Long-lived X Particle **97**

E Accuracy of Approximate Solutions **100**

F Temperature Dependence of the Annihilation Cross Section **103**

ABSTRACT

This thesis discusses the methodology for extracting concrete experimental predictions from compactified string theories. The primary difficulty encountered in phenomenological studies of string theory is the presence of a “string landscape”, which refers to the numerous physically inequivalent ground states (vacuaa) predicted by a particular string compactification. Without a mechanism for selecting the “true” vacuum that describes nature, it is difficult to make predictions for low energy physics purely from UV considerations. In this thesis, we will instead leverage experimental constraints to isolate regions of the string landscape that are consistent with all known experimental data. Given these restrictions on the string landscape, it is possible to make concrete predictions for upcoming experiments. We will carry out this procedure, and study the resulting phenomenology for collider physics and dark matter predicted by realistic compactified string theories. We will also discuss how these predictions can be tested with new experiments, such as a future hadron collider operating at 100 TeV. Some parts of this work (Chapters 2 and 3) are specific to a particular string compactification known as the “G_2-MSSM”, while other parts (Chapters 4 and 5) are applicable to string compactifications in general.

CHAPTER 1

Introduction

This thesis discusses the methodology for making experimental predictions from an underlying compactified string theory. In particular I will focus on how one can leverage phenomenological constraints to sharpen experimental predictions for the string landscape. Although much of this work is done in the context of M-theory compactifications whose construction was pioneered in [1, 2, 3, 4, 5, 6, 7, 8], the philosophy and approach described herein is in principle applicable to string compactifications in general. This thesis focuses predominantly on three of my recently published papers which study string theory predictions for collider physics [9, 10] and dark matter [11]. The purpose of this introduction is to provide some context for the results discussed in this thesis and to outline the remaining chapters of this work.

1.1 Preamble: The Standard Model and Beyond

The field of particle physics has always aspired to understand the fundamental interactions which govern nature. Over the past century, particle physicists have made monumental strides towards achieving this goal. The crowning achievement of this endeavor is the Standard Model, a theory which elegantly encompasses nearly all experimentally observed non-gravitational phenomena. The recent discovery of the Higgs boson [12, 13] at the Large Hadron Collider (LHC) further cemented the Standard Model as a state of the art model for particle physics, ending a decades long experimental search to understand the origin of spontaneous symmetry breaking. There are however a variety of experimental and theoretical reasons to believe that framework of the Standard Model + general relativity (GR) does not give a complete description of the universe. Rather than give an exhaustive list of these reasons, I will focus on the pieces of evidence for Beyond Standard Model (BSM) physics which are central to the motivation of this thesis.

From a theoretical point of view, there is the question of how the Standard Model can be unified with general relativity to give a consistent theory of quantum gravity, and the related problem of technical naturalness. In the context of a quantum field theory (QFT), GR can be described as a long-ranged force mediated by massless gravitons. Such a theory is inherently non-renormalizable, as gravitons couple to matter via higher dimensional operators (suppressed by negative powers of the Planck mass). From our usual intuition with effective field theories (EFTs), this implies that the QFT for gravitational interactions is the low energy limit of some ultraviolet (UV) theory of quantum gravity. This motivates the presence of BSM physics for two reasons.

The first reason is simply that a consistent UV completion of quantum gravity necessitates some drastically new BSM physics which manifests at energies above the Planck scale. The second reason is that incorporating any new high-mass scales within the Standard Model leads to the problem of technical naturalness (also known as the hierarchy problem). Technical naturalness is the statement that in a QFT, any dimensionful couplings which are not protected by symmetries[1] will receive quantum (loop) corrections of order the cutoff of the theory[14]. If nature is described only by the Standard Model + quantum gravity, the cutoff for the Standard Model EFT is of order the Planck mass. The problem then arises because scalar masses in the Standard Model + gravity are not protected by any symmetry, and would naively be of order the Planck mass. Thus without any new physics below the Planck scale, *all* scalar particles would be expected to have masses $\mathcal{O}(M_{pl}) \sim 10^{18}$ GeV. This is obviously contradicted by the discovery of an $\mathcal{O}(100)$ GeV Higgs boson mentioned above (along with the presence of $\mathcal{O}(100)$ GeV gauge bosons). One way to address this problem is to suppose that the Standard Model is “fine-tuned” and unnatural, such that all $\mathcal{O}({M_{pl}}^2)$ contributions to the mass parameter $\mathcal{L} \supset -{m_H}^2 \left|H\right|^2$ cancel up to one part in 10^{32}. This explanation is disfavored by many in the field, as such a cancellation seems quite ad-hoc in the Standard Model. Another way to address the fine-tuning problem is to add BSM physics with non-trivial structure that enforces the cancellation of dangerous loop corrections to scalar masses. This thesis will favor the latter explanation, focusing in particular on Supersymmetry as a new physics mechanism for restoring naturalness to the SM. The precise mechanism for this is discussed in more detail in Chapter 2.

There is also a litany of experimental evidence for new physics beyond the Standard Model. In contrast to the above issues which are more theoretical and abstract in nature, these experimental issues *unequivocally* demonstrate that the Standard Model is an incomplete description of nature. After all, the true unambiguous test of a physical theory is

---

[1] Here ”protected by symmetries” refers to couplings which enhance the global symmetries of the Lagrangian if the coupling vanishes.

whether or not it agrees with experimental data. There are many experimental observations which can not be accounted for by the Standard Model[2], notably neutrino oscillations/masses, the matter anti-matter asymmetry, and the presence of dark matter. Of these issues, this thesis will focus on the question of dark matter and how it might arise from attractive models for BSM physics.

In this thesis, I will explore the possibility that string theory is the UV completion of the Standard Model that addresses both the theoretical and experimental concerns raised above. String theory handily addresses the theoretical issues raised above, as it provides a consistent UV complete theory of quantum gravity that solves the naturalness problem via Supersymmetry. The study of string theory as a candidate for BSM physics is known as string phenomenology. In the following, I will give a brief overview of string phenomenology, and discuss the challenges encountered when attempting to formulate predictions from string theory for experimental data.

1.2 An Overview of String Phenomenology

As evidenced by the preceding section, the motivations for studying BSM physics can be divided into two categories: theoretical and phenomenological/experimental. This dichotomy is typified by the two approaches to BSM model building, known colloquially as the "top-down" approach versus the "bottom-up" approach. In the "top-down" approach, one is motivated primarily by the theoretical issues associated with UV-completing the Standard Model. Given a seemingly salient UV completion to the Standard Model, one determines to what extent the UV completion of interest is consistent with the multitude of known experimental constraints. In the "bottom-up" approach, one instead remains agnostic about the particular nature of the UV completion and focuses primarily on how BSM physics manifests at low energies (compared to the scale of the UV completion).

Both of these approaches have their respective weaknesses. In the top-down approach, a typical difficulty lies in the fact that concrete predictions for low energy phenomenology are often technically challenging to extract from the UV theory. It is not uncommon to begin with an *a priori* realistic UV completion of the Standard Model and put in significant effort to understand the resulting phenomenology, only to realize that the model is completely ruled out by some combination of experimental constraints. The bottom-up approach avoids this problem, as the starting point for bottom-up model building is usually the Standard Model itself plus some additional particles (dark matter, vector-like quarks, etc.).

---

[2] Honorable mention to the strong CP problem, which is similar to the hierarchy problem in that it can be solved either by fine-tuning the Standard Model or by incorporating new physics such as axions[15].

The weakness of "bottom-up" model building is that such models are usually motivated by an (often fleeting) experimental anomaly, rather than some more fundamental theoretical considerations. Thus it is often difficult to asses whether or not a "bottom-up" model can be considered as a legitimate step towards formulating a consistent UV completion of the Standard Model as discussed above.

As the reader might have anticipated, it is possible to combine the "top-down" and "bottom-up" approaches to BSM model building in order to overcome the weaknesses of each individual approach. Theoretical constraints from an underlying UV theory can be combined with a plethora of experimental constraints in order to obtain a viable "bottom-up" theory while still maintaining a deeper theoretical motivation. This, in essence, is the guiding principle behind modern string phenomenology, much of which was pioneered by my advisor Gordon Kane alongside other collaborators.

Before discussing string phenomenology, it is useful to review the motivation behind string theory itself. As discussed in the preamble, one important open problem in particle physics is formulating a UV complete theory of quantum gravity. Perhaps the most significant success of string theory is that it indeed provides a consistent UV completion of quantum gravity, which reproduces general relativity as its low energy limit. Furthermore, string theory naturally predicts Supersymmetry [3] which provides an elegant solution to the technical naturalness problem discussed in the preamble- this will be elaborated upon in Chapter 2. A detailed technical discussion and formulation of string theory is beyond the scope of my thesis, and I recommend [16, 17] for a pedagogical overview of such topics.

1.2.1 Extra Dimensions and Moduli Stabilizaion

An interesting consequence of string theory is that anomaly cancellation conditions imply that string theory is only consistent for a fixed number of spacetime dimensions. Concretely, type I, type II and heterotic string theories are only consistent in 10 spacetime dimensions, while M-theory instead implies 11 spacetime dimensions. This immediately begs the following phenomenological problem: if our universe is described by string theory, why do we observe only 4 spacetime dimensions? A potential explanation for this is that the extra spacetime dimensions become *compactified* due to some underlying dynamics. By compactified, we mean that the additional spacetime dimensions are finite and sufficiently small in volume such that they are virtually unobservable in modern experi-

---

[3] There is a distinction between purely bosonic string theory and "superstring" theory which contains bosonic and fermionic degrees of freedom. Phenomenological studies of string theory actually refer to superstring theory, which gives much more realistic phenomenology than its purely bosonic counterpart (which predicts tachyons). I will refer to superstring theory simply as string theory as is often done in the literature.

ments.

An illustrative example is the original 5-D Kaluza-Klein theory (see e.g. [18]). In this toy model, there are four non-compact spacetime dimensions and one compact circular dimension with radius R. Integrating over the compact dimension gives an effective 4-D theory where the presence of a 5th compact dimension is encoded in a "tower" of additional particles with masses $\gtrsim R^{-1}$ (in natural units). To see this, consider a massless scalar field ϕ in 5D with coordinates $x_M = (x_\mu, \theta)$. We can write this scalar field in terms of its Fourier modes along the compact dimension, resulting in $\phi(x_\mu, \theta) = \sum_n \phi_n(x_\mu) e^{in\theta}$. The 5D equation of motion $\partial_M \partial^M \phi(x_\mu, \theta) = 0$ then decomposes as[4]:

$$\left(\partial_\mu \partial^\mu - R^{-2} \partial_\theta^2\right) \phi(x_\mu, \theta) = 0 \implies \left(\partial_\mu \partial^\mu \phi_n(x_\mu) + \frac{n^2}{R^2}\right) \phi_n(x_\mu) = 0 \tag{1.1}$$

which from the 4D point of view yields a tower of particles ϕ_n with $m_n = n/R$. Thus the presence of extra dimensions can only be directly observed when the energy scale of a process exceeds the inverse compactification radius R^{-1} (in natural units). This is a general feature of compactified theories. In the context of string compactifications, $R^{-1} \sim M_{pl} \sim 10^{18}$ GeV, so the extra dimensions are unobservable to even our highest energy experimental probes[5].

Although the compact dimensions of string theory can not directly be observed, their presence indirectly affects the 4D effective theory through fields known as *moduli* (see e.g. [21]). Moduli are scalar fields in the 4D theory which arise as zero-modes of the metric along the compact dimensions. Here "zero-mode" refers to the massless mode of the Kaluza-Klein tower e.g. the $n = 0$ mode in (1.1). These moduli fields parameterize the size and shapes of the compact dimensions. For example, in the 5D Kaluza-Klein model, the zero-mode of the metric component $g_{\theta\theta}$ gives a scalar field in 4D which corresponds to the radius of the compact dimension. In realistic compactified theories, there must be some dynamics to give the moduli fields non-zero expectation values and thus stabilize the structure of the compact dimensions. Such a mechanism is referred to as *moduli stabilization*, and is required to prevent phenomenologically dangerous massless moduli in the 4D theory. In compactified string theories with low-energy Supersymmetry[6], moduli stabilization often provides a direct link between the geometric structure of the compact dimensions and the particle content of the 4D effective theory. This is because in a large class of string models, moduli stabilization also breaks Supersymmetry and sets the mass spectrum of

---

[4] Using the mostly minus metric convention e.g. (+,-,-,...).

[5] The possibility of a much lower compactification scale with $R^{-1} \sim$ TeV has also been considered[19, 20]

[6] We remind the reader that we are considering superstring theories (see footnote 3) which yield a Supersymmetric field theory as its low energy limit.

Supersymmetric particles. In fact, fairly general arguments show that moduli stabilization must break Supersymmetry to allow axions to solve the strong CP problem[22]. Because of this connection, the nature of the compact dimensions can be *indirectly observed* by measuring the mass spectrum of Supersymmetric particles. This connection will be explored more explicitly in Chapters 2 and 3 in the context of realistic M-theory compactifications.

1.2.2 Navigating the String Landscape

The dynamics of moduli stabilization as described above represent one of the greatest open problems in string phenomenology. Many studies of string phenomenology simply assume an ansatz for the compact dimensions (e.g. Calabi-Yau manifold[23] or a toroidal orbifold[24, 25]), and treat moduli stabilization as stabilizing perturbations about such an ansatz. The problem with this approach is that there are a multitude of different ways a given string theory can be compactified to give low energy Supersymmetry[7], and each different compactification geometry will yield different predictions for the Supersymmetric particle spectrum. Without a better understanding of moduli stabilization, it is difficult to *a priori* discern which of these different compactifications (if any) provide an accurate description of the universe. Phrased differently, string theory contains numerous different ground states or vacuaa corresponding to different compact geometries, and we do not yet understand the mechanism through which string theory "selects" a particular vacuum from these different possibilties. The presence of numerous inequivalent vacuaa with realistic phenomenology gives rise to what is known as the *string landscape* (see [26] for an overview of this concept).

The string landscape exemplifies the problem with "top-down" approaches mentioned in Section 1.1, namely that it is technically challenging to extract unambiguous phenomenological predictions from a purely UV standpoint. However, progress can be made if one combines these UV considerations with "bottom-up" input from experimental data. The idea behind this approach is that although numerous compactifications can reproduce the Standard Model and yield seemingly realistic phenomenology, many would-be candidates for BSM physics are inevitably excluded by some combination of experimental constraints. Thus although we do not understand the UV dynamics for selecting a vacuum from the string landscape, imposing all known experimental constraints will by itself rule out a significant portion of the string landscape. This approach is the synthesis of the "top-down" and "bottom-up" approaches to model building discussed earlier in this section. Using this

---

[7] We are interested in compactifications that yield a 4D theory with $\mathcal{N} = 1$ Supersymmetry, as they provide a solution to the naturalness/hierarchy problem discussed in Section 1.1.

approach, one can then focus on the subset of string vacuaa that satisfy all known experimental constraints and make correlated predictions for upcoming experiments.

An example of this approach was carried in the mid to late 2000's in the context of M-theory compactified on a manifold of G_2 holonomy [27, 28, 29]. M-theory, unlike the other 10D incarnations of string theory, is conjectured to contain 11 spacetime dimensions. Here G_2 refers to the holonomy group[8] of the compact 7D manifold required to maintain superysmmetry in the 4D theory [30]. The resulting model, known as the G_2-MSSM, combined cosmological constraints from Big Bang nucleosynthesis (BBN) with UV considerations to argue that the spectrum expected from compactified M-theory consisted of heavy $\gtrsim$ 10 TeV scalar superpartners and lighter $\mathcal{O}(100 - 1000)$ GeV fermionic superpartners. Furthermore, I was involved with a project that predicted a 120-130 GeV Higgs boson in the G_2-MSSM [31, 32]. This prediction was later experimentally validated by the Higgs discovery [12, 13]. As discussed in Chapter 3, the Higgs boson discovery gives a prime example of how we can incorporate new experimental data to help further narrow the promising regions of the string landscape.

1.3 An Outline of this Thesis

The work presented in this thesis expands upon the "top-down meets bottom-up" approach to string phenomenology discussed in the preceding section. In the following, I will explore in more detail the compactified string theory predictions for experimental signatures of BSM physics. In particular I will discuss predictions for the LHC (Chapter 3), predictions for future hadron colliders (Chapter 4) and experimental searches for dark matter (Chapter 5). Chapters 2 and 3 are specific to M-theory compactified on a manifold of G_2 holonomy (hereafter referred to as the G_2-MSSM), while Chapters 4 and 5 are applicable to compactified string theories in general. I will now briefly outline the contents of each subsequent chapter, and summarize the main results therein.

Chapter 2: Moduli Stabilization in the G_2-MSSM

In this chapter, I will provide an overview of moduli stabilization and Supersymmetry breaking in the G_2-MSSM. This chapter can be thought of as a "primer" for the G_2-MSSM, and reviews the main results of the earlier pioneering papers [27, 28, 29]. First, I will give a very brief overview of Supersymmetry and how it extends the Standard Model. I will

---

[8] Roughly speaking, the holonomy of a manifold corresponds to the group of transformations which result from parallel transporting vectors along closed loops.

then discuss how non-perturbative dynamics in a hidden sector can stabilize all of the G_2 moduli fields, breaking Supersymmetry and giving masses to the Supersymmetric partners of Standard Model particles. I will arrive at the result that in the G_2-MSSM, the masses of scalar superpartners are $\gtrsim \mathcal{O}(20)$ TeV while the fermionic superpartners[9] are roughly one to two orders of magnitude lighter.

Chapter 3: Collider Predictions of the G_2-MSSM

In this chapter, I will discuss in more detail the collider phenomenology of the G_2-MSSM given the Supersymmetry breaking parameters derived in Chapter 2. This chapter is largely based on the results in [9]. I will show that imposing the measured Higgs mass constraint reduces the dimensionality of the G_2-MSSM parameter space to a single dimension. I will then take a benchmark spectrum with a 35 TeV gravitino mass as a concrete example to illustrate the LHC signatures of these models. This benchmark spectrum contains a 1.5 TeV mass gluino which is discoverable by the upcoming 14 TeV run of the LHC. Squarks on the other hand are out of reach, but may be discoverable at a 100 TeV hadron collider via the channels described in Chapter 3.

Chapter 4: Future Collider Probes of String Compactifications

In this chapter, I will discuss future collider signatures of compactified string theories. This chapter is largely based on the results of [10]. In Chapter 3, we discussed collider signatures in the specific model of the G_2-MSSM. Here we instead consider collider signatures of string compactifications in general, without making any assumptions regarding a particular model. In many corners of compactified string theory, it is a fairly general result that one expects $\gtrsim 20$ TeV scalar superpartners and $\mathcal{O}(100-1000)$ GeV gauge boson superpartners (gauginos); see [33] for a review. Given such a spectrum, scalar quarks (squarks) are well out of kinematic reach of the LHC. I will instead discuss the prospects of observing heavy squarks at a future hadron collider operating at a center of mass energy of 100 TeV. The possibility of such a future collider has recently received significant attention within the particle physics community. Although pair production of $\gtrsim 20$ TeV squarks will not give observable signatures even at 100 TeV, the production of a $\gtrsim 20$ TeV squark in association with a lighter gaugino is a promising method for observing such heavy squarks. I will examine these future colliders signatures in detail, and show that squark-gaugino associated production can discover squark masses up to $\approx$ 32 TeV in compactified string models

---

[9] Excluding the Higgsinos, see Chapter 2.

with light gauginos[10]. This production channel is perhaps the only possibility for directly observing the heavy scalar superpartners predicted by many compactified string models.

Chapter 5: Hidden Sector Dark Matter in String Compactifications

In this chapter, I will discuss dark matter phenomenology in compactified string theories. This chapter is largely based on the results of [11]. Similar to the discussion in Chapter 4, this section will discuss dark matter in string compactifications in general without focusing on a particular model. I will argue that given the current constraints from dark matter indirect detection experiments, dark matter in compactified string models can not couple strongly to Standard Model particles. This implies that dark matter must reside in a "dark sector" comprised of particles which couple very weakly to the Standard Model. I will then perform a detailed study of the Boltzmann equations which govern the cosmological evolution of dark sector particles, including the dark matter. This will allow us to identify the potential production mechanisms for relic dark matter in this dark sector framework. I will then map out the parameter space of these models, and show that most of the compactified string theory parameter space results in an overabundance of dark matter. Thus the measured dark matter relic abundance provides another important "bottom-up" constraint for navigating the string landscape. I will then briefly discuss the experimental signatures expected of such models. These dark matter models predict an absence of direct detection and collider signatures for dark matter, but may allow for observable signatures in indirect detection experiments.

---

[10] This reach assumes that a 2 TeV gluino is also present in the spectrum, see Chapter 4 for details.

CHAPTER 2

Moduli Stabilization in the G_2-MSSM

In Chapter 1, we discussed how the extra compact spacetime dimensions predicted by string theory manifest as scalar moduli fields in the effective 4D theory. Moreover in a large class of string compactifications, the geometric structure of these compact dimensions directly influences the particle spectrum predicted in the 4D theory. This connection manifests through moduli stabilization (i.e. giving *vev*'s to the moduli fields), which breaks Supersymmetry and sets the mass scale for the Supersymmetric particles in the 4D theory. In this chapter we provide a concrete example of this connection in a particular model, namely M-theory compactified on a manifold of G_2-holonomy (see Section 1.2.2 for an explanation of this terminology). This model is referred to in the literature as the G_2-MSSM.

This chapter is organized as follows. In Section 2.1, we provide a very brief overview of Supersymmetry in order to provide some context for the reader. In Section 2.2, we review the connection between moduli stabilization and Supersymmetry breaking in the G_2-MSSM. We show that the spectrum of Supersymmetric particles predicted in the G_2-MSSM is approximately calculable given certain well-motivated assumptions regarding the UV theory. A key result which is crucial for the connection between compactified M-theory and TeV scale physics is the fact that moduli stabilization fixes the gravitino mass (defined in Section 2.1) to be 50 TeV, within a factor of 2 or so. The results of Section 2.2 will largely be a review of previous work done in [27, 28, 29, 34].

2.1 A Crash Course in Supersymmetry

Supersymmetry (SUSY) describes a class of theories in which the Poincare symmetry of the Lagrangian is enhanced by including additional spinorial and anti-commuting generators Q^i_α. This extends the Poincare algebra to the so-called "super-Poincare" algebra via the following relations:

$$\begin{aligned} \{Q^i_\alpha, \bar{Q}^j_{\dot{\alpha}}\} &= 2\delta^{ij}\sigma^\mu_{\alpha\dot{\alpha}}P_\mu, & \{Q^i_\alpha, Q^j_\beta\} &= \epsilon_{\alpha\beta}Z^{ij}, \\ [Q^i_\alpha, P^\mu] &= 0, & [Q^i_\alpha, M^{\mu\nu}] &= i\sigma^{\mu\nu}_{\alpha\beta}Q^i_\beta \end{aligned} \tag{2.1}$$

Here we have adopted two-component notation[1] (see e.g. [35]) with indices α, β. $M_{\mu\nu}$ are generators of Lorentz transformations i.e. boosts and rotations. The indicies i, j run from 1 to $\mathcal{N}$, where $\mathcal{N}$ is the total number of Supersymmetric generators in the theory. Z^{ij} is an antisymmetric matrix containing the so-called central charges of the theory. Due to the antisymmetry of Z^{ij}, centeral charges are absent in $\mathcal{N} = 1$ theories.

The studies of SUSY theories defined by (2.1) is a very rich topic of significant theoretical interest. In this thesis we focus on SUSY as an extension of the Standard Model that solves the naturalness problem discussed in Chapter 1. This restricts us to considering $\mathcal{N} = 1$ Supersymmetry, as it allows for the chiral fermions observed in the Standard Model. The topic of $\mathcal{N} = 1$ SUSY extensions to the Standard Model is itself quite deep. In this section we will only review the relevant aspects in order to keep this thesis as concise and self-contained as possible. There are many great comprehensive reviews on this topic, for example [36, 37].

2.1.1 The Minimal Supersymmetric Standard Model

In SUSY theories, the transformations generated by Q^i_α transform half-integer spin particles (fermions) into integer spin particles (bosons) and vice-versa. Thus each fermion has a bosonic "superpartner"; these partners are related to one another via SUSY transformations. The field content of SUSY theories is organized into "superfields" which contain both fermionic and bosonic degrees of freedom. In the $\mathcal{N} = 1$ theories we are interested in, there are two types of superfields: chiral superfields and vector superfields. Chiral superfields Φ contain a complex scalar and a left-handed Weyl fermion, while vector superfields V^α contain a vector boson and a Majorana fermion[2]. As their names imply, Standard Model fermions (i.e. quarks and leptons) are contained in chiral superfields while the gauge bosons are contained within vector superfields. Superpartners to fermions are referred to as sfermions, while superpartners to gauge bosons are referred to as gauginos.

Given this heuristic description, we can give a taxonomy of particles expected in the minimal $\mathcal{N} = 1$ extension to the Standard Model, also known as the MSSM. This taxonomy, along with the corresponding nomenclature, is given in Table 2.1. As can be seen

---

[1] Note that $\sigma^{\mu\nu}_{\alpha\beta} \equiv \frac{1}{4}[\sigma^\mu_{\alpha\dot{\alpha}}\overline{\sigma}^\nu_{\dot{\alpha}\beta} - \sigma^\nu_{\alpha\dot{\alpha}}\overline{\sigma}^\mu_{\dot{\alpha}\beta}]$.

[2] We are only considering the on-shell degrees of freedom within these superfields.

SM Particle	SUSY Partner	Spin of SUSY Partner
Quark	Squark	0
Lepton	Slepton	0
$SU(2)_W$ gauge boson	Wino	1/2
$U(1)_Y$ gauge boson	Bino	1/2
Gluon	Gluino	1/2
Up-type Higgs H_u	Higgsino	1/2
Down-type Higgs H_d	Higgsino	1/2

Table 2.1: Taxonomy and nomenclature of particles in the MSSM.

from this table, one immediate consequence of a SUSY Standard Model is the presence of two $SU(2)_W$ doublet Higgs fields. This is because supersymmetrizing the Higgs field introduces a Weyl fermion, the Higgsino, which is charged under $U(1)_Y$. If only a single Higgs superfield is included, the corresponding Higgsino induces a $U(1)_Y$ triangle anomaly. Thus in order to preseve cancellation of gauge anomalies, we must introduce another Higgs superfield with opposite $U(1)_Y$ charge. As will be shown below, the up-type Higgs fields gives mass to up-type (up, charm, top) quarks while the down-type Higgs field gives mass to down-type (down, strange, bottom) quarks and leptons. The SM Higgs is typically identified as the lightest real scalar resulting from the H_u, H_d mass matrix.

Note that we have denoted the superpartners of electroweak gauge bosons in terms of gauge eigenstates ($SU(2)_W \times U(1)_Y$) as opposed to mass eigenstates ($Z, W^{\pm}, \gamma$). In the presence of electroweak symmetry breaking, the $SU(2)_W$ triplet Wino will decompose into a neutral gaugino and two electrically charged gauginos, while each $SU(2)_W$ doublet Higgsino decomposes into a neutral and charged fermion. Combined with the neutral Bino, we now have four neutral Majorana fermions (Bino, Wino and Higgsinos) and two charged Dirac fermions (Winos and Higgsinos). These fermions will mix with one another in the presence of a non-zero Higgs *vev*. In the mass eigenstate basis, the four neutral fermions are referred to as "neutralinos", while the charged fermions are referred to as "charginos". In compactified string theories the lightest Supersymmetric particle (LSP) is typically the lightest neutralino. This has implications for collider physics as discussed in Chapter 3.

We now discuss the interactions of the MSSM. Interactions amongst chiral superfields are encoded in a "superpotential" denoted by W. The superpotential is a holomorphic function of superfields i.e. only involves chiral superfields rather than anti-chiral superfields.

The MSSM superpotential is given by[3] [4]:

$$W = Y_u Q H_u U^c + Y_d Q H_d D^c + Y_l L H_d E^c + \mu H_u H_d \tag{2.2}$$

For simplicity we have suppressed gauge and generation indices. Y_u, Y_d and Y_l correspond respectively to up quark, down quark and lepton Yukawa couplings. Q and L denote the $SU(2)_W$ doublet quark and lepton superfields, while U^c, D^c and E^c denote the $SU(2)_W$ singlet quark and lepton superfields. From the superpotential, one can derive[5] the following interaction Lagrangian:

$$\mathcal{L}_W = -\frac{1}{2}\sum_{ij}\left(\frac{\partial^2 W}{\partial\Phi_i \partial\Phi_j}\psi_i\psi_j + \text{h.c.}\right) - \sum_i \left|\frac{\partial W}{\partial \Phi_i}\right|^2 \tag{2.3}$$

Here ψ_i denotes the left-handed Weyl fermion contained in the chiral superfield Φ_i. Note that for the partial derivatives of W appearing in (2.3), one must replace all chiral superfields with their scalar components.

The kinetic terms for chiral superfields, along with their corresponding gauge interactions, are encoded in a non-holomorphic function of superfields known as the Kahler potential. In addition to the standard gauge interactions, the Kahler potential also encodes supersymmetrized sfermion-fermion-gaugino gauge interactions. In compactified string theories, the Kahler potential also includes couplings between moduli and chiral superfields through gravitionally suppressed higher-dimensional operators. For the purpose of brevity we will not discuss the Kahler potential in more detail here, though it will be important for the SUSY breaking mechanism discussed in Section 2.2.

As stated in Chapter 1, one of the primary motivations for a SUSY extension of the Standard Model is the naturalness/hierarchy problem. To reiterate, this problem arises in theories with fundamental scalar fields and some UV cutoff Λ_{UV}. In the Standard Model, loop corrections will give a contribution to the Higgs mass parameter of order $\Delta m_H^2 \sim \Lambda_{UV}^2/16\pi^2$. This must be fine-tuned against other contributions to give the observed value $m_H \sim \mathcal{O}(100)$ GeV. In the MSSM however, this cancellation of UV contributions to the Higgs mass is actually enforced by Supersymmetry. For example, consider the SUSY version of the top quark Yukawa coupling, $W \supset y_t Q_3 H_u U_3^c$. Using (2.3) this results in the

---

[3] We omit the kinetic term for vector superfields which is also contained in the superpotential, see the references [36, 37] for details.

[4] Note that we have assumed R-parity, a Z_2 symmetry under which quark and lepton superfields are odd while all other superfields are even.

[5] The most straightforward way to obtain this result is via the superspace formalism, in which $\mathcal{L}_W = \int d^2\theta W$. See e.g. the appendix of [38] for details.

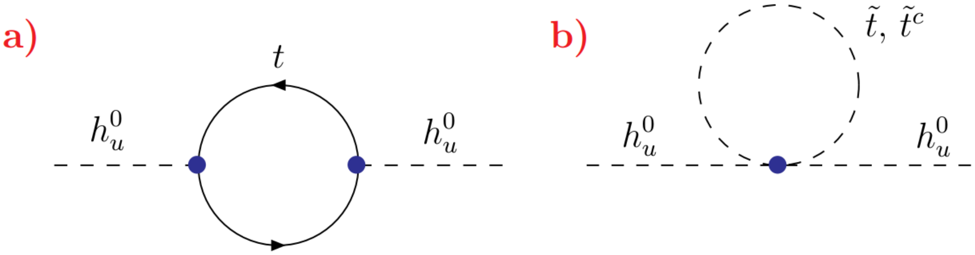

Figure 2.1: One-loop contribution to the Higgs mass involving the top and stops.

following interaction terms involving the SM Higgs:

$$\mathcal{L} \supset -\left(y_t\, h_u^0\, t\, t^c + h.c.\right) - {y_t}^2 \left|h_u^0\, \tilde{t}\right|^2 - {y_t}^2 \left|h_u^0\, \tilde{t}^c\right|^2 \tag{2.4}$$

where h_u^0 is the real scalar component of H_u, and $\tilde{t}$, $\tilde{t}^c$ are superpartners to the top quark (also known as "stops"). Now let us consider the one-loop contributions of these couplings to the Higgs mass squared. For simplicity we focus on the phase of the theory where the electroweak symmetry is unbroken and the top quarks are massless. The relevant diagrams are shown in Figure 2.1. Keeping only terms which are non-vanishing as $\Lambda_{UV} \to \infty$, Figure 2.1.a gives [37]:

$$\Delta {m_{h_u^0}}^2 = -\frac{3{y_t}^2}{8\pi^2} {\Lambda_{UV}}^2, \tag{2.5}$$

while Figure 2.1.b gives [37]:

$$\Delta {m_{h_u^0}}^2 = \frac{3{y_t}^2}{8\pi^2} \left[{\Lambda_{UV}}^2 - 2{m_{\tilde{t}}}^2 \log\left(\frac{\Lambda_{UV}}{m_{\tilde{t}}}\right)\right] \tag{2.6}$$

where we have assumed that $\tilde{t}$ and $\tilde{t}^c$ are degenerate with mass $m_{\tilde{t}}$. Combining these contributions, we see that the $\mathcal{O}({\Lambda_{UV}}^2)$ terms cancel exactly in $\Delta {m_{h_u^0}}^2$. This exact cancellation is not ad hoc; rather it is enforced by the underlying Supersymmetric structure of the theory that relates the coupling in Figure 2.1.a to the coupling in Figure 2.1.b. Repeating this exercise for the other couplings in (2.2), one obtains the general result that $\mathcal{O}({\Lambda_{UV}}^2)$ contributions to $\Delta {m_{h_u^0}}^2$ cancel in the MSSM. This shows explicitly that the MSSM solves the naturalness/hierarchy problem discussed in Chapter 1.

One might have noticed that Figure 2.1 results in $\Delta {m_{h_u^0}}^2 \sim \mathcal{O}({m_{\tilde{t}}}^2)$. If $m_{\tilde{t}}$ is much greater than $\mathcal{O}(100)$ GeV, the MSSM then suffers from its own naturalness/hierarchy problem. The increasing hierarchy between M_Z, M_W and $m_{\tilde{t}}$ implied by experimental bounds on superpartners is referred to as the "little hierarchy problem". See [39] for an explanation of how this problem may be addressed in comapctified string theories.

2.1.2 $SU(5)$ Grand Unification

We briefly discuss the topic of grand unified theories (GUT's). In the MSSM, it is well known that the $SU(3) \times SU(2)_W \times U(1)_Y$ gauge couplings precisely unify at high renormalization scales corresponding to $Q \sim 10^{16}$ GeV (typically referred to as the GUT scale). Moreover, the chiral superfields which comprise the Standard Model fit neatly into complete representations[6] of $SU(5)$ and form an anomaly-free set. This gives compelling evidence that the MSSM descends from an $SU(5)$ GUT which is broken to its $SU(3) \times SU(2) \times U(1)$ subgroup at the GUT scale. This is a well studied topic in particle physics; see [40] for a review. For the G_2-MSSM models discussed later in this chapter, we will assume that the MSSM is embedded in an $SU(5)$ GUT. For technical details regarding this embedding we refer the reader to [5, 7].

2.1.3 Supersymmetry Breaking

If SUSY is unbroken in nature, SUSY particles would be degenerate in mass with their Standard Model partners. This is in clear contradiction with a litany of experimental constraints. Thus for the MSSM to be phenomenologically viable, there must be some source of SUSY breaking. The couplings which break SUSY must be dimensionful in order to maintain the UV insensitivity discussed in Section 2.1.1; this is referred to as soft SUSY breaking. One potential source of SUSY breaking is the Higgs mechanism. However if the Higgs *vev* is the only source of SUSY breaking, the down-type squarks and sleptons would be tachyonic. This leads us to the conclusion that some dynamics outside of the MSSM must break SUSY to give an experimentally viable theory.

In general, most SUSY breaking models require two ingredients. First, there must be some "hidden" sector in which dynamical SUSY breaking occurs. Second, there must be some mediators that communicate this hidden sector SUSY breaking to the MSSM. In string compactifications such as the model discussed in Section 2.2, dynamical SUSY breaking is induced by moduli stabilization. SUSY breaking is then mediated to the MSSM via gravitational interactions. These interactions manifest in the effective theory as Planck suppressed Kahler potential operators coupling moduli fields to MSSM fields. This type of SUSY breaking mechanism is referred to as gravity mediation in the literature. We will give an example of this mechanism in Section 2.2 in the context of the G_2-MSSM.

---

[6] This is not quite true for the Higgs fields, which require additional color triplets to form complete representations of $SU(5)$. These additional triplets must have masses of order the GUT scale to preserve gauge coupling unification, while the Higgs fields must be much lighter. This is known as the "doublet-triplet splitting" problem.

2.2 Moduli Stabilization and Supersymmetry Breaking in the G_2-MSSM

In this section we discuss the mechanisms for moduli stabilization and SUSY breaking in the G_2-MSSM. As stated in Chapter 1, this model is inspired by M-theory compactified on a 7D manifold of G_2 holonomy. The compact 7D manifold must have G_2 holonomy in order to preserve $\mathcal{N} = 1$ SUSY in the 4D theory [41]. Otherwise the compactification to 4D would itself break SUSY, resulting in Planck scale superpartners. This would reintroduce the naturalness/hierarchy problem as per the discussion in Section 2.1.

Given a compact 7D manifold with a G_2 holonomy group, the additional geometric structure required for a realistic 4D theory (non-abelian gauge group, chiral fermions, etc.) was explored in [1, 2, 3, 4, 5, 6, 7, 8]. We will not discuss these subtleties, and instead assume that the compact G_2 manifold contains all the necessary geometric features to reproduce the gauge and matter content of the Standard Model. This will allow us to focus on the 4D effective $\mathcal{N} = 1$ Supergravity (SUGRA) theory[7], which in turn maps onto the MSSM as its low energy limit. From this perspective we will show how the presence of non-abelian hidden sectors can stabilize all moduli fields and break SUSY. As stated in the beginning of this chapter, this section is mostly a review of previous work done in [27, 28, 29, 34].

Of particular importance for gravity mediation is the gravitino, the spin-3/2 superpartner to the graviton predicted by SUGRA. The gravitino mass $M_{3/2}$ can be thought of as the order parameter for SUSY breaking, as the gravitino would be degenerate with the massless graviton if SUSY were unbroken. In models with gravity mediated SUSY breaking, the soft SUSY breaking scalar masses are to lowest order equal to the gravitino mass [42]. In the following, we will approximately calculate $M_{3/2}$ from moduli stabilization. For the remainder of this section we will use Planck units i.e. $m_{pl} = 1$.

2.2.1 Moduli and Matter Kahler Potential

In G_2 compactifications of M-theory, the moduli fields s_i in the effective 4-D theory arise from Kaluza-Klein (KK) zero modes of the covariantly constant 3-form Φ, which is uniquely determined by the metric of the G_2 manifold X. Note that the 3-form Φ is real, such that the moduli fields s_i are real scalar fields in 4-D. The moduli Kahler potential can be inferred

---

[7] In simple terms, SUGRA can be obtained from SUSY simply by promoting Supersymmetry transformations to a local (as opposed to global) symmetry. This is reminiscent of how GR can be obtained by promoting the global Poincare symmetry to a local one. In practice, the resulting SUGRA Lagrangian is quite complicated; the technical details are beyond the scope of both this thesis and the author's expertise.

from the classical moduli space metric to be[43]:

$$\hat{K} = -3 \log 4\pi^{1/3} V_X \tag{2.7}$$

where V_X is the volume of the G_2-manifold in 11-d Planck units:

$$V_X = \frac{1}{7} \int_X \Phi \wedge *\Phi. \tag{2.8}$$

Without explicit knowledge of the metric for a particular G_2 manifold, the functional form for V_X in terms of the moduli fields s_i can not be determined. However, it is possible to argue on general grounds that V_X is a homogeneous function of degree $7/3$ in the moduli s_i, in other words $V_X \to A^{7/3} V_X$ if the moduli are scaled by a common factor $s_i \to A\, s_i$. Using this homogeneity property, one can derive the identity:

$$\sum_{i=1}^{N} s_i \hat{K}_i = -7 \tag{2.9}$$

where $\hat{K}_i \equiv \partial \hat{K} / \partial s_i$. We will use this homogeneity property in Section 2 to derive general results from moduli stabilization without needing to specify a particular form for V_X.

The Kahler potential for the matter fields is given by:

$$K = \kappa(s_i) \frac{QQ^\dagger}{V_X} \tag{2.10}$$

where Q represents some chiral matter supermuliplet and $\kappa(s_i)$ is a scale-invariant function of the moduli s_i. This form for the Kahler potential was motivated in Section III of [34] by three independent arguments: (i) dimensional reduction, (ii) locality of the physical Yukawa couplings and (iii) matching KK threshold corrections to the 4-D gauge coupling[44] in the effective $\mathcal{N} = 1$ supergravity (SUGRA) theory. For brevity we will not reproduce these arguments here.

2.2.2 Moduli Superpotential

In order to preserve $\mathcal{N} = 1$ SUSY in the effective Lagrangian, the real moduli fields s_i must have combined with some other scalar degree of freedom in order to form the complex scalar component of some chiral mutliplet. Such scalar degrees of freedom arise from the KK zero-modes of the real 3-form C-field present in 11-dimensional supergravity. The complexified moduli z_i can be expressed as the zero-modes of the "complexified" 3-form

$\Phi + iC$:

$$C + i\Phi = \sum_{i=1}^{b^3(X)} (a_i + is_i)\,\phi_i = \sum_{i=1}^{b^3(X)} z^i \phi_i \tag{2.11}$$

where ϕ_i represent harmonic 3-forms $\phi_i \in H^3(X, \mathrm{Z})$ and $b^3(X)$ is the 3rd Betti number of the G_2 manifold. From explicit constructions of smooth G_2-manifolds we expect $b^3(X) \sim \mathcal{O}(100)$.

The a_i, which are the scalar zero-modes of C, are axionic as they inherit a shift symmetry in the 4-D effective theory from the underlying higher-dimensional gauge symmetry of the C-field. This provides a very important M-theoretic input for the 4-D effective lagrangian, namely that *polynomials of the complexified moduli fields can not appear in the superpotential*, assuming that the axionic shift symmetry is violated only by non-perturbative effects. In order to stabilize the moduli s_i, we must assume the presence of non-Abelian “hidden sector” gauge groups in addition to the Standard Model one. In G_2 compactifications of M-theory, non-Abelian gauge fields are localized along 3-dimensional submanifolds which parameterize families of ADE orbifold singularities[45, 2]. Thus requiring the presence of hidden sectors is equivalent to assuming that there are some other 3-cycles in the G_2 manifold which support non-Abelian gauge fields, in addition to the visible sector 3-cycle which supports the SM gauge fields. Because two 3-cycles will generically not intersect in a 7-dimensional space, we assume no light matter charged under both the visible and hidden sector gauge groups and thus SUSY breaking will be gravity mediated.

In the presence of a pure $SU(Q)$ super Yang-Mills (SYM) hidden sector[8], non-perturbative dynamics generate an effective moduli superpotential of the form $W = Am_{pl}^3 e^{i2\pi bf}$ where f is the hidden sector gauge kinetic function $f = \sum_i N_i z_i$ and $b = 1/Q$. The integers N_i are determined by the homology class of the 3-cycle. Such a superpotential will stabilize all moduli; however the presence of only a single hidden sector may not yield vacuaa which are within the supergravity approximation ($V_X \gg 1$ in 11-D Planck units). Introducing another pure SYM hidden sector such that $W = m_{pl}^3 \left(A_1 e^{i2\pi b_1 f_1} + A_2 e^{i2\pi b_2 f_2} \right)$ will stabilize moduli within the supergravity approximation, but gives only AdS vacuaa. In order to obtain de Sitter vacua with moduli stabilized in a region where the supergravity approximation is valid, at least one hidden sector $SU(P+1)$ gauge group with charged matter is required. It was discussed in [46] how chiral matter charged under a particular gauge group naturally arises from isolated conical singularities in the G_2 manifold. Note the introduction of the $SU(Q)$ and $SU(P+1)$ gauge groups here; they will be referred to extensively below.

---

[8] Super Yang-Mills describes Supersymmetric theories in which the only particles are the gauge bosons and gauginos of a non-abelian gauge group.

In the minimal setup, we assume that there are two hidden sectors; an $SU(Q)$ pure SYM hidden sector, and a $SU(P+1)$ hidden sector with $N_f = 1$ flavor of fundamental + antifundamental chiral multiplets. The Affleck-Dine-Seiberg effective superpotential [47] is then given by:

$$W = A_1 \phi^{-2b_1} \, e^{i2\pi b_1 f_1} + A_2 \, e^{i2\pi b_2 f_2} \tag{2.12}$$

where $b_1 = 1/P$, $b_2 = 1/Q$, f_1, f_2 are the gauge kinetic functions of the $SU(P+1)$ and $SU(Q)$ hidden sectors, and A_1 and A_2 represent instanton prefactors. ϕ represents the $Q\overline{Q}$ meson condensate in $SU(P+1)$ sector. There in principal will be other gauge groups which also contribute non-perturbative superpotential terms. However their contribution to W will scale like $W \propto e^{i2\pi f/\left(N-N_f\right)}$, so hidden sectors with large $N - N_f$ will provide the dominant contribution to $\langle W \rangle$ while other smaller rank hidden sectors will provide a subdominant contribution to $\langle W \rangle$ and can be neglected in the moduli stabilization analysis.

2.2.3 Moduli Stabilization and Determining $M_{3/2}$

From the discussion in the preceding section, we have argued that in G_2 compactifications of M-theory motivate the following forms for the Kahler potential and moduli superpotential in the effective theory:

$$\begin{aligned} K &= -3 \log 4\pi^{1/3} V_X + \kappa_h(s_i) \frac{\phi \phi^\dagger}{V_X} \\ W &= A_1 \phi^{-2b_1} \, e^{i2\pi b_1 f_1} + A_2 \, e^{i2\pi b_2 f_2} \end{aligned} \tag{2.13}$$

where again we take ϕ to be the $SU(P+1)$ hidden sector meson condensate. We have neglected visible sector fields, as they do not develop *vev*'s at this stage and are thus irrelevant for the moduli stabilization analysis. In the following analysis we assume that 3-cycles which support the $SU(Q)$ and $SU(P+1)$ gauge groups are equivalent in cohomology so that $f_1 = f_2 \equiv f$. This simplifies the moduli stabilization analysis; the more general case is considered in [48]. Given W and K in (7), we can now compute the scalar potential for the effective 4-D $\mathcal{N} = 1$ SUGRA Lagrangian:

$$V = e^K \left(g^{n\overline{m}} F_n \overline{F}_{\overline{m}} - 3 \left| W \right|^2 \right) \tag{2.14}$$

where the Kahler metric $g_{n\overline{m}}$ is obtained in the usual way by differentiating K with respect to the moduli and meson fields. The resulting form of the Kahler potential in terms of the moduli fields along with the minimization conditions are rather cumbersome, so we will not reproduce them here. The details are provided in pages 21-25 of [34]. Here we simply recapitulate the main points of the analysis, which in particular demonstrates that solutions with stabilized moduli exist.

The stabilized moduli *vev*'s are given by the following ansatz:

$$s_i = \frac{a_i}{N_i}\frac{3}{7}V_Q \tag{2.15}$$

where V_Q is the volume of the hidden sector gauge kinetic functions, $V_Q \equiv Im(f) = \sum_i N_i s_i$. The a_i are defined as $3a_i \equiv -s_i\, \partial\hat{K}/\partial s_i$, and given an explicit form for V_X their value at the de Sitter minimum can be obtained by solving the following transcendental equation:

$$\frac{\partial \hat{K}}{\partial s_i}\Big|_{s_i=a_i/N_i} = -3N_i. \tag{2.16}$$

Regardless of the form for V_X, the homogeneity property (3) implies $\sum a_i = 7/3$. Given the ansatz (9) for s_i, one can numerically solve for the value of V_Q which satisfies the moduli stabilization equations. A good approximation for V_Q is given by:

$$V_Q = \frac{1}{2\pi}\frac{PQ}{Q-P}\log\left(\frac{QA_1\phi_0^{-2/P}}{PA_2}\right) \tag{2.17}$$

in the limit where $V_Q \gg 1$. In a regime where the supergravity approximation is valid $V_X \gg 1$; since the homogeneity properties of V_X imply $V_X \propto s^{7/3}$, we expect $s_i \gg 1$ and thus $V_Q = \sum N_i s_i \gg 1$ if the supergravity approximation is valid.

Given the ansatz (9) along with the homogeneity property $\sum_i a_i = 7/3$, the value of the scalar potential (8) at the minimum to lowest order in $\mathcal{O}(1/{P_{eff}}^2)$ is given by:

$$\begin{aligned}\frac{V_0}{M_{3/2}^2} =& \Big[\left(\frac{2}{Q-P}+\frac{\phi_0^2}{V_X}\right)^2 \\ &+ \frac{14}{P_{eff}}\left(1-\frac{2}{3(Q-P)}\right)\left(\frac{2}{Q-P}+\frac{\phi_0^2}{V_X}\right) - 3\frac{\phi_0^2}{V_X}\Big]\frac{V_X}{\phi_0^2}\end{aligned} \tag{2.18}$$

where we have defined:

$$P_{eff} = P\log\left(\frac{QA_1\phi_0^{-2/P}}{PA_2}\right). \tag{2.19}$$

Thus the superpotential coefficients A_1 and A_2 have been absorbed into our definition of P_{eff}. Note from (11) that $V_Q \approx P_{eff}Q/2\pi(Q-P)$, so $V_Q \gg 1$ ensures $P_{eff} \gg 1$.

We now require that the minimization condition for the meson condensate ϕ_0 causes the tree level scalar potential (12) to vanish. To leading order in $1/P_{eff}^2$, this imposes the requirement that[9]:

$$P_{eff} = \frac{14(3(Q-P)-2)}{3(3(Q-P)) - 2\sqrt{6(Q-P)}}. \tag{2.20}$$

Thus given particular values of Q and P, imposing a vanishing cosmological constant actually fixes the ratio A_1/A_2. Put another way, tuning the vacuum energy to zero at tree level upon moduli stabilization is only possible for a particular value of A_1/A_2. Requiring the s_i to be stabilized at positive values requires $P_{eff} > 0$ as can be seen from (9) and (11), which imposes the constraint $Q - P \geq 3$. If (14) is satisfied, then the meson *vev* is obtained by determining the value of ϕ_0 which causes (12) to vanish:

$$\frac{\phi_0^2}{V_X} = \frac{2}{Q-P} + \frac{7}{P_{eff}}\left(1 - \frac{2}{3(Q-P)}\right) + \mathcal{O}(1/P_{eff}^2) \tag{2.21}$$

Thus we have shown that ϕ_0 and s_i are all stabilized by non-perturbative effects from hidden sector strong dynamics. We can now compute the value of the bare gravitino mass from (7)-(14):

$$M_{3/2} = e^{K/2}\,|W| = \frac{e^{\phi_0^2/2V_X}}{8\sqrt{\pi}V_X^{3/2}}\,|P-Q|\,\frac{A_2}{Q}e^{-P_{eff}/(Q-P)}. \tag{2.22}$$

Thus given the ranks of the hidden sector gauge groups $SU(Q)$ and $SU(P+1)$, the value of $M_{3/2}$ is completely determined up to the unknown instanton prefactor A_2. Field theoretic computations[49] indicate that $A_2 = Q$ up to renormalization-scheme dependent and threshold corrections, so we expect $A/Q \lesssim 1$.

Now we examine constraints on the possible values of $Q - P$, which fixes the exponential factor in (16). As discussed, we require $Q - P \geq 3$ so that $V_Q \equiv Im(f) = \sum N_i s_i$ stays positive. From (11), (13) and (14) we see that for $Q - P = 3$, $V_Q \approx 3.37\,Q$ while for $Q - P > 3$, $V_Q < 0.84\,Q$. Recall that for the supergravity approximation to be valid we require $V_X \gg 1$ from which we expect $s_i > 1$. Thus we expect $V_Q = \sum_i N_i s_i \gtrsim N_{mod}$, where N_{mod} is the number of moduli fields. As mentioned in Section 1, from explicit constructions we expect $N_{mod} = b^3(X) \sim \mathcal{O}(100)$, so we roughly expect $V_Q \sim \mathcal{O}(100)$ if the supergravity approximation is valid. Thus the larger the value of $Q - P$, the more difficult it is to stabilize moduli in a region where the supergravity approximation is valid. To ensure the validity of the SUGRA approximation we focus on the case where $Q - P = 3$; the general case will be discussed at the end of this section. This fixes the gravitino mass to be:

$$M_{3/2} \approx 10^6\,(\text{TeV})\,\frac{A_2}{QV_X^{3/2}}. \tag{2.23}$$

---

[9] Note that we are neglecting the ϕ_0 dependence of P_{eff}, due to the smallness of $2/P$ along with the fact that the dependence is logarithmic.

The value of V_X in (17) can be fixed from dimensional reduction arguments by requiring that the 11-D supergravity theory gives the correct value for the 4-D visible sector gauge coupling α_{GUT} at the GUT scale[44]. This constrains V_X to be:

$$V_X \approx 137 L(\mathcal{Q})^{2/3} \tag{2.24}$$

where $L(\mathcal{Q})$ is a topological invariant, related to the analytic torsion of the 3-cycle $\mathcal{Q}$ on which visible sector gauge fields are localized. The dependence of V_X on $L(\mathcal{Q})$ arises from computing KK-threshold corrections to the visible sector gauge coupling. Motivated by triplet-doublet splitting [5], the reference [44] assumes $\mathcal{Q} \cong S_3/Z_q$ in which case $L(\mathcal{Q}) = 4qsin^2\left(5\pi\omega/q\right)$. ω is an integer determined by the geometry of $\mathcal{Q}$ such that $Mod(5\omega, q) \neq 0$. The Poincare conjecture seems to imply that this form for $L(\mathcal{Q})$ is fairly general, but we are still currently working on understanding this issue in more detail. It is also straightforward to compute the scale of gaugino condensation in the $SU(Q)$ SYM hidden sector:

$$\Lambda \sim \frac{e^{-\frac{2\pi}{3Q}V_Q}}{2\pi^{1/6}V_X^{1/2}} \approx \frac{1.1 \times 10^{14}\,\text{GeV}}{L(\mathcal{Q})^{1/3}} \tag{2.25}$$

Assuming $Q - P = 3$ and $L(\mathcal{Q}) = 4qsin^2\left(5\pi\omega/q\right)$, we can combine (17) and (18) to obtain some representative values for $M_{3/2}$, given in Table 1 of [34]. Depending on the values of ω and q, $20\,\text{TeV} \lesssim M_{3/2}\,(A_2/Q) \lesssim 100\,\text{TeV}$. Thus up to the ratio A_2/Q which we expect to be $\lesssim 1$, we have shown with a pure $SU(Q)$ gauge group as well as an $SU(P+1)$ gauge group with $N_f = 1$, setting $Q - P = 3$ and stabilizing moduli naturally gives $M_{3/2} \sim \mathcal{O}(50)$ TeV within about a factor of 2.

We have shown that there exists a generic class of compactified M-theories which naturally give $M_{3/2} \sim 50$ TeV upon moduli stabilization; however a crucial assumption we have made is $Q - P = 3$ to ensure the validity of the supergravity approximation $V_X \gg 1$. It may be in principal possible to find valid solutions with $Q - P > 3$, which will greatly change $M_{3/2}$ due to the exponential sensitivity in (16). However, it is straightforward to show from (14) and (16) that for $Q - P \geq 4$, $P_{eff} \geq 20$, which results in $M_{3/2} \gtrsim 10^{-2} M_{pl}$. Therefore $Q - P = 3$ is the only possibility which allows a solution to the hierarchy problem between $M_{3/2}$ and M_{pl}. In other words, if one demands a solution of the hierarchy problem from moduli stabilization in this framework, $Q - P = 3$ and $M_{3/2} \sim 50$ TeV is a robust prediction. If one takes the appropriate attitude for string phenomenology of looking for a generic set of solutions that could describe our world, with stabilized moduli, the set of solutions that emerges and solves the hierarchy problem has $M_{3/2} \sim 50$ TeV!

2.2.4 Hierarchy between Gaugino Masses and $M_{3/2}$

We now briefly discuss the hierarchy between $M_{3/2}$ and the soft SUSY breaking gaugino masses, namely $M_{1/2}/M_{3/2} \sim 10^{-2}$, which results from the moduli stabilization procedure mentioned in Section 2. The universal tree-level contribution to the gaugino masses from the supergravity Lagrangian is given by[42]:

$$M_{1/2} = \frac{e^{K/2} F^i \partial_i f_{vis}}{2i\, Im(f_{vis})} \tag{2.26}$$

where F_i are the F-terms for the moduli fields s_i and f_{vis} is now the visible sector gauge kinetic function, $f_{vis} = \sum_i N_i^{vis} z_i$. The suppression of $M_{1/2}$ with respect to $M_{3/2}$ arises from a suppression of the moduli F-terms F_i with respect to the hidden sector meson condensate F-term F_ϕ. In particular, the moduli stabilization procedure discussed in the previous section yields the following F-term *vev*'s:

$$\left|e^{K/2} F^i\right| \approx \frac{2s_i}{P_{eff}} M_{3/2}, \;\; \left|e^{K/2} F^\phi\right| \approx \phi\, M_{3/2} \tag{2.27}$$

The moduli stabilization procedure yields $s_i \sim \phi$, and therefore the moduli F-terms are suppressed by $1/P_{eff}$ with respect to the meson condensate F-terms; therefore the meson condensate F-terms dominate the vacuum energy. Since f_{vis} does not depend on the meson condensate ϕ, $\partial_\phi f_{vis} = 0$ and only the smaller moduli F-terms contribute to (20). Consequently, (12) yields:

$$\left|M_{1/2}\right| \approx \frac{1}{P_{eff}} \left(1 + \frac{2V_X}{(Q-P)\phi_0^2}\right) M_{3/2}. \tag{2.28}$$

As discussed in the previous section, for solutions with $Q-P = 3$, $P_{eff} \approx 61$ and $\phi_0^2/V_X \sim 0.5$, and thus $M_{1/2} \approx 0.03\, M_{3/2}$. Thus the universal tree level contribution to gaugino masses from gravity mediation is suppressed relative to $M_{3/2}$. There are also the usual non-universal anomaly-mediated contributions to the gaugino masses, as well as non-universal effects which arise from renormalizing parameters down to the electroweak scale, but they are of the same order of magnitude as the tree level contributions from (20).

This result is significant for LHC phenomenology, as in gravity mediation the soft SUSY breaking scalar masses are all $\mathcal{O}(M_{3/2})$ assuming no sequestering, as is expected to be generic in M-theory compactifications. This implies that all scalar superpartners will have masses $\tilde{m} \sim M_{3/2} \sim$ 10's of TeV, while gauginos will have masses in the $200\,\mathrm{GeV} \lesssim M \lesssim 2$ TeV range (depending on the particular gaugino in question). Thus the compactified M-theory framework yields a robust prediction that scalar superpartners will be out of reach of the LHC, while the gauginos (the gluino in particular) should be light enough to be within kinematic reach. As we have discussed, these predictions are largely insensitive to details regarding the precise mathematical structure of compact G_2 manifolds. In the following chapter, we will discuss in detail the collider signatures resulting from G_2-MSSM spectra, and make the above statements regarding discoverability much more precise.

CHAPTER 3

Collider Predictions of the G_2-MSSM

In Chapter 2 we discussed moduli stabilization and Supersymmetry breaking in the G_2-MSSM, arriving at the important result that the gravitino mass will be ~ 50 TeV with gaugino masses suppressed by roughly 2 orders of magnitude. We however ignored some technical subtleties which must be considered for a precise prediction of the SUSY mass spectrum. First, we only considered the values of mass parameters at a high renormalization scale, $Q \sim M_{GUT}$. These mass parameters must be renormalized down to the electroweak scale for an accurate calculation of physical masses. Second, with respect to the gaugino masses we only discussed tree-level contributions from moduli stabilization. There are also anomaly-mediated contributions [50, 51] which are comparable to the tree-level contributions. These corrections must be taken into account for an accurate prediction of the gaugino mass spectrum.

In this chapter we will address the above subtleties in order to obtain precise benchmark spectra predicted by the G_2-MSSM. This will allow us to perform a detailed study of the collider signatures expected in these models. We also illustrate an example of the "top-down meets bottom-up" approach outlined in Chapter 1 by imposing the measured Higgs mass constraint on the spectra derived in Chapter 2. We discuss how the superpartner spectrum is completely fixed by electroweak symmetry breaking (EWSB), once both the gravitino mass $M_{3/2}$ and the superpotential μ-term are specified. Furthermore, the measured value of the Higgs mass picks out a particular slice in the $(\mu, M_{3/2})$ plane; thus *all* sparticle masses can be fixed by determining either μ or $M_{3/2}$.

To make the discussion of collider physics concrete, we focus on the benchmark value $M_{3/2} = 35$ TeV, which gives a benchmark spectrum with a 1.5 TeV gluino. All sfermion and heavy Higgs masses are of $\mathcal{O}(M_{3/2})$, while the Wino(Bino)-like lighter gauginos have masses of $615(450)$ GeV. The hierarchy between gauginos and $M_{3/2}$ follows from the dynamics of moduli stabilization discussed in Chapter 2. As will be discussed below, this benchmark spectrum is not constrained by LHC-8. Both gluino pair production *and* direct electroweak gaugino production should yield discoveries with $\lesssim 300$ fb $^{-1}$ of LHC-14 data, particularly since electroweak gauginos yield distinctive signatures through $\chi_2^0 \to \chi_1^0 + h$ which has a nearly 100% branching ratio. This bencmark spectrum predicts $\mu \approx 1.4$ TeV, leading to heavy Higgsinos which are out of reach of LHC-14.

We will also discuss implications of the G_2-MSSM for future colliders. Taking the benchmark spectrum, we will show that 1.5 TeV Higgsinos are accessible at both 50 and 100 TeV colliders. Furthermore, the heavier squarks are also accessible at 100 TeV colliders, with hundreds of squark-gluino associated production events expected with $\gtrsim 1000$ fb^{-1} of data. In particular, for a gluino mass of $\sim$ TeV, the cross-section for associated stop-gluino-top production $pp \to \tilde{g} + \tilde{t}_1 + t$, and potentially even sbottom-gluino-bottom $pp \to \tilde{g} + \tilde{b}_1 + b$, can be sizeable at 100 TeV colliders for stops and sbottoms lighter than ~ 20 TeV. This is especially relevant for SUGRA-like theories with universal scalar masses at the GUT scale, in which third generation squarks are expected to be lighter due to RGE (renormalization group equation) effects.

Thus the benchmark spectrum has the remarkable feature that Higgsinos and squarks are accessible at future colliders, despite the scale of SUSY breaking $M_{3/2}$ being in the tens of TeV range. Furthermore, the constrained relationship between SUSY breaking parameters implies that within the G_2-MSSM, *the discovery of a single sparticle is enough to actually measure* $M_{3/2}$. Given the discovery of a single sparticle, the rest of the G_2-MSSM spectrum is determined uniquely, resulting in a multitude of additional predictions which can be readily confirmed or falsified in ongoing and upcoming collider experiments. This point highlights the potential power of top-down approaches in greatly reducing the naive parameter space of Supersymmetry.

This chapter is organised as follows. Section 3.1 gives a brief overview of the G_2-MSSM framework (overlapping slightly with Chapter 2), and discusses how the benchmark spectrum corresponding to $M_{3/2} = 35$ TeV is obtained. Section 3.2 provides the sparticle spectrum and relevant branching ratios corresponding to the benchmark spectrum obtained in Section 3.1. Predictions for LHC-14 are given in Section 3.3, while predictions for future colliders are given in Section 3.4. Finally, we summarize these results in Section 3.5. This chapter is based largely on work done with collaborators in [9].

3.1 Theoretical Framework

We begin by reviewing some features and successes of the compactified M-theory framework. G_2-compactifications of M-theory provide a natural setting for full moduli stabilisation and broken $\mathcal{N} = 1$ Supersymmetry in a deSitter vacuum while also solving the gauge hierarchy problem, as discussed in Chapter 2. Additionally, EDM [52, 53] and flavour constraints (such as $B_s \to \mu\mu$) [54] are avoided. However, it may not explain $(g-2)_\mu$, while the strong CP problem is solved by the axionic components of moduli fields [55]. The presence of late-decaying moduli results in a non-thermal cosmological history which solves the moduli problem and the gravitino problem [56]. Since the baryon asymmetry and the dark matter both arise from moduli decay (including axions), the ratio of baryonic matter to dark matter is calculable [57]. R-parity conservation is expected [58]; thus consistency with the observed DM relic abundance implies that the visible sector LSP will decay to hidden sector DM particles [11][1]. μ is incorporated into the theory following the proposal of Witten [5] and including effects of moduli stabilisation [61]. Calculations in this framework anticipated the mass and decay branching ratios of the Higgs boson observed at the LHC [31].

A key result of the aforementioned references is that once moduli stabilization breaks Supersymmetry and cancels the vacuum energy at tree level, the relationship between SUSY breaking parameters becomes very constrained. Upon moduli stabilization and SUSY breaking, the soft breaking parameters at the renormalization scale $Q \sim M_{GUT}$ are given by [34]:

$$\begin{aligned} &m_0^2 \approx M_{3/2}^2\left(1-C\right), \quad A_0^2 \approx 1.5 M_{3/2}\left(1-C\right), \\ &M_a \approx \left[-0.032\eta + \alpha_{GUT}\left(0.034\left(3C_a - C_a'\right) + 0.079 C_a'(1-C)\right)\right] \times M_{3/2} \end{aligned} \tag{3.1}$$

where $C_a = (0, 2, 3)$ and $C_a' = (33/5, 7, 6)$. m_0 and A_0 are universal soft scalar masses and trilinears, and "C" parameterizes higher order Kähler potential corrections arising from higher dimensional operators as defined in [34]. The quantity η parameterizes KK-threshold corrections to the unified gauge coupling; we will argue in Section 3.1.2 that $\eta \sim 1$, unless the geometry of the G_2 manifold becomes incredibly complicated. The hierarchy between gaugino masses and $M_{3/2}$ arises because $M_{3/2}$ feels contributions from both hidden sector meson and moduli F-terms, while M_a feels contrbutions from only the moduli F-terms which are suppressed by approximately $\alpha_{GUT} \approx 1/25$ with respect to the meson F-terms. See Section 2.2 for a more detailed discussion of this point. Note that (3.1) is more precise than the results derived in Section 2.2, as here we have included both the contribution from Kahler potential corrections as well as the anomaly-mediated [50, 51] contribution to the gaugino masses.

Thus the *entire* sparticle spectrum is essentially fixed once $M_{3/2}$, μ and C are specified. We will show in Section 3.1.1 that imposing consistent EWSB along with the measured

---

[1] For non-thermal cosmologies, a stable Bino-LSP will overclose the universe, while a stable Wino-LSP is in tension with indirect detection contraints [59, 60].

value of the Higgs mass $M_h = 125.2 \pm 0.4$ GeV [62, 63] reduces the 3D space of allowed $(M_{3/2}, \mu, C)$ values to an approximately one-dimensional space. As a result, the entire sparticle spectrum is completely determined for a given value of $M_{3/2}$. In Section 3.1.2 we will use top-down considerations to approximately calculate $M_{3/2}$, giving a central value of $M_{3/2} \approx 35$ TeV which we use to obtain the benchmark spectrum considered in Section 3.2 and onwards.

3.1.1 Imposing Constraints: EWSB and the Higgs Mass

In the previous section, we have stated that the sparticle spectrum is essentially determined by three quantities: $M_{3/2}$, μ, C, or equivalently $M_{3/2}, \mu/M_{3/2}, C$. In principle, these quantities are calculable from the full UV theory. In practice however, there are theoretical uncertainties which preclude a full top-down calculation. Instead, we will show in this section how bottom-up constraints of EWSB along with the measured Higgs mass provide two independent constraints, reducing the naive 3D region to a one-dimensional strip. This illustrates the power of combining top-down calculations with known bottom-up constraints to increase the predictiveness of a particular theory.

A detailed discussion of how the constraints from EWSB and $M_h = 125.2 \pm 0.4$ GeV are imposed is given in Appendix A; the result is shown in Figure 3.1. One can see that EWSB constraints restrict the region to an approximately 2D-slice. Imposing the constraint $M_h = 125.2 \pm 0.4$ reduces this slice to a thin band; the thickness of this band is due primarily to experimental uncertainties on M_h, M_t and α_s [31]. The range $0 < \mu/M_{3/2} \lesssim 0.1$ is motivated by both top-down [61] and little hierarchy [64] arguments; this is discussed in more detail in Appendix A.

Upon imposing these bottom-up constraints, the entire sparticle spectrum becomes an approximately one-dimensional strip in the original 3D space. In the next section, we take the perspective that Figure 3.1 fixes the entire spectrum in terms of $M_{3/2}$, and use equation (2.23) to motivate the benchmark value $M_{3/2} = 35\,\text{TeV}$ and obtain the associated benchmark spectrum.

3.1.2 Obtaining a Benchmark Spectrum

Having established that the entire Supersymmetric particle spectrum is essentially determined for a given value of $M_{3/2}$, we discuss how $M_{3/2}$ can be approximately computed from the UV theory. Upon moduli stabilization and SUSY breaking, the standard Super-

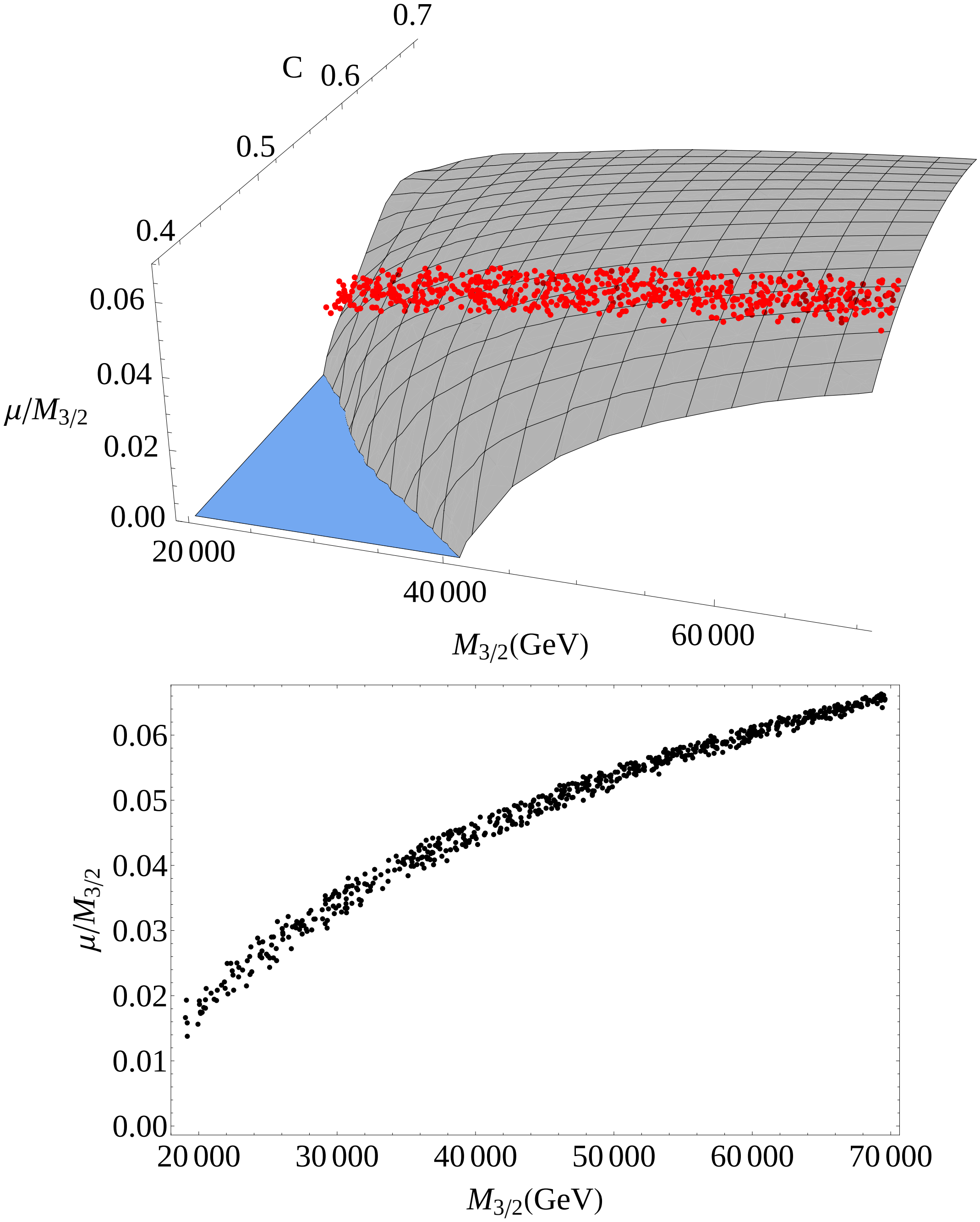

Figure 3.1: **Upper Figure**: The dark gray surface shows the slice of $M_{3/2}, c, \mu/M_{3/2}$ parameter space which satisfies EWSB, while red points also satisfy the Higgs mass constraint $M_h = 125.2 \pm 0.4$ GeV. The blue shaded region corresponds to points which are inconsistent with $\mu/M_{3/2} \lesssim 0.1$; see the Appendix for further discussion. In these plots, μ is defined at the renormalization scale $Q^2 = m_{\tilde{t}_1} m_{\tilde{t}_2}$. The mesh lines are added for perspective, and do not have any physical significance.
Lower Figure: A projection of the upper figure onto the $M_{3/2} - \mu/M_{3/2}$ plane.

gravity expression for the gravitino mass gives [34] :

$$M_{3/2} \approx \frac{9 \times 10^5}{V_X^{3/2}} \left(\frac{A_2}{Q}\right) \text{TeV} \tag{3.2}$$

where Q is the rank of a hidden sector $SU(Q)$ gauge group which undergoes gaugino condensation, and A_2 is the corresponding non-perturbative superpotential coefficient. V_X is the volume of the G_2-manifold in 11-D Planck units. This expression was explicitly derived in Section 2.2; see (2.23) and the surrounding text for details.

In principle, V_X is a function of the moduli fields and is thus calculable once moduli are stabilized. However the particular expression for V_X in terms of moduli fields is not fully known; we can instead fix V_X by ensuring that dimensional reduction to 4D gives the correct value for Newton's constant [7]. This fixes V_X to be [34]:

$$V_X \approx 137.4\, L(\mathcal{Q})^{2/3}, \quad L(\mathcal{Q}) = 4q\, \sin^2\left(\frac{5\pi\omega}{q}\right) \tag{3.3}$$

where $L(\mathcal{Q})$ is a topological invariant which parameterizes threshold corrections from Kaluza-Klein states. This form for $L(\mathcal{Q})$ was computed in [7], assuming that the visible sector $SU(5)$ gauge fields are compactified on a Lens space $\mathcal{Q} \cong S_3/Z_q$ in the presence of a non-trivial Wilson line. $5\,\omega$ is an integer parameterizing the effect of the Wilson line, as will be discussed below.

To proceed, we briefly review the motivation for considering $SU(5)$ gauge theories compactified on a Lens space $\mathcal{Q}$. In G_2-compactifications of M-theory, non-abelian gauge fields arise from co-dimension 4 ADE singularities and thus propogate on a 7-dimensional manifold $\mathcal{H}$ [1]. In our notation, we take $\mathcal{H} \cong \mathcal{Q} \times M$ where M is our Minkowski spacetime. Starting from an $SU(5)$ GUT theory, the issues of GUT breaking and doublet-triplet splitting must be resolved for a realistic model. As pointed out by Witten, both problems are elegantly solved in the presence of a non-trivial Wilson line background [5], which breaks $SU(5)$ to the SM while admitting a geometric symmetry which solves doublet-triplet splitting.

The resulting symmetry is determined by the fundamental group of $\mathcal{Q}$, which for $\mathcal{Q} \cong S/Z_q$ is simply Z_q. The non-trivial Wilson line gives the $\int d^2\theta \mu H_u H_d$ superpotential term charge 5ω under Z_q, while $\int d^2\theta M T_u T_d$ is uncharged. However, realistic phenomenology requires non-zero μ, which implies that Z_q is broken once moduli with charge 5ω obtain *vev*'s [61]. If Z_q is completely broken, higher-dimensional Kähler potential operators will generate dangerous lepton-number violating operators which generically violate neutrino mass bounds [58]. Thus Z_q must be broken to a non-trivial subgroup Z_p, where:

$$p = \mathrm{GCD}(q, 5\omega), \quad p \neq 1 \tag{3.4}$$

The simplest case which satisfies these requirements is therefore the case where $p = 4$ and $5\omega = 2$, corresponding to the Lens space S_3/Z_4 and an unbroken Z_2 symmetry once a non-zero μ term is generated. For our benchmark spectrum, we take these values and obtain from (3.2), (3.3):

$$M_{3/2} \approx 35 \left(\frac{A_2}{Q}\right) \text{ TeV}. \tag{3.5}$$

Note that this also fixes η in (3.1) [7]:

$$\eta = 1 - \frac{5\alpha_{GUT}}{2\pi} \ln\left(\frac{L(Q)}{q}\right) \approx 0.956 \tag{3.6}$$

We see that $1-\eta$ is loop suppressed, and can only be $\mathcal{O}(1)$ for $q \gtrsim 100$. This validates our earlier claim that one naturally expects $\eta \sim 1$.

The only remaining undetermined factor in our benchmark spectrum is A_2/Q in (3.5). In the context of Supersymmetric field theories, the precise normalization $A_2 = Q$ [47] in the $\overline{DR}$ scheme was determined by requiring the consistency of various techniques used to study non-perturbative SUSY gauge theories [49]. However, in the present context there may be UV threshold corrections which modify the relation $A_2/Q = 1$. To obtain the benchmark spectrum, we retain $A_2/Q = 1$, which gives $M_{3/2} = 35$ TeV. Imposing constraints from EWSB and M_h for this benchmark value fixes $C \approx 0.52$ and $\mu \approx 1.4$, resulting in the benchmark spectrum discussed in Section 3.2. Figure E.1 illustrates the effect of relaxing this assumption; the gluino mass is plotted for $0.6 \lesssim A_2/Q \lesssim 1.4$, corresponding to $20\,\text{TeV} \lesssim M_{3/2} \lesssim 50$ TeV. $M_{3/2} = 20$ TeV may barely avoid tension with BBN constraints [65], depending on the particular values of moduli couplings and T_{RH}.

In order to obtain a very approximate lower bound on $M_{\tilde{g}}$, we use the `FastLim` [66] package. The program currently only implements some of the possible event topologies, and does not yet implement cascade decays such as $\tilde{g} \to qq\chi_2^0 \to qqh\chi_1^0$. Therefore, when using `FastLim` we treat the aforementioned cascade decays as $\tilde{g} \to qq\chi_2^0 \to qq\chi_1^0$, neglecting additional objects from $\chi_2^0 \to \chi_1^0 + h$. This simplification obviously reduces sensitivity to searches involving high (≥ 6) jet multiplicity. Using this method, we obtain the approximate bound $M_{\tilde{g}} \gtrsim 1.1$ TeV in the compactified M-theory framework, though clearly a more precise analysis is desirable. Nonetheless, the benchmark spectrum with a 1.5 TeV gluino mass sits comfortably outside the excluded region, as we will discuss in Section 3.2.

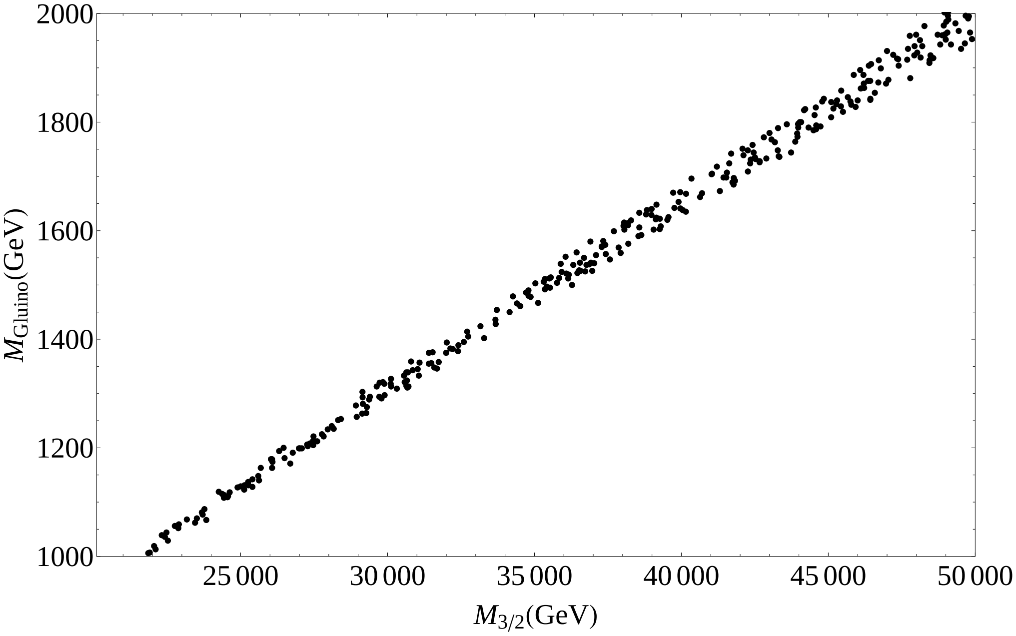

Figure 3.2: Gluino mass vs $M_{3/2}$ for points which satisfy EWSB and Higgs mass constraints, i.e. the red points in Figure 3.1.

3.2 The spectrum and the branching ratios

In this section we present the benchmark spectrum that results from the theoretical framework presented in Section 3.1. In the compactified M-Theory all scalars are generically of order the gravitino mass, with the universal scalar mass given by $m_0 \sim \mathcal{O}(1)M_{3/2}$. We use the computing package `SOFTSUSY` [67] to do two-loop RGE evolution of the high scale soft parameters to obtain sparticle pole masses.

We compute the branching ratios for the decays of some of the superpartners using `SDECAY` [68], which are given in Table 3.1. We focus in particular on the superpartners that we expect to see at the LHC or at future colliders.

Since the squark masses are of $\mathcal{O}(M_{3/2})$ at the high scale, they are not detectable at the LHC. RGE running splits the squarks to give the physical spectrum shown in Fig. 3.3. The neutralinos χ_1^0 (χ_2^0) are Bino (Wino)-like, while χ_3^0, χ_4^0 are Higgsino-like. Note that the mixing angles in the neutralino and chargino sectors are small, as $\mu \gg M_W, M_Z$. In previous studies of the G_2-MSSM, the LSP was taken to be Wino-like, as a Wino-LSP serves as a good DM candidate in string-motivated non-thermal cosmologies [69]. However, obtaining a Wino-like as opposed to a Bino-like LSP requires large KK-threshold corrections to GUT scale gaugino masses (see e.g. [70]), which we argued is unnatural in

---

[2] For details regarding how the Higgs mass is calculated, we refer the reader to Appendix A.

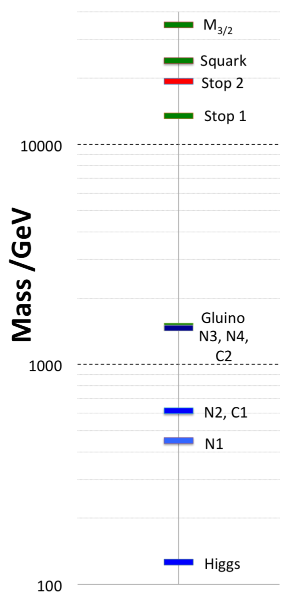

Particle	Mass (GeV)
m_0	24200
$M_{3/2}$	35000
$\tilde{q}_{L,R}$	24000
$\tilde{t}_2$	19300
$\tilde{t}_1$	13500
$\tilde{b}_2$	23900
$\tilde{b}_1$	19300
$\tilde{g}$	1500
χ_1^0	450
χ_2^0	614
χ_3^0	1460
χ_4^0	1460
$\chi_1^\pm$	614
$\chi_2^\pm$	1460
h	125.2[2]

Figure 3.3: Spectrum given GUT scale input values calculated from the theory for the central value $M_{3/2} = 35\,\mathrm{TeV}$. This spectrum has the GUT scale inputs $m_0 \approx 24$ TeV and $A_0 \approx 25$ TeV, where m_0 and A_0 are respectively the universal scalar mass and soft-breaking trilinear. The GUT scale gaugino masses are $M_1 = -1020\,\mathrm{GeV}$, $M_2 = -730\,\mathrm{GeV}$, $M_3 = -590\,\mathrm{GeV}$. Details on how this spectrum was derived are presented in Section 3.1. For the gaugino masses and trilinear, we take the sign convention opposite to that of `SOFTSUSY` . This relative sign affects the 2-loop term in the gaugino mass RGE's which is proportional to A_t.

Section 3.1. In this chapter, we assume that any would-be Bino-like LSP relic abundance decays to a hidden sector DM candidate, but the LSP is sufficiently long-lived to appear stable on collider scales.

Of note is the 100 % branching ratio of $\chi_1^\pm \to \chi_1^0 W^\pm$, and the 98.7 % branching ratio of $\chi_2^0 \to \chi_1^0 h$. Note that the $\chi_2^0 \to \chi_1^0 Z$ decay width is subdominant to that of $\chi_2^0 \to \chi_1^0 h$. This can be explained as follows. The $\chi_2^0 \chi_1^0 h$ coupling arises from couplings of the form $\tilde{W}^0 \tilde{H} h$ and $\tilde{B}^0 \tilde{H} h$ in the gauge eigenstate basis. Since χ_1^0 and χ_2^0 are Bino and Wino-like, the $\chi_2^0 \to \chi_1^0 h$ amplitude is suppressed by a single power of gaugino-Higgsino mixing angles, $\mathcal{O}(M_Z/\mu)$. In contrast, in the gauge eigenstate basis only Higgsinos couple directly to Z via couplings of the form $Z_\mu \tilde{H}^\dagger \bar{\sigma}^\mu \tilde{H}$. Thus the $Z_\mu \chi_1^{0\dagger} \bar{\sigma}^\mu \chi_2^0$ coupling is suppressed by two powers of gaugino-Higgsino mixing angles, resulting in a suppresion of the $\chi_2^0 \to \chi_1^0 Z$

Decay	BR (%)
$\tilde{g} \to \chi_1^{+} q_{1,2}\bar{q}_{1,2}$	25
$\tilde{g} \to \chi_1^{\pm} b\bar{t},\ t\bar{b}$	23
$\tilde{g} \to \chi_1^0 t\bar{t}$	20
$\tilde{g} \to \chi_2^0 q_{1,2}\bar{q}_{1,2}$	12
$\tilde{g} \to \chi_1^0 q_{1,2}\bar{q}_{1,2}$	8
$\tilde{g} \to \chi_2^0 b\bar{b}$	7
$\tilde{g} \to \chi_2^0 t\bar{t}$	4
$\tilde{g} \to \chi_1^0 b\bar{b}$	1

Decay	BR (%)
$\chi_4^0 \to \chi_1^{\pm} W^{\mp}$	60
$\chi_4^0 \to \chi_2^0 h$	27
$\chi_4^0 \to \chi_1^0 h$	8
$\chi_4^0 \to \chi_2^0 Z$	4
$\chi_4^0 \to \chi_1^0 Z$	2
$\chi_3^0 \to \chi_1^{\pm} W^{\mp}$	60
$\chi_3^0 \to \chi_2^0 Z$	26
$\chi_3^0 \to \chi_1^0 Z$	8
$\chi_3^0 \to \chi_2^0 h$	4
$\chi_3^0 \to \chi_1^0 h$	2
$\chi_2^0 \to \chi_1^0 h$	98
$\chi_2^0 \to \chi_1^0 Z$	2

Decay	BR (%)
$\chi_2^{\pm} \to \chi_1^{\pm} h$	31
$\chi_2^{\pm} \to \chi_1^{\pm} Z$	30
$\chi_2^{\pm} \to \chi_2^0 W^{\pm}$	30
$\chi_2^{\pm} \to \chi_1^0 W^{\pm}$	9
$\chi_1^{\pm} \to \chi_1^0 W^{\pm}$	100

Table 3.1: Branching ratios of gluino, neutralinos and charginos. The numbers don't add to 100 in the case of the χ_4^0 branching ratios due to rounding errors.

amplitude by $\mathcal{O}(M_Z^2/\mu^2)$.

Note that this spectrum with a 1.5 TeV gluino should not have been discovered at LHC-8. In simplified models with decoupled squarks, the strongest limits on the gluino production come from multijet + MET searches, which place the bound $M_{\tilde{g}} \gtrsim 1.35$ TeV. When setting limits on simplified models, the gluino is assumed to have a 100% branching ratio into either $qq\chi_1^0$ or $tt\chi_1 0$ final states. For more realistic spectra such as the one considered here, the gluino mass bound will weaken significantly due to branching ratio factors.

3.3 LHC-14 Predictions

In this section, using the spectrum derived and presented above, we discuss the channels we expect to be observable at the LHC. We expect to see three channels, $pp \to \tilde{g}\tilde{g}$, $pp \to \chi_2^0\chi_1^{\pm}$ and $pp \to \chi_1^{\pm}\chi_1^{\mp}$, and only these. The fact that only these three channels would be apparent is a feature of the M-theory construction. The scalars being heavy makes them kinematically inaccessible. The hierarchy between μ and the gaugino masses M_a (and $\mu \gg M_Z$) results in a Bino-like LSP and Wino-like NLSP with heavy Higgsinos, meaning that only two neutralino/chargino direct production channels are accessible at LHC-14.

We computed using the production cross-sections to leading order for the three channels listed above using `MadGraph5` [71] and multiplied them by K factors calculated using `Prospino` [72, 73, 74]. The results, including the expected number of events N given 300 fb^{-1} of data, are tabulated below.

Channel	σ (fb)	N
$pp \to \tilde{g}\tilde{g}$	19	5800
$pp \to \chi_2^0\chi_1^\pm$	19	5800
$pp \to \chi_1^\pm\chi_1^\mp$	10	3000

Given the LSP mass of 450 GeV, a 1.5 TeV gluino is expected to be discoverable at the 5σ level at LHC-14 given 300 fb^{-1} of data [75]. The gluino mass and cross-section allow immediate deduction of the gluino spin [76] and therefore confirmation that the discovery is indeed Supersymmetry. With squarks heavy, that procedure is straightforward. Furthermore, the $\chi_2^0 \to \chi_1^0 h$ decay mode allows for discovery potential in the chargino/neutralino direct production channels. For the benchmark spectrum considered here, direct $\chi_2^0, \chi_1^\pm$ production should be discoverable at LHC-14 with 1000 fb^{-1} of data [77]. We understand that careful background studies need to be done to be sure these processes can be observed. The signatures are distinctive and event numbers large enough so it seems likely signals can be seen, but people more expert than us need to demonstrate the signals are really robust.

3.4 Future Collider Predictions

In this section, we briefly discuss the possible discoveries to be made at future colliders given the spectrum under consideration. We focus in particular on two possible proton-proton colliders, one with $\sqrt{s} = 50\,\mathrm{TeV}$, and the other with $\sqrt{s} = 100\,\mathrm{TeV}$. Prospects for Supersymmetry at such higher energy colliders has been studied recently [75, 78, 79], although not in the context of a top-down, UV complete theory.

Given the spectrum, we find that some crucial new channels are accessible, namely $pp \to t\tilde{t}_1\tilde{g}$, $pp \to b\tilde{b}_1\tilde{g}$, $pp \to \tilde{q}_{1(L,R)}\tilde{g}$, $pp \to \chi_3^0\chi_4^0$, $pp \to \chi_3^0\chi_2^\pm$, $pp \to \chi_4^0\chi_2^\pm$ and $pp \to \chi_2^\pm\chi_2^\mp$. Unfortunately, scalars are too heavy to be pair-produced [78]. However, we note that associated production of first family squarks with gluinos is accessible. The splitting of the light stop and the heavier first family squark masses, plus the kinematic measurement of the first family squarks, combine to give a precise measurement of the gravitino mass, the fundamental quantity that determines all masses in the theory, and thus deeply probes Supersymmetry breaking!

The associated production of stops and sbottoms can come from gluon splitting, or from the top (bottom) quark being considered as a parton. The question of when the top quark parton distribution function (PDF) becomes important has been studied recently [80], and it has been found that using a top PDF has only a small effect at $\sqrt{s} = 100\,\mathrm{TeV}$. Therefore we simulate the production of stop gluino by looking at diagrams where the gluon splits and emits a top quark also. The bottom PDF is better known, and has a more significant effect at the energies in question, but for the purposes of this calculation, we present results using gluon splitting for the associated production of sbottoms. The dominant Feynman diagram for top stop gluino production is shown in fig. 3.4. The diagram for sbottoms is identical with $b, \tilde{b}$ swapped for $t, \tilde{t}$. We recognise that careful studies of bottom and top PDFs need to be done to get fully reliable numbers.

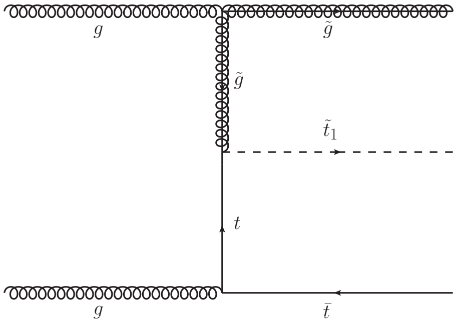

Figure 3.4: Dominant Feynman graph for stop associated production by gluon splitting.

We computed using `MadGraph5` [71] the production cross-sections to leading order for these channels for both $\sqrt{s} = 50\,\mathrm{TeV}$ and 100 TeV. The results are tabulated below, including the number of events N expected given 3000 fb^{-1} of data.

Channel	$\sigma_{50\ \mathrm{TeV}}$ (fb)	$N_{50\ \mathrm{TeV}}$	$\sigma_{100\ \mathrm{TeV}}$ (fb)	$N_{100\ \mathrm{TeV}}$
$pp \to t\tilde{t}_1\tilde{g}$	7.1×10^{-5}	0	1.6×10^{-2}	47
$pp \to b\tilde{b}_1\tilde{g}$	2.6×10^{-6}	0	3.0×10^{-3}	9
$pp \to \tilde{q}_{1(L,R)}\tilde{g}$	3.2×10^{-4}	1	3.0×10^{-1}	900
$pp \to \chi_3^0\chi_4^0$	9.2×10^{-1}	2800	3.4	10200
$pp \to \chi_3^0\chi_2^\pm$	1.8	5400	6.4	19200
$pp \to \chi_4^0\chi_2^\pm$	1.8	5400	6.4	19200
$pp \to \chi_2^\pm\chi_2^\mp$	1.0	3000	3.7	11100

Although the number of stop events is not large, the gluino mass will already be known from LHC, which makes the stop and bottom search significantly simpler. The sbottom production cross-section is expected to be greater given that we make the approximation of gluon splitting rather than using the bottom PDF. We expect 15 or so stop events should already be found given 1000 fb^{-1} of data, as well as 300 first generation squark events. The relatively large number of first family squark associated production events means these should be detectable. We also expect the heavy neutralinos and chargino to be detected, already at a 50 TeV, and certainly at a 100 TeV collider. Note there are other electroweakino production channels e.g. $\chi_2^0\chi_2^\pm$ which have subdominant production cross-sections, two or more orders of magnitude smaller than those presented here. Because of their small production cross-sections, we do not list those channels here.

3.5 Conclusion

In this chapter, we have examined predictions for Supersymmetric particle masses in the G_2-MSSM, motivated by phenomenogically realistic compactifications of M-theory. By combining top-down constraints from moduli stabilization with bottom-up constraints from EWSB and the measured Higgs mass, the sparticle spectrum is completely determined by $M_{3/2}$. Furthermore, given reasonable assumptions regarding the topology of the G_2 manifold, the gravitino mass is approximately calculable, giving a benchmark value $M_{3/2} = 35$ TeV.

The benchmark spectrum corresponding to $M_{3/2} = 35$ TeV is not constrained by LHC-8, and turns out to provide exciting phenomenology for LHC-14 and future colliders. The gluino mass is expected to be about 1.5 TeV for this benchmark spectrum, while the Wino(Bino)-like gaugino mass is about 614(450) GeV. The hierarchy between gaugino masses and $M_{3/2}$ arises because $M_{3/2}$ feels contributions from both the hidden sector meson and moduli F-terms, while gaugino masses only feel contributions from the moduli F-terms which are suppressed by about $\alpha_{GUT} \approx 1/25$ with respect to the meson F-terms. Three and only three production channels should discoverable at LHC-14: $pp \to \tilde{g}\tilde{g}$, $pp \to \chi_2^0\chi_1^\pm$ and $pp \to \chi_1^\pm\chi_1^\pm$ where χ_1^0 and χ_2^0 are respectively Bino and Wino-like. The expected signature of the $\chi_1^\pm\chi_1^\pm$ channel is $\chi^+\chi^- \to W^+W^- +$ MET. The $\chi_2^0\chi_1^\pm$ production channel gives the final state $\chi_2^0\chi_1^\pm \to W^\pm h +$ MET, which should be quite a clear channel at the LHC [77].

We have also investigated the prospects for the discovery of the heavier stops, first family squarks and Higgsinos at future colliders. We find that associated production of gluino stop $pp \to \tilde{g}\tilde{t}_1 t$, gluino sbottom $pp \to \tilde{g}\tilde{b}_1 b$ as well as gluino squark production

$pp \to \tilde{g}\tilde{u}, \tilde{d}$ should be seen at a 100 TeV collider, with leading-order production cross-sections of 1×10^{-2}, 3×10^{-3} and 3×10^{-1} fb respectively. This leads to hundreds of gluino-squark events given 3000 fb^{-1} of data; precise knowledge of the gluino mass can help seperate these events from SM background. The heavy Higgsinos should also be detectable at a 50 TeV collider, and produced in relative abundance at a 100 TeV collider. The relevant Higgsino production channels are $pp \to \chi_3^0\chi_4^0$, $pp \to \chi_3^0\chi_2^\pm$, $pp \to \chi_4^0\chi_2^\pm$ and $pp \to \chi_2^\pm\chi_2^\pm$. The relevant production cross sections at 50 (100) TeV are $\sigma \sim 1.8$ (6.4) fb for $pp \to \chi_{3,4}^0\chi_2^\pm$, and $\sigma \sim 1.0$ (3.5) fb for $pp \to \chi_3^0\chi_4^0$ and $pp \to \chi_2^\pm\chi_2^\pm$. Thus given 3000 fb^{-1} of data, we expect of order a few thousand events for each channel at a 50 TeV collider, and of order tens of thousands of events at a 100 TeV collider.

To summarize, we have shown that the G_2-MSSM provides a constrained top-down framework, in which gluinos and some electroweakinos should be discoverable at LHC-14. The discovery of a single sparticle uniquely determines the remainder of the sparticle spectrum. Thus given a discovery of gauginos at LHC-14, a discovery of squarks and Higgsino at 100 TeV colliders within the predicted mass range would give strong evidence towards Supersymmetry and an UV completion like the compactified M-theory construction presented here.

CHAPTER 4

Future Collider Probes of String Compactifications

In Chapters 2 and 3 we have focused on a particular compactified string model, namely M-theory compactified on a manifold with G_2 holonomy (the G_2-MSSM). A key result in these chapters is that the scalar superpartner masses in the G_2-MSSM are expected to be $\gtrsim 20$ TeV, while the gluino (Wino, Bino) masses are expected to be ~ 1.5 TeV (~ 500 GeV). Such a spectrum with heavy scalars and hierarchally lighter gauginos are generically expected in many compactified string models, see [33] for a review. If nature is described by a compactified string theory with such a spectrum, one generically expects that only gauginos are discoverable at the 14 TeV run of the LHC. However as alluded to in Section 3.4, future hadron colliders operating at much higher center of mass energies can provide a probe of the heavy squarks which are inaccessible at the LHC.

There has recently been considerable interest in the SUSY discovery potential of a future hadron collider operating at a center of mass energy of 100 TeV [75, 81, 79, 78, 9, 82, 83, 84, 85, 86, 87]. These studies of SUSY at future hadron colliders have focused primarily on pair production, either of colored superpartners [75, 81, 78] or of electroweak-inos[1] [79, 82, 83, 84, 85, 86]. In this chapter, we will instead examine the reach of a $\sqrt{s} = 100$ TeV collider for associated production of a heavy squark along with a lighter gaugino. This production channel is particularly noteworthy if the squark masses are $\mathcal{O}(10)$'s of TeV, such that squark pair production is kinematically inaccessible at $\sqrt{s} = 100$ TeV. Spectra where squarks are hierarchically heavier than the gluino/electroweak-inos are predicted in many SUSY breaking models such as anomaly mediation [50, 51] or more general "mini-split"-type scenarios [88, 28, 89] such as the compactified string theories described above. Moreover, multi-TeV squark masses can naturally accommodate the stop masses required to achieve a 125 GeV Higgs boson within the MSSM.

---

[1] Here electroweak-ino refers to any admixture of the Wino, Bino and Higgsino.

The main results of this chapter are summarized in Figures 4.1-4.5, which show the reach of a $\sqrt{s} = 100$ TeV p-p collider with 3 ab^{-1} integrated luminosity for squark-gaugino associated production in various spectra [2]. Squark-gluino production can discover squark masses up to 32 TeV for $\lesssim 4$ TeV gluino masses in spectra with a large gluino-neutralino LSP mass splitting (Fig 4.1). For spectra with a small gluino-neutralino LSP mass splitting, squark masses up to 37 TeV can similarly be discovered (Fig. 4.2). For squark-Wino (Bino) LSP production, Wino (Bino) masses up to $4\,(1.7)$ TeV can be discovered for squark masses $\lesssim 7\,(5)$ TeV (Figs. 4.3-4.4). We find a similar reach for squark-Wino NLSP production (Fig 4.5), even without utilizing objects resulting from NLSP $\rightarrow$ LSP decay. These results indicate that squark-gaugino production represents a SUSY discovery mode at a $\sqrt{s} = 100$ TeV p-p collider in a wide variety of models with heavy first- and second-generation squarks. Currently, the construction of such a future collider is the only known way of directly observing the presence of the heavy squarks predicted by the compactified string theory models discussed in this thesis.

The remainder of this chapter is organized as follows. Section 4.1 discusses our general methodology and simulation strategies. Section 4.2 presents in detail our analysis of squark-gluino associated production, while Section 4.3 presents our analysis of squark-Wino/Bino associated production. Section 4.4 contains a summary of these results. This chapter is based largely on [10] which was done in collaboration with Sebastian Ellis.

4.1 General Methodology

In this section we briefly discuss the general methodology of the analyses presented below. Event topologies arising from heavy squark - light gaugino associated production are characterized by a hard leading jet and significant $\not{E}_T$. These objects result primarily from the squark decay products, as the associated gaugino is produced at relatively low transverse momentum. The dominant SM background for such events is in the $t\bar{t}+$ jets and vector boson + jets channels [75], which fall off rapidly with increasing leading jet p_T, $\not{E}_T$, and $\not{E}_T/\sqrt{H_T}$ (H_T is defined as the scalar sum of the jet transverse energies).

In the following analyses, we consider the reach of a $\sqrt{s} = 100$ TeV proton-proton collider given 3 ab^{-1} integrated luminosity. The minimum production cross section yielding $\gtrsim 10$ events is roughly $\sim 10^{-2}$ fb, corresponding to $m_{\tilde{q}} + m_{\tilde{g}} \sim 35$ TeV ($m_{\tilde{q}} + m_{\tilde{W}} \sim 15$ TeV) for squark-gluino (squark-Wino) associated production. For such masses, good back-

---

[2] Note that a recent study in [90] calls for an integrated luminosity of between 10 and 20 ab^{-1} at a future 100 TeV p-p collider. We present here results for 3 ab^{-1} as a conservative estimate, and so as to be directly comparable with the current literature.

ground discrimination is achieved with hard leading jet p_T cuts for squark-gluino production, and with hard $\not{E}_T/\sqrt{H_T}$ cuts for squark-Wino/Bino production. Our strategy is as follows: for each analysis we impose a set of baseline cuts catered to a set of spectra. We then scan over leading jet p_T and $\not{E}_T$ cuts (squark-gluino) or $\not{E}_T/\sqrt{H_T}$ cuts (squark-Wino/Bino) to maximize significance σ, defined by

$$\sigma \equiv \frac{S}{\sqrt{1+B+\lambda^2 B^2+\gamma^2 S^2}} \ . \tag{4.1}$$

S (B) is the number of signal (background) events passing cuts, and γ (λ) parameterize systematic uncertainties associated with signal (background) normalization. Details of the event generation and collider simulation are given in Appendix B. Like most future collider studies, our simulated σ values are subject to $\mathcal{O}(1)$ uncertainties associated with e.g. the performance of a detector which is yet to be designed. However, this translates to a comparatively mild uncertainty for the predicted reach, due to the rapid falling of production cross sections with increasing mass.

4.1.1 Simplified Models

In the analyses presented below, we consider the following SUSY simplified models:

Model	**Particle Content**	**Fig.**
Squark-Gluino	$\tilde{q}$, $\tilde{g}$, $\chi_1^0 = \tilde{B}$	
Non-compressed	$M_1 = 100$ GeV	Fig. 4.1
Compressed	$m_{\tilde{g}} - m_{\chi_1^0} = 15$ GeV	Fig. 4.2
Squark-Wino LSP	$\tilde{q}$, $\chi_1^0 = \tilde{W}$	Fig. 4.3
Squark-Bino LSP	$\tilde{q}$, $\chi_1^0 = \tilde{B}$	Fig. 4.4
Squark-Wino NLSP	$\tilde{q}$, NLSP = $\tilde{W}$, $\chi_1^0 = \tilde{B}/\tilde{H}$	Fig. 4.5
Split	$M_1/\mu = 100$ GeV	
Non-split	$m_{\tilde{W}} - m_{\chi_1^0} = 200$ GeV	

Table 4.1: Simplified models considered in this chapter.

which encompass a wide array of potential event topologies arising from squark-gaugino production. We take degenerate first and second generation squark masses, and decouple all sparticles not listed in Table 4.1. For the squark-gluino non-compressed model, our results are not sensitive to the choice of $M_1 = 100$ GeV as the LSP is effectively massless for $m_{\chi_1^0} \ll m_{\tilde{g}}$. The squark-gluino compressed model is motivated by the gluino-neutralino coannihilation region [91, 92]. We choose $m_{\tilde{g}} - m_{\chi_1^0} = 15$ GeV as a fiducial value, though the leading jet p_T-based analysis presented below is robust as long as $m_{\tilde{g}} - m_{\chi_1^0} \ll m_{\tilde{g}}$. For the Wino NLSP models, we choose two spectra with differing LSP masses to illustrate the effects of increasing the NLSP-LSP mass splitting. In the "non-split" case, we have chosen an NLSP-LSP mass splitting of 200 GeV so that the NLSP decays to the LSP + on-shell SM bosons.

4.2 Squark-Gluino Associated Production

In this section we discuss squark-gluino associated production. As this process only involves α_s, it can be important at a $\sqrt{s} = 100$ TeV p-p collider even if $m_{\tilde{q}} + m_{\tilde{g}} \gtrsim 35$ TeV. If a heavy squark of order tens of TeV is produced in association with a gluino of mass $\lesssim 10$ TeV, the leading jet from the squark decay will be very hard, $p_T \sim m_{\tilde{q}}/2$. Furthermore the neutralino resulting from the decay chain $\tilde{q} \to q\tilde{g} \to 3\, q\chi^0$ will be very boosted, resulting in large $\not{E}_T$. These kinematic features result in a striking collider signature with very low SM background.

We explore the reach in squark-gluino production at a $\sqrt{s} = 100$ TeV p-p collider for the two types of squark-gluino spectra listed in Table 4.1. For simplicity we assume the LSP is a Bino, and all other neutralinos/charginos are decoupled. Relaxing this assumption allows squark decays to intermediate neutralinos/charginos, resulting in additional final state objects which can be used for background discrimination.

For both non-compressed and compressed spectra, we impose the following baseline cuts:

$$H_T > 10 \text{ TeV}, \quad \not{E}_T/\sqrt{H_T} > 20 \text{ GeV}^{1/2}$$

while for the non-compressed spectra we impose the additional cut:

$$8 \text{ jets with } p_T > 50 \ (150) \text{ GeV}$$

The softer cut is optimized for heavier squarks and lighter gluinos, while the harder cut is optimized for lighter squarks and heavier gluinos. Upon imposing these baseline cuts, we then scan over leading jet p_T and $\not{E}_T$ cuts in order to maximize significance σ as defined in (4.1). We have verified that the optimal cuts render any "background" from gluino pair production subdominant to the SM background.

The results of this analysis are depicted in Figs. 4.1 and 4.2, which show the reach

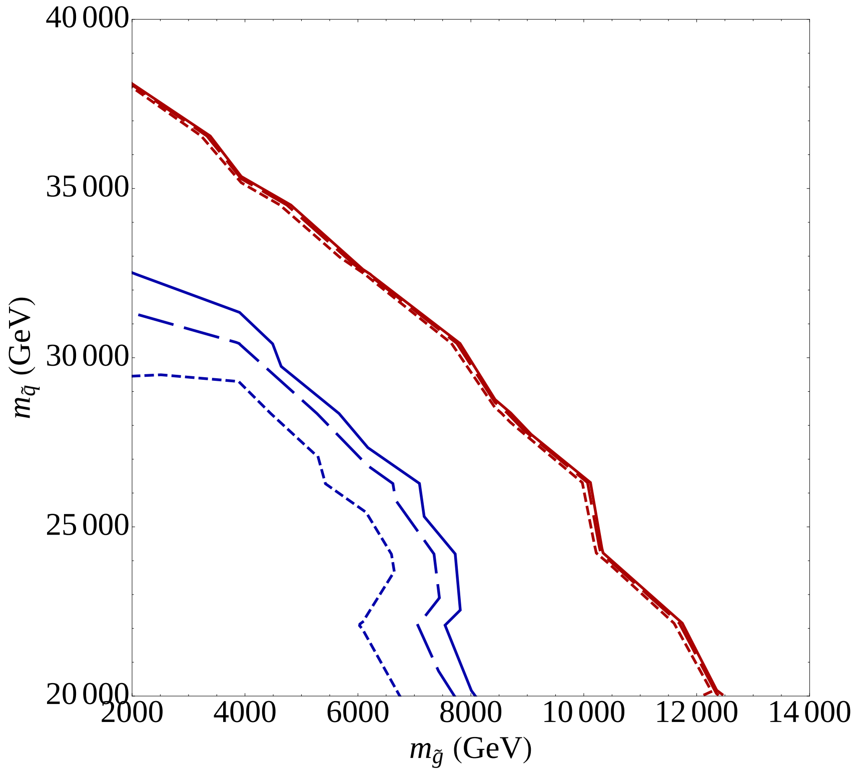

Figure 4.1: Experimental reach for squark-gluino associated production at a 100 TeV proton collider with 3 ab^{-1} integrated luminosity, for spectra with a ~ 100 GeV LSP mass. The solid, long dashed and short dashed lines are for and $5,\ 10,\ 15\%$ systematic uncertainty for the signal respectively. Blue lines indicate 5σ discovery reach and red lines indicate 95% exclusion limits. We assume 20% systematic uncertainty in the background.

of a $\sqrt{s} = 100$ TeV proton collider with 3 ab^{-1} of integrated luminosity. The solid, long dashed and short dashed lines correspond respectively to systematic uncertainties of $5,\ 10$ and 15% for the signal normalization, while the background systematic uncertainty is fixed to 20%. The projected reach is fairly insensitive to background systematic uncertainties, as the number of background events is quite low due to the hard leading jet p_T and $\not{E}_T$ cuts.

As is evident from Figs. 4.1 and 4.2, a $\sqrt{s} = 100$ TeV collider with 3 ab^{-1} integrated luminosity can begin probing much of the "mini-split" parameter space for sufficiently low gluino masses. Final states in the compressed spectra yield more $\not{E}_T$ compared to the non-compressed spectra, resulting in the greater reach depicted in Figure 4.2. Notably, with 3 ab^{-1} integrated luminosity the entire neutralino-gluino coannihilation region (whose upper endpoint lies at $m_{\tilde{g}} \approx m_{\tilde{\chi}} \approx 8$ TeV [92]) can be excluded if the squark masses are $\lesssim 28$ TeV.

It is worthwhile to compare Figs. 4.1 and 4.2 to projected reaches for gluino pair

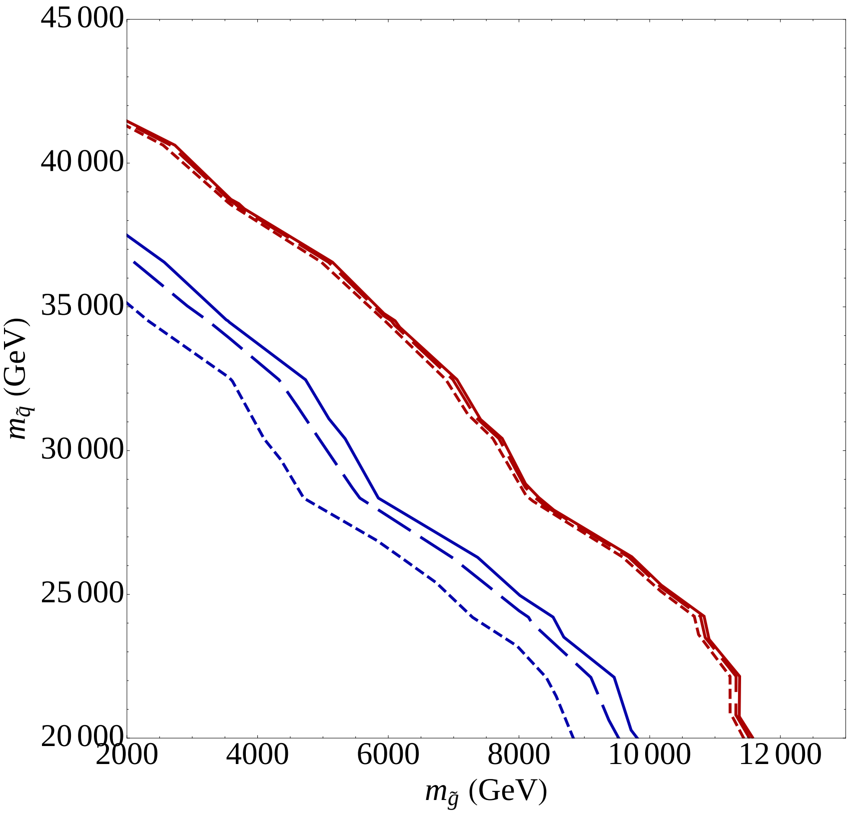

Figure 4.2: Experimental reach for squark-gluino associated production at a 100 TeV proton collider with 3 ab^{-1} integrated luminosity for spectra with $m_{\tilde{g}} - m_{\chi_1^0} = 15$ GeV. The different lines follow the conventions of Fig. 4.1. We assume 20% systematic uncertainty in the background.

production. Our results for non-compressed spectra have some overlap with [75][3], which considered both pair production and associated production in similar spectra with squark masses $\lesssim 24$ TeV. The results of [75] indicate that gluino pair production will likely be the discovery channel for colored superpartners for the spectra in Fig. 4.1 provided $m_{\tilde{g}} \lesssim 14$ TeV. On the other hand, if the gluino and the LSP are nearly degenerate, searches for gluino pair production rapidly lose sensitivity [75]. Thus if the gluino and the LSP are nearly degenerate as in the gluino-neutralino coannihilation scenario, squark-gluino associated production would be a potential discovery channel for colored superpartners.

---

[3] A search optimizing over H_T cuts as opposed to leading jet p_T cuts was done in [75]. For the spectra in Fig. 4.1, the H_T cut based analysis has a 3-5 TeV weaker reach in $m_{\tilde{q}} + m_{\tilde{g}}$ with respect to squark-gluino associated production.

4.3 Squark-Wino and Squark-Bino Associated Production

In this section we discuss squark-Wino and squark-Bino associated production. These channels are particularly important if squark-gluino associated production is inaccessible due to a sufficiently heavy gluino mass[4]. The event topology is qualitatively similar to squark-gluino production, as the squark will decay to a boosted jet and boosted Wino/Bino while the associated Wino/Bino is produced at relatively low p_T. However as noted in Section 4.1, associated squark-Wino/Bino production probes significantly lighter squark masses than squark-gluino production. Consequently, multi-TeV leading jet p_T and $\not{E}_T$ cuts are not as effective for background discrimination in squark-Wino/Bino production. Instead, we find that hard $\not{E}_T/\sqrt{H_T}$ cuts are quite effective at reducing the $t\bar{t}+$ jets and vector boson + jets background without rejecting too many signal events.

In order to determine the projected reach for squark-Wino/Bino production at a $\sqrt{s} = 100$ TeV pp collider with 3 ab^{-1} integrated luminosity, we impose the following baseline cuts:

$$p_T(j_1) > 2 \text{ TeV}, \quad \not{E}_T > 3 \text{ TeV}, \;\; \Delta\phi(j, \not{E}_T) > 0.5$$

where the $\Delta\phi$ cut is imposed only on the two leading jets. We then scan over $\not{E}_T/\sqrt{H_T}$ cuts for each spectrum to maximize σ as defined in (4.1).

Our focus is on spectra listed in Table 4.1 where at most one of the gaugino/Higgsino mass parameters M_1, M_2, μ are $\lesssim 1$ TeV, such that the gauge eigenstates are approximately aligned with the mass eigenstates in the neutralino/chargino sectors. We omit the "compressed" region $m_{\tilde{q}} - m_{\tilde{\chi}} < 1$ TeV, as in this region the event topology of associated squark-Wino/Bino production is similar to squark pair production, only with a substantially smaller cross section. Assuming a systematic uncertainty of 10% for the signal normalization, the results of the above analysis for the various spectra in Table 4.1 are depicted in Figures 4.3-4.5.

Figure 4.3 shows the reach for squark-Wino production with a pure Wino LSP; the solid, short-dashed, long-dashed lines correspond to background uncertainties of 1%, 2% and 3 %. In Figure 4.4 we show the reach for squark-Bino production with a pure Bino LSP. The solid, short-dashed, long-dashed lines correspond to background systematic uncertainties of 0.5%, 1% and 1.5%. Compared to squark-Wino production, the reach for squark-Bino associated production is quite sensitive to background uncertainties. This is because the 5σ contours for squark-Bino production correspond to significantly lower masses due to the smaller production cross-section, resulting in lower optimal $\not{E}_T/\sqrt{H_T}$ cuts and thus larger

---

[4] In the MSSM, a gluino which is hierarchically heavier than the squarks requires fine-tuning of the soft masses. This can be avoided however in a model with Dirac gluinos [93, 94].

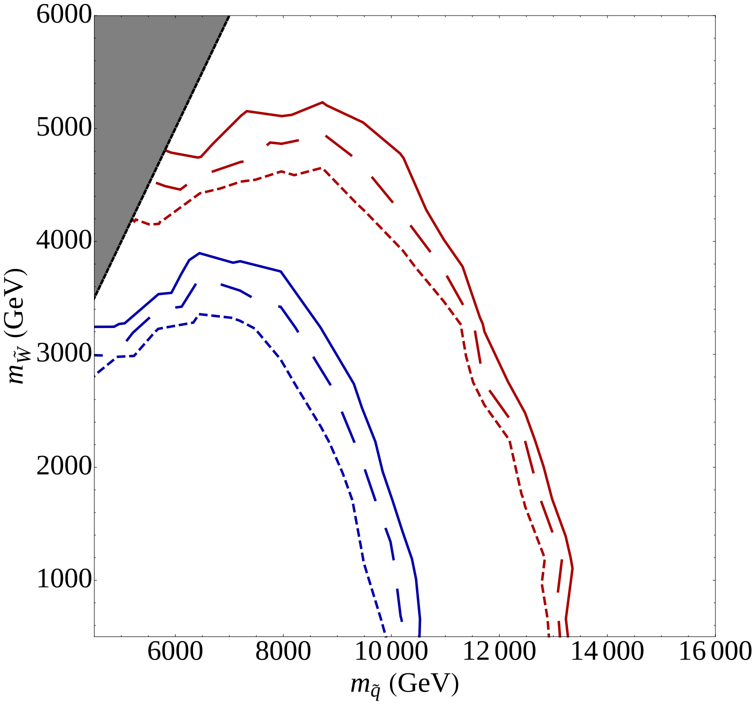

Figure 4.3: Experimental reach for squark-Wino LSP associated production at a 100 TeV proton collider with 3 ab^{-1} integrated luminosity. The solid, long dashed and short dashed lines are for $1, 2, 3\%$ systematic uncertainty for the background respectively. Blue lines indicate 5σ discovery reach and red lines indicate 95% exclusion limits. We do not consider the grey shaded region ($m_{\tilde{q}} - m_{\tilde{W}} < 1$ TeV) for reasons given in the text. We assume 10% systematic uncertainty for the signal.

backgrounds.

In Figure 4.5 we show the reach of the $\not{E}_T/\sqrt{H_T}$ based monojet analysis for squark-Wino production with a Wino NLSP, with background uncertainties fixed to be 1%. The green lines correspond to $M_{NLSP} - M_{LSP} = 200$ GeV, while the red lines correspond to $M_{LSP} = 100$ GeV. For comparison, the blue lines show the reach for squark-Wino production when the Wino is the LSP. Away from the $m_{\tilde{q}} \sim m_{\tilde{W}}$ region the sensitivity is lower for a Wino NLSP, as $\not{E}_T$ is being traded for W, Z and higgs bosons arising from the NLSP $\rightarrow$ LSP decay. Note that the analysis considered here does not exploit the additional SM bosons present in the Wino NLSP scenario. Thus the reach for the Wino NLSP scenario depicted in Figure 4.5 applies regardless of whether the LSP is Bino-like or Higgsino-like. Exploiting the additional SM bosons could extend the reach for the Wino NLSP scenario, so the result presented here is a conservative estimate.

We close this section by comparing the results of Figures 4.3-4.5 to studies of pair production at $\sqrt{s} = 100$ TeV. Given 3 ab^{-1} integrated luminosity, squark pair production can discover squark masses up to 2.5 TeV [75] (assuming a conservative 20 $\%$ background

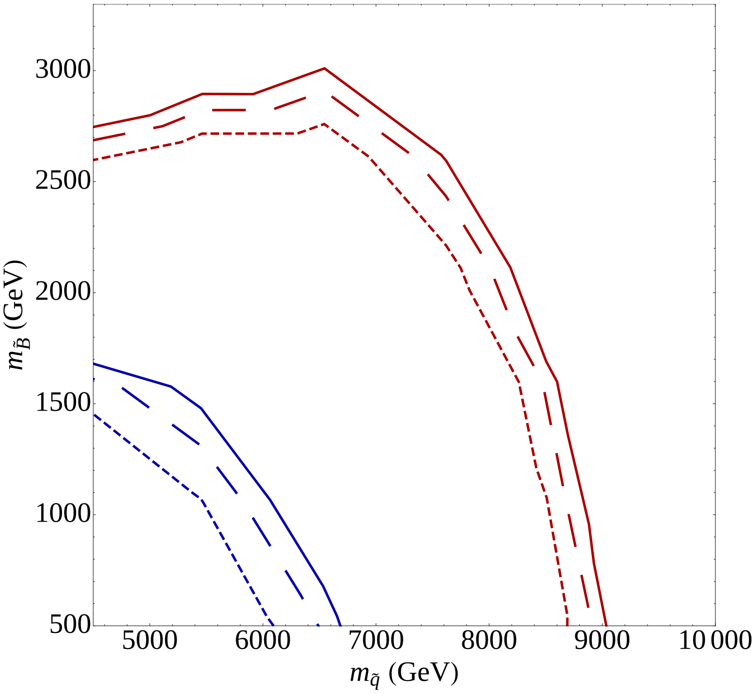

Figure 4.4: Experimental reach for squark-Bino LSP associated production at a 100 TeV proton collider with 3 ab^{-1} integrated luminosity. The solid, long dashed and short dashed lines are for and $0.5,\ 1,\ 1.5\%$ systematic uncertainty for the background respectively. Blue lines indicate 5σ discovery reach and red lines indicate 95% exclusion limits. We do not consider the region $(m_{\tilde{q}} - m_{\tilde{B}} < 1$ TeV) for reasons given in the text. We assume 10% systematic uncertainty in the signal.

systematic uncertainty). In the pure Wino case, searches in VBF channels can discover Winos up to 1.1 TeV [86]. Disappearing tracks can also provide a collider probe of pure Wino LSP pair production. Extrapolating the disappearing tracks background from the 8 TeV ATLAS study [95], the projected reach is 2-3 TeV for pure Winos [79]. However, the data-driven disappearing-track background at 100 TeV is difficult to estimate, making this projected reach less reliable than the reach in the VBF channel or the reach depicted in Figure 4.3. Finally, pair production of Wino NLSPs has been considered in [82, 83]. Assuming no systematic uncertainties, for a Higgsino LSP the projected discovery reach is 2.3 TeV, while for a Bino LSP the reach is 1-3 TeV depending on the NLSP $\rightarrow Z$ LSP branching ratio. Comparing these reaches to Figures 4.3-4.5, we see that squark-Wino/Bino associated production can provide a SUSY discovery mode provided the squark is not too much heavier than the Wino/Bino.

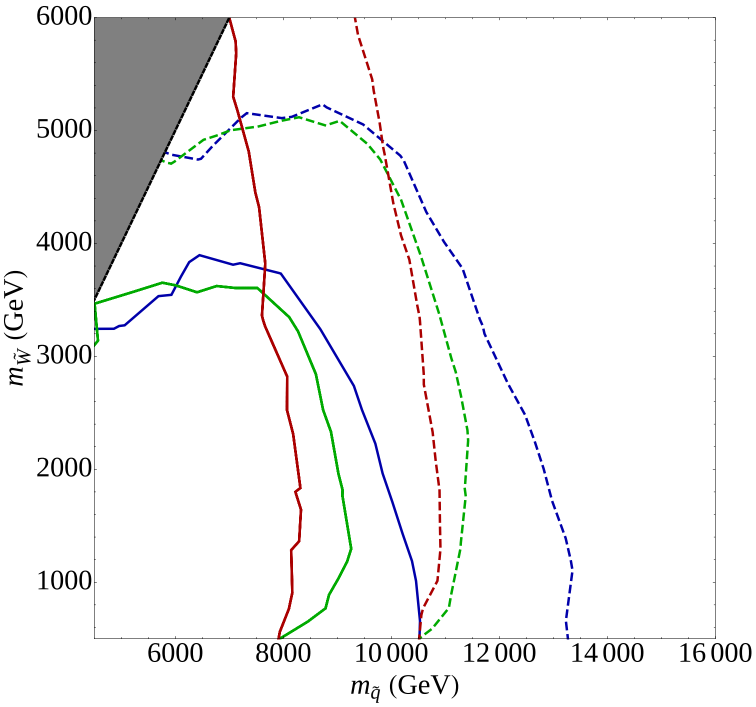

Figure 4.5: Experimental reach for squark-Wino associated production at a 100 TeV proton collider with 3 ab^{-1} integrated luminosity. Solid lines indicate 5σ discovery reach, and dotted lines indicate 95% exclusion limits. Blue curves correspond to a Wino LSP, while the green (red) curves correspond to a Wino NLSP with $M_{\text{NLSP}} - M_{\text{LSP}} = 200$ GeV ($M_{LSP} \sim 100$ GeV). The results are applicable for both Bino- and Higgsino-like LSP. We do not consider the grey shaded region ($m_{\tilde{q}} - m_{\tilde{W}} < 1$ TeV) for reasons given in the text. We assume 1% systematic uncertainty in the background and 10% in the signal.

4.4 Summary

We have examined in this chapter the kinematic reach for squark-gaugino associated production at a 100 TeV proton proton collider. In models where squark pair production is kinematically inaccessible at a 100 TeV collider, squark-gaugino associated production may be the only possible channel for observing heavy squarks. This is of considerable importance for compactified string models discussed in this thesis, which predict heavy $\gtrsim 20$ TeV squark masses that are well out of reach of the LHC.

We have considered the various simplified models listed in Table 4.1. For squark-gluino production with $\mathcal{O}$(TeV) gluinos, the discovery reach for first-generation squarks can be up to 37 TeV for compressed spectra (small gluino-LSP mass splitting), and up to 32 TeV for non-compressed spectra, subject to systematic uncertainties. For squark-Wino LSP production, we have shown that the discovery reach for the Wino is almost 4 TeV for squarks of ~ 7 TeV, subject to systematic uncertainties. For squark-Wino NLSP production we have analysed two scenarios: one where the NLSP-LSP mass difference is 200 GeV, and one where the LSP mass is ~ 100 GeV. In the first scenario, the Wino discovery reach is about 3.5 TeV for squarks of $\sim$ 7 TeV. In the second scenario, the Wino reach extends up to 6 TeV. Our results in the Wino-NLSP scenario are insensitive to the nature of the LSP. For $\lesssim 9$ TeV squark masses, squark-Wino associated production marks a significant increase in the Wino reach compared to pair production channels. We also consider squark-Bino associated production, and find that the kinematic reach for the Bino is up to 1.7 TeV for squarks of mass ~ 5 TeV, subject to systematic uncertainties.

The results presented here raise the exciting prospect of directly probing a region of parameter space that so far has been the exclusive domain of indirect searches through low-energy FCNC observables. The squark-gaugino associated production channels studied here, coupled with studies of Supersymmetry at 100 TeV colliders already undertaken [75, 81, 79, 78, 9, 82, 83, 84, 85, 86, 87], provide a strong physics case for the construction of such a collider.

CHAPTER 5

Dark Sector Dark Matter in String Compactifications

In Chapters 3 and 4, we focused primarily on collider physics as an experimental probe of compactified string theories. This chapter instead focuses on dark matter and its implications for string-motivated models. Like Chapter 4, this chapter attempts to be as general as possible regarding compactified string theories, and does not focus on any particular model.

Apart from its existence (see e.g. [96]), the nature and non-gravitational interactions of dark matter (DM) are still very uncertain. The most popular class of dark matter models - Weakly Interacting Massive Particles (WIMPs) - rely on two key assumptions to reproduce the observed relic abundance (see e.g. [97]). First, WIMPs are assumed to annihilate into Standard Model (SM) particles with an electroweak-scale cross section. Second, the universe is usually assumed to be radiation dominated between the end of inflation and matter-radiation equality. However, there are no clear indications that either of these assumptions are valid. With regards to the former, large regions of WIMP parameter space have been ruled out by various direct and indirect detection experiments. With regards to the latter, the earliest evidence for a radiation dominated universe arises during Big Bang Nucleosynthesis (BBN), which occurs at temperatures of order an MeV. The energy budget of the Universe has not been probed for temperatures above that at the time of BBN. Of course, it is still possible that dark matter is a simple WIMP, but because of the above reasons it is well-motivated to go *beyond* the traditional WIMP paradigm, both in terms of DM candidates as well as the production mechanisms for DM.

A well-motivated alternative to the standard "thermal" cosmological history mentioned above is that of a non-thermal cosmological history, in which BBN is preceeded by a phase of pressureless matter domination. A non-thermal cosmological history is naturally predicted by compactified string theories, as the moduli discussed in Chapters 1 and 2 significantly influence early universe cosmology. When the Hubble parameter drops below moduli masses, moduli begin coherent oscillations and behave as pressure-less matter, dominating the energy density of the universe until the longest-lived one (ϕ) decays to reheat the universe. In these cosmological histories, an electroweak-scale Wino provides a natural candidate for SUSY dark matter, provided that the modulus dominated phase ends at temperatures below a GeV or so [69, 98]. However, recent FERMI-LAT and HESS observations of Galactic Center photons have placed severe limits on Wino DM [59, 60]. If the Wino is stable, satisfying these constraints in the cosmological histories mentioned above requires a large hierarchy between the modulus and gravitino masses [59]. This hierarchy is quite unnatural for a broad class of models in which moduli stabilization sets the scale of Supersymmetry breaking [33, 65, 99, 100], such as the G_2-MSSM model discussed in previous chapters. This conclusion also holds if the lightest superpartner is some more general admixture of MSSM particles [101]. A simple way to avoid these constraints is to assume that the lightest visible sector superpartner, hereafter referred to as the LOSP, is unstable.

Motivated by the above statements, this chapter provides a comprehensive study of relic DM production in cosmological histories with a late phase of modulus domination. To perform as general an analysis as possible, we go beyond the standard WIMP picture by *i*). allowing for a wide range of DM masses and annihilation cross sections and *ii*). allowing for the possibility that DM is in kinetic equilibrium with some sector other than the visible sector. These two assumptions are well motivated in SUSY theories with an unstable LOSP, but can also be true in general. If the LOSP decays, DM is not a visible sector particle; a priori there is no reason to expect its DM mass or annihilation cross section to be near the electroweak scale. Moreover, if the DM resides in a sector that couples weakly to the visible sector, DM could be in kinetic equilibrium with a "dark sector" instead of the thermal bath of visible sector particles.

The primary goal of this chapter is to classify production mechanisms for dark matter particles that resides in a "dark sector". This dark sector need not be in thermal equilibrium with the visible sector, and must therefore be tracked seperately in the Boltzmann equations[1]. We will solve the relevant system of Boltzmann equations, and classify all potential mechanisms for the production of relic DM into four different parametric regimes. This will allow us to map out the viable regions of parameter space in the context of compactified string theories. Much of this parameter space is excluded due to overproduction of dark matter, illustrating the importance of dark matter constraints as a bottom-up input for studying the string landscape. We then briefly discuss potential experimental signatures of these DM models. Notably, there are a class of DM models in which the DM power

---

[1] We refer here to the Boltzmann equations which govern particle number density in an expanding universe, see e.g. [97].

spectrum is sensitive to the linear growth of subhorizon DM density perturbations during the modulus dominated era. This can lead to interesting astrophysical signatures, such as an abundance of earth-mass (or smaller) DM microhalos which are far denser than their counterparts in standard cosmologies [102].

This chapter is organized as follows. Section 5.1 provides an overview of the two-sector cosmology analyzed here. Section 5.2 provides a classification of the DM production mechanisms in this framework, and provides semi-analytic expressions for $\Omega_{DM}h^2$. Section 5.3 maps out viable regions of parameter space for UV-motivated SUSY theories such as the compactified string theories discussed in preceeding chapters. Section 5.4 describes the experimental consequences of these models. Section 5.5 presents a summary of this chapter. Note that this chapter is largely based on work done with collaborators in [11].

5.1 Overview of Two-Sectors - Models and Cosmology

The framework considered here consists of two sectors: a visible sector containing SM (and perhaps MSSM) particles and a dark sector containing the DM. Both the visible and dark sectors are assumed to have sufficient interactions such that thermal equilibrium is separately maintained within the two sectors, whose temperatures are T and T' respectively. We assume that there exist very weak portal interactions between the two sectors, so that T and T' may not be equal to each other. Finally, we assume that the Universe is dominated by the coherent oscillations of a modulus field ϕ at some time which is much earlier than when BBN occurs[2]. The cosmological framework described above is depicted schematically in Figure 5.1. The results of our work will be straightforward to reduce to the single sector case, see the discussion in Section 5.2.5.

As denoted in Figure 5.1, the visible sector contains radiation degrees of freedom R, comprised of relativistic particles in equilibrium with the SM bath at temperature T. We also track the abundance of an unstable WIMP-like particle X which is in equilibrium with the visible sector. X corresponds to the LOSP in the SUSY theories discussed in the introduction. The dark sector is assumed to contain a stable DM candidate X', along with dark radiation R'. "Dark radiation" refers to dark sector particles which are in thermal equilibrium and are relativistic at a given dark sector temperature T'. Henceforth, visible (dark) sector quantities are denoted using unprimed (primed) variables. For simplicity and

---

[2] In general, there could be many moduli present in the early Universe. In this case, ϕ should be thought of as the longest-lived modulus. DM produced from shorter-lived moduli will be diluted by entropy production [56].

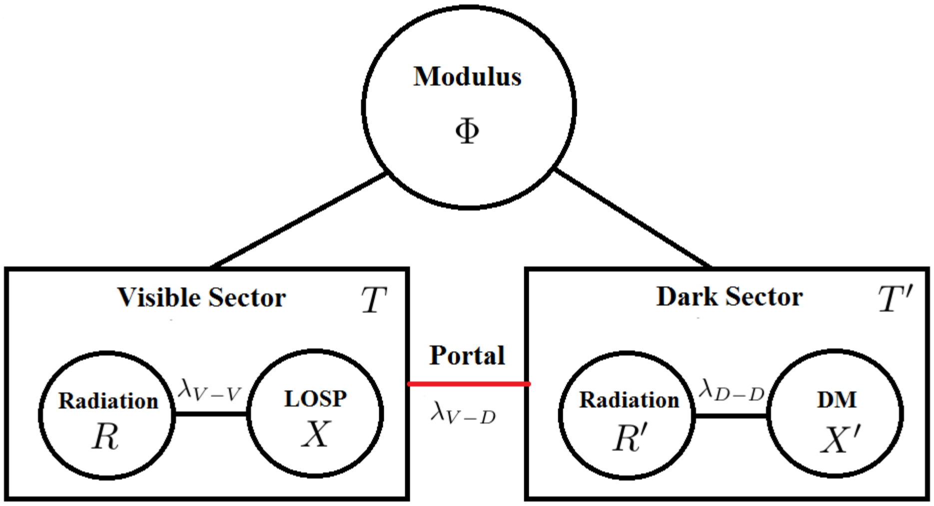

Figure 5.1: Schematic representation of the Two-sector Framework under consideration.

concreteness, we assume that no DM asymmetry is present, so DM particles and antiparticles need not be separately tracked in the Boltzmann equations. Relaxing this assumption is worth exploring in future studies, see for example [101]. Finally we make the assumption that M_X, $M_{X'} \ll m_\phi$, which is naturally expected for the Supersymmetric theories discussed in the introduction and in Section 5.3.

Before moving on to study the cosmological evolution of this system, it is worth mentioning that there are constraints on hidden sector relativistic degrees of freedom during BBN and during recombination, through their contribution to the expansion rate of the Universe. These constraints are typically presented in terms of the number of effective extra neutrino species $\Delta N_{\rm eff}$, which is related to the number of relativistic hidden sector degrees of freedom $g'_*(T')$ by:

$$\Delta\, N_{\rm eff}(T_{BBN}) = 0.57\; g'_\star(T'_{BBN})\, \xi^4(T_{BBN}), \quad \Delta\, N_{\rm eff}(T_{CMB}) = 2.2\; g'_\star(T'_{CMB})\, \xi^4(T_{CMB}) \tag{5.1}$$

where $T_{BBN} \sim 1$ MeV, $T_{CMB} \sim 1$ eV and $\xi(T) \equiv (T'/T)^4$. The current 95% CL bounds are $\Delta\, N_{\rm eff}(T_{BBN}) \leq 1.44$ [103] and $\Delta N_{\rm eff}(T_{CMB}) \leq 0.4$ [104]. We will discuss the implications of these constraints for the two sector models considered here in Section 5.2.1.2.

5.1.1 Cosmological Evolution

The cosmology of the framework can be studied by writing down the Boltzmann equations for the time evolution of the relevant quantities which comprise the total energy density of the Universe. This includes the modulus energy density ρ_ϕ, the energy density arising from X and X' with number densities n_X and $n_{X'}$ respectively, and the energy densities of radiation in the visible and dark sector, denoted by ρ_R and $\rho_{R'}$ respectively. The relevant parameters in the Boltzmann equations turn out to be:

$$\{T_{RH}, \Gamma_X, M_X, M_{X'}, \langle\sigma\, v\rangle, \langle\sigma\, v\rangle', B_X, B_{X'}, \eta, g_*(T), g'_*(T')\}. \tag{5.2}$$

Here Γ_X is the decay width of the unstable X particle, M_X and $M_{X'}$ denote the masses of X and X' respectively, while $\langle\sigma\, v\rangle$ and $\langle\sigma\, v\rangle'$ denote the thermally averaged annihilation cross-section of X and X' respectively. $g_*(T)$ and $g'_*(T')$ are the relativistic degrees of freedom in the visible and dark sectors at a given temperature T, T'. The quantities B_X and $B_{X'}$ denote the branching fractions of the modulus to X and X' respectively[3]. Given the assumption $M_X,\, M_{X'} \ll m_\phi$, η approximately denotes the fraction of the energy density from the modulus going to dark radiation, with the remaining fraction $(1-\eta)$ going to visible radiation. Finally, following established convention we define T_{RH} in terms of the decay width of the modulus Γ_ϕ as follows:

$$T_{RH} \equiv \sqrt{\Gamma_\phi M_{\rm pl}} \left(\frac{45}{4\pi^3 g_*(T_{RH})}\right)^{1/4}, \tag{5.3}$$

where $M_{\rm pl} = 1.22\times10^{19}$ GeV is the Planck scale, and $g_\star(T_{RH})$ is the number of relativistic degrees of freedom in the visible sector at T_{RH}. We will discuss the physical intepretation of T_{RH} in Section 5.2.1.2.

A priori, the nine parameters in (5.2) can vary over a wide range of values, and could affect the computation of the DM relic abundance in a variety of ways. However, we will show that for $\Gamma_X > \mathcal{O}(1)\Gamma_\phi$, the DM production mechanisms only depend on a subset of the parameters in (5.2), in particular:

$$\{T_{RH},\, B_{tot},\, m_\phi,\, \eta, M_{X'},\, \langle\sigma v\rangle',\, g_\star(T),\, g'_\star(T')\}, \tag{5.4}$$

where $B_{tot} \equiv B_X + B_{X'}$ if X decays to X' and $B_{tot} \equiv B_{X'}$ if X does not decay to X'. Note that there is no dependence on parameters measuring the attributes of the LOSP X– $\{\Gamma_X, M_X, \langle\sigma v\rangle\}$! Furthermore, as will be discussed in Section 5.3, the parameters T_{RH} and m_ϕ are completely determined by the masses and couplings of the modulus ϕ. Thus these parameters are insensitive to the details of the dark sector. In the forthcoming analysis, we

---

[3] Note that B_X also includes channels in which ϕ decays to X through intermediate states; $B_{X'}$ is similarly defined.

find it useful to choose benchmark values for the following parameters:

$$\begin{aligned} \text{Benchmark :} \qquad & T_{RH} = 10\,\text{MeV},\ B_{tot} = 0.1,\ m_\phi = 50\,\text{TeV},\ \eta = 0.1, \\ & \qquad\qquad g_\star(T) = 10.75,\ g'_\star(T') = 10.75 \end{aligned} \tag{5.5}$$

The theoretical motivation for these benchmark values will be clear from the discussion in Section 5.3. With these parameters fixed, the DM abundance will depend only on $M_{X'}$ and $\langle\sigma v\rangle'$, and we will see that these can take a wide range of values for viable DM production mechanisms. As mentioned above, for most of the analysis we take $\Gamma_X > \Gamma_\phi$ since this is naturally obtained if Γ_X is not Planck suppressed. In Appendix D, however, we will briefly discuss the case $\Gamma_X \lesssim \Gamma_\phi$.

The Boltzmann equations which describe this system are a natural generalization of those which are applicable to a single sector framework within a modulus dominated Universe, as studied in [105, 106]. As pointed out in these papers, it is more convenient to define dimensionless variables corresponding to the energy and number densities and also to convert derivatives with respect to time to those with respect to the (dimensionless) scale factor $A \equiv \frac{a}{a_I}$, with $a_I \equiv T_{RH}^{-1}$. Thus, following [105, 106] we define:

$$\begin{aligned} \Phi \equiv \frac{\rho_\phi A^3}{T_{RH}^4},\ R \ &\equiv\ \rho_R \frac{A^4}{T_{RH}^4},\ X \equiv n_X \frac{A^3}{T_{RH}^3},\ R' \equiv \rho_{R'} \frac{A^4}{T_{RH}^4},\ X' \equiv n_{X'} \frac{A^3}{T_{RH}^3}, \\ \widetilde{H} \ &\equiv\ \left(\Phi + \frac{R+R'}{A} + \frac{E_{X'}X' + E_X X}{T_{RH}}\right)^{1/2}. \end{aligned} \tag{5.6}$$

$E_X \approx (M_X^2 + 3\,T^2)^{1/2}$ and $E_{X'} \approx (M_{X'}^2 + 3\,T'^2)^{1/2}$ are the thermally averaged X, X' energies assuming that X and X' are in kinetic equilibrium. The Boltzmann equations in terms of these comoving dimensionless variables are:

$$\begin{aligned} \widetilde{H}\frac{d\Phi}{dA} \ &= \ -\,c_\rho^{1/2}\, A^{1/2}\Phi \\ \widetilde{H}\frac{dR}{dA} \ &= \ c_\rho^{1/2} A^{3/2}\left(1-\bar{B}\right)(1-\eta)\Phi + c_1^{1/2}\, M_{\rm pl}\left[\frac{2E_X\left\langle\sigma v\right\rangle}{A^{3/2}}\left(X^2 - {X_{\rm eq}}^2\right) + A^{3/2}\Lambda\left\langle\Gamma_X^R\right\rangle X\right] \\ \widetilde{H}\frac{dX}{dA} \ &= \ \frac{c_\rho^{1/2} T_{RH} B_X}{m_\phi} A^{1/2}\Phi + c_1^{1/2}\frac{M_{\rm pl}T_{RH}}{A^{5/2}}\left\langle\sigma v\right\rangle\left({X_{\rm eq}}^2 - X^2\right) - \frac{c_1^{1/2}M_{\rm pl}}{{T_{RH}}^2}A^{1/2}X\left\langle\Gamma_X\right\rangle \\ \widetilde{H}\frac{dX'}{dA} \ &= \ \frac{c_\rho^{1/2} T_{RH} B_{X'}}{m_\phi} A^{1/2}\Phi + c_1^{1/2}\, M_{\rm pl}T_{RH}A^{-5/2}\ \left\langle\sigma v\right\rangle'\left({X'_{\rm eq}}^2 - X'^2\right) + \frac{c_1^{1/2}M_{\rm pl}}{{T_{RH}}^2}A^{1/2}X\left\langle\Gamma_X\right\rangle \\ \widetilde{H}\frac{dR'}{dA} \ &= \ c_\rho^{1/2}\, A^{3/2}\left(1-\bar{B}\right)\eta\,\Phi + c_1^{1/2}\, M_{\rm pl}\left[\frac{2E_{X'}\left\langle\sigma v\right\rangle'}{A^{3/2}}\left(X'^2 - {X'_{\rm eq}}^2\right) + A^{3/2}\Lambda\left\langle\Gamma_X^{R'}\right\rangle X\right] \end{aligned} \tag{5.7}$$

with $c_\rho = \left(\frac{\pi^2 g^*(T_{RH})}{30}\right)$, $c_1 = (\frac{3}{8\pi})$, $\Lambda = (E_X - E_{X'})/T_{RH}^3$ and

$$\bar{B} \equiv \frac{B_X E_X + B_{X'} E_{X'}}{m_\phi}\,. \tag{5.8}$$

X_{eq} and X'_{eq} are related to the X and X' equilibrium number densities via:

$$X_{eq} \equiv \left(\frac{A}{T_{RH}}\right)^3 \frac{gT{M_X}^2}{2\pi^2} K_2\left(\frac{M_X}{T}\right) \quad \text{if} \quad M_X \gg T, \quad \left(\frac{A}{T_{RH}}\right)^3 \frac{c_\xi\,\zeta(3) T^3}{\pi^2} \quad \text{if} \quad M_X \ll T, \tag{5.9}$$

where g counts the degrees of freedom of X and $c_\xi = g\;(3g/4)$ for bosonic (fermionic) X. X'_{eq} is given by (5.9) with primed variables replacing unprimed variables.

Note that we have assumed in (5.7) that X decays to X'; we neglect $X' + ... \to X$ inverse decays, as the dynamics which fix $\Omega_{X'}$ occur when $T' \lesssim M_X$ (see Section 5.2.2) at which point inverse decays are exponentially suppressed. The thermally averaged X decay rate is given by:

$$\langle \Gamma_X \rangle = \Gamma_X \frac{K_1(M_X/T)}{g_X K_2(M_X/T)}, \qquad \langle \Gamma_X \rangle \xrightarrow{M_X \gg T} \frac{\Gamma_X}{g_X}. \tag{5.10}$$

where Γ_X is the X decay rate in the X rest frame, and K_1 and K_2 are modified Bessel functions of the second kind. The quantities $\langle \Gamma_X^R \rangle$ and $\langle \Gamma_X^{R'} \rangle$ are respectively the thermally averaged partial widths for $X \to X'R$ and $X \to X'R'$. In the remainder of this work, we focus on the case where all X decay channels yield X' such that (5.7) is valid; this corresponds to X and X' both being charged under the DM stabilization symmetry. It is also possible for X to instead decay directly to visible radiation, as is the case for R-parity violating SUSY models. In this case X and X' are essentially decoupled in the Boltzmann equations, which significantly simplifies the analysis. In Section 5.2 we focus on the more complicated case where X decays to X', and discuss how relaxing this assumption affects our results.

The above differential equations are solved subject to the following initial conditions:

$$A = 1,\ \Phi = \Phi_I = \frac{3H_I^2\, M_{\rm pl}^2}{8\pi\, T_{RH}^4},\ R = 0,\ R' = 0,\ X = 0,\ X' = 0 \tag{5.11}$$

These initial conditions are somewhat unphysical as they imply $\rho_R = \rho_{R'} = 0$ at $A = 1$. However, at early times the visible and dark radiation energy densities are subdominant, so this approximation is justified. H_I is the initial value of the Hubble parameter which fixes the initial energy density of the modulus field, parameterized by Φ_I. As we will see, in most cases the DM relic abundance is largely insensitive to the initial condition Φ_I.

5.2 Solution of the Boltzmann Equations and the Dark Matter Abundance

Given the system of equations (5.7), it is possible to numerically solve it for various choices of the parameters in (5.2). However, in order to get a good physical intuition of the qualitatively different mechanisms at play, it is advisable to study various approximate (semi) analytic solutions which are applicable in different regions of the parameter space. We carry out such an exercise in this section. In Appendix E, we compare our approximations to the full numerical analysis and find very good agreement.

5.2.1 Useful Approximations

We now derive useful approximations which allow us to obtain semi-analytic expressions for $\Omega_{DM}h^2$ in Section 5.2.2. To start with, it is worth noting that Φ remains constant until $H \sim \Gamma_\phi$ to a very good approximation. Thus in the following analysis we set $\widetilde{H} = {\Phi_I}^{1/2}$ throughout the period of modulus domination, considerably simplifying the Boltzmann equations. Our strategy will be to use physically well-motivated approximations to first solve for Φ, R, R' and X, and then use these solutions to study the equation for X'.

5.2.1.1 Approximate solutions for Φ, R and R'

Consider first the Boltzmann equation for Φ. With $\widetilde{H} = \Phi_I^{1/2}$, it is straightforward to solve for Φ:

$$\Phi \approx \Phi_I \exp\left[-\frac{2}{3}\left(\frac{c_\rho}{\Phi_I}\right)^{1/2}(A^{3/2}-1)\right]. \tag{5.12}$$

Thus, as expected, Φ remains approximately constant at Φ_I, and only begins to decay vigorously when the dimensionless scale factor satisfies $A > A_\star$, with

$$A_\star \equiv \left(\frac{3}{2}\left(\frac{\Phi_I}{c_\rho}\right)^{1/2}+1\right)^{2/3}. \tag{5.13}$$

Now consider the equations for R and R'. As can be seen from (5.7), in addition to the modulus decay term these equations contain the X and X' annihilation terms as well as the X decay term. *However, it turns out that for $M_X, M_{X'} \ll m_\phi$ all these terms are quite sub-dominant compared to the modulus decay term.* This is because if M_X, $M_{X'} \ll m_\phi$, the energy densities of X and X' are subdominant to ρ_ϕ during the modulus dominated era; a more detailed argument for this is presented in Appendix C. Given this approximation, the solutions to (5.7) do not depend on the branching fractions of X. Thus the approximate solutions for R and R' can be found readily by integrating the modulus decay term:

$$\begin{aligned} R(A) &\approx \left(\frac{c_\rho}{\Phi_I}\right)^{1/2}(1-\eta)\int_1^A (1-\bar{B})A'^{3/2}\Phi(A')\,dA';\; R'(A) \approx \frac{\eta}{1-\eta}R(A) \quad (5.14)\\ R_{\text{final}} &\approx (1-\eta)(1-B_{\text{eff}})\,\Gamma\left(\frac{5}{3}\right)\left[\left(\frac{3}{2}\right)^{2/3}\left(\frac{\Phi_I}{c_\rho}\right)^{1/3}\Phi_I\right];\; R'_{\text{final}} \approx \frac{\eta}{1-\eta}R_{\text{final}}. \end{aligned}$$

In the second line of (5.14), R_{final} represents the *late time* solution for R, i.e when the scale factor $A \gg A_*$. Note that $R \approx R_{\text{final}}$ during the radiation dominated era. We have approximated $\bar{B}$ as

$$B_{\text{eff}} \equiv \frac{B_X\left({M_X}^2 + 3{T_D}^2\right)^{1/2} + B_{X'}\left({M_{X'}}^2 + 3{T_D'}^2\right)^{1/2}}{m_\phi}\,, \tag{5.15}$$

where T_D and T'_D approximately correspond to the temperatures at which the integrand (5.14) peaks. These temperatures characterize the transition between modulus and radiation domination, and are defined more precisely in Section 5.2.1.2. To obtain the result above for R_{final}, we have expanded the function obtained after the integration as a series expansion in $\frac{c_\rho}{\Phi_I}$ with $\frac{c_\rho}{\Phi_I} \ll 1$ and kept the leading term. This can be justified by taking Φ_I as given by (5.11), where H_I is the Hubble parameter when the modulus ϕ starts dominating the energy density of the Universe. Thus, for $H_I = \gamma\,\Gamma_\phi$ with $\gamma \gg 1$,[4] one finds $\frac{c_\rho}{\Phi_I} = \frac{1}{\gamma^2} \ll 1$.

5.2.1.2 Temperature-scale factor relation and the "maximum" temperature

The temperature of a system is measured by the radiation energy density, and the relation between the two is given in general by:

$$T = \left(\frac{30}{\pi^2 g_*(T)}\right)^{1/4}\frac{R^{1/4}}{a} = \left(\frac{30}{\pi^2 g_*(T)}\right)^{1/4}\frac{R^{1/4}}{(A/T_{RH})}\,. \tag{5.16}$$

In a radiation dominated Universe, it is well known that $R^{1/4} = (\rho_R^{1/4}\,a)$ remains constant with time, giving $T \propto a^{-1}$. However, the situation is different within a modulus dominated

---

[4] We expect $\gamma \gg 1$ because the modulus dominates the energy density of the universe when $m_\phi \gtrsim H \gg \Gamma_\phi$.

Universe since $R^{1/4}$ does not remain constant with time. It can be shown that at early times when $T \gg T_{RH}$, $\Phi \approx \Phi_I$ and the temperatures and scale factor are related approximately by [105]:

$$T \approx \left(\frac{8^8}{3^3 5^5}\right)^{1/20} \left(\frac{g_*(T_{\max})}{g_*(T)}\right)^{1/4} T_{\max} \left(A^{-3/2} - A^{-4}\right)^{1/4}, \tag{5.17}$$

where $T_{\max}$, the maximum temperature attained during modulus domination, is given by:

$$T_{\max} \equiv (1-\eta)^{1/4} \left(\frac{3}{8}\right)^{2/5} \left(\frac{5}{\pi^3}\right)^{1/8} \left(\frac{g_*(T_{RH})^{1/2}}{g_*(T_{\max})}\right)^{1/4} (M_{\text{pl}} H_I T_{RH}^2)^{1/4}. \tag{5.18}$$

Thus, we see that the temperature has a more complicated dependence on the scale factor compared to that in radiation domination. Using the fact that $H_I = \gamma\,\Gamma_\phi$ with $\gamma \gg 1$, one finds that $T_{\max} \sim \gamma^{1/4} T_{RH}$. From (5.14) it is straightforward to relate the visible and dark sector temperatures:

$$T' \approx \left(\frac{\eta\, g_*(T)}{(1-\eta)\, g'_*(T')}\right)^{1/4} T \implies \xi \equiv \frac{T'}{T} \approx \left(\frac{\eta\, g_\star(T)}{(1-\eta) g'_\star(T')}\right)^{1/4}. \tag{5.19}$$

Combining (5.18) and (5.19) gives $T'_{\max}$ for the dark sector. As mentioned in Section 5.1.1, bounds on N_{eff} at both $T_{BBN} \sim 1$ MeV and $T_{CMB} \sim 1$ eV constrain T'_{BBN}/T_{BBN} and T'_{CMB}/T_{CMB}, which through (5.19) can be mapped into a constraint on η. Comparing (5.19) with the N_{eff} bound (5.1), we see that the resulting constraint on η is insensitive to $g'_*(T')$ assuming $g'_*(T') \neq 0$. Taking $g_*(T_{BBN}) = 10.75$ and $g_*(T_{CMB}) = 3$, the ΔN_{eff} constraints (5.1) imply $\eta \lesssim 0.20$ (BBN) and $\eta \lesssim 0.06$ (CMB).

In the presence of dark radiation, T_{RH} as defined in (5.3) no longer corresponds to the visible sector temperature when $H = \Gamma_\phi$, assuming the modulus has completely decayed ($\Phi = 0$). Instead, we define the temperatures T_D, T'_D as the visible and dark sector temperatures when $H\big|_{\Phi=0} = \Gamma_\phi$:

$$H\big|_{\Phi=0} = \frac{(8\pi/3)^{1/2}}{M_{\text{pl}}} (\rho_R + \rho_{R'})^{1/2} = \frac{(8\pi/3)^{1/2}}{M_{\text{pl}}} \left(\frac{\rho_R}{1-\eta}\right)^{1/2} = \Gamma_\phi$$

$$\Rightarrow T_D \approx T_{RH}(1-\eta)^{1/4}, \quad T'_D \approx \left(\frac{g_*(T_D)}{g'_*(T'_D)}\right)^{1/4} \eta^{1/4}\, T_{RH} \tag{5.20}$$

The bounds from N_{eff} discussed above imply $T_D \approx T_{RH}$. Hence, for simplicity we will set $g_*(T_{RH}) = g_*(T_D)$. It is also useful to compute the scale factor A_D which corresponds to the temperature T_D, T'_D. We compute A_D by substituting $T = T_D$ and $R = R_{\text{final}}$ in (5.16):

$$A_D = \left[\Gamma(5/3)\,(3/2)^{2/3}\,(1 - B_{\text{eff}})\right]^{1/4} \left(\frac{\Phi_I}{c_\rho}\right)^{1/3} \approx 1.5(1 - B_{\text{eff}})^{1/4} \left(\frac{\Phi_I}{g_*(T_{RH})}\right)^{1/3} \tag{5.21}$$

From the definition of $A_\star$ in (5.13), we see that $A_\star \sim A_D$.

We caution the reader that the definitions of T_D, T'_D and A_D established above are limited in the following sense. The above expressions for T_D, T'_D and A_D were derived from $H = \Gamma_\phi$ assuming that the universe has reached radiation domination, i.e. $\Phi = 0$ and $R = R_{\text{final}}$, $R' = R'_{\text{final}}$. However, modulus decay is a continuous process which occurs when $H \sim \Gamma_\phi$, but does not have a well-defined start or end point. Upon solving the Boltzmann equations, one finds that when $H = \Gamma_\phi$, the modulus has not finished decaying and the radiation dominated phase has not yet been reached ($R \neq R_{\text{final}}$). In the next subsection we will verify this fact graphically, utilizing the full numerical solutions for Φ and R (see Figure 5.2 below). Despite this ambiguity, we find T_D, T'_D and A_D to be useful qualitative proxies for the temperature and scale factor at which the universe transitions from the modulus dominated to radiation dominated era.

5.2.1.3 Approximate solution for X

Now consider the Boltzmann equation for X. Motivated by earlier statements, we are interested in the case where X is a LOSP with weak scale mass and annihilation cross section; thus X_{eq} will be exponentially suppressed for temperatures of a few GeV. In our analysis, we will mostly consider the situation that the LOSP X decays before the modulus (typically much before), i.e. $\Gamma_X > \mathcal{O}(1)\Gamma_\phi$. Such a condition can be naturally achieved since the modulus decays by Planck-suppressed operators. In Appendix D, we will briefly consider the case where $\Gamma_X \lesssim \Gamma_\phi$.

In the Boltzmann equation for X', the X decay term grows like $A^{1/2}$; thus we are interested in the solution for X in the low temperature regimes where X_{eq} can be neglected (this approximation is justified in Appendix D). With this approximation, the Boltzmann equation for X can be written as:

$$\frac{dX}{d\log A} = -\left(\frac{X^2}{X_{\text{crit}}} + \frac{A^3}{X_{\text{crit}}\,\langle\sigma v\rangle}\frac{\Gamma_X}{g_X T_{RH}^3}X\right) + \left(\frac{A^3}{X_{\text{crit}}\,\langle\sigma v\rangle}\frac{c_\rho^{1/2} B_X}{m_\phi c_1^{1/2} M_{pl}}\Phi\right), \tag{5.22}$$

where X_{crit} is the critical value required for annihilations to be efficient for a given value of the Hubble parameter. More precisely, $X_{\rm crit}$ is given by:

$$X_{\rm crit} \equiv (n_X)_{\rm crit}\, \frac{A^3}{T_{RH}^3} = \frac{H A^3}{\langle\sigma v\rangle\, T_{RH}^3} = \frac{\widetilde{H} A^{3/2}}{c_1^{1/2}\, M_{\rm pl} T_{RH} \,\langle\sigma v\rangle}\,. \tag{5.23}$$

Now, if the processes for depletion of X (the first and second terms on the right hand side of (5.22)) and the production of X (the third term in the right hand side of (5.22)) are *larger* than X itself, then these are each faster than the Hubble rate and one rapidly reaches a situation where the two processes cancel each other, giving rise to what is known as *quasi-static equilibrium* (QSE) [107]. The QSE solution is found by equating the right hand side of (5.22) to zero:

$$X_{\rm QSE} = \frac{\Gamma_X A^3}{2\, T_{RH}^3 g_X \,\langle\sigma v\rangle} \left[\left(1 + \frac{4 g_X^2 B_X c_\rho^{1/2}\, \Phi\, {T_{RH}}^6 \,\langle\sigma v\rangle}{c_1^{1/2} A^3\, m_\phi M_{pl} \Gamma_X^2}\right)^{1/2} - 1\right]. \tag{5.24}$$

Given the criteria described above (5.24), QSE occurs when:

$$\left(X_{\rm QSE} + \frac{A^3}{\langle\sigma v\rangle}\frac{\Gamma_X}{g_X\, T_{RH}^3}\right) > X_{\rm crit} \;\&\; \frac{A^3}{\langle\sigma v\rangle}\left[\left(\frac{c_\rho^{1/2} B_X}{c_1^{1/2} m_\phi\, M_{pl}}\right)\left(\frac{\Phi}{X_{\rm QSE}}\right)\right] > X_{\rm crit}\,. \tag{5.25}$$

Upon inspection, one finds that the QSE condition (5.25) is equivalent to the familiar condition $\Gamma_X/g_X > H$. *Thus, we see that as long as* $\Gamma_X > g_X\,\Gamma_\phi$*, the QSE condition will be satisfied during the modulus dominated era such that* $X \approx X_{\rm QSE}$ *for* $\Gamma_X > g_X H$.

We can gain further insight into the QSE solution for X by rewriting (5.24) as:

$$\begin{aligned} X_{\rm QSE} &= \frac{\Gamma_X A^3}{2 T_{RH}^3 g_X \,\langle\sigma v\rangle}\left[\left(1 + \frac{\langle\sigma v\rangle}{\langle\sigma v\rangle_*}\right)^{1/2} - 1\right], \\ \Longrightarrow\; X_{\rm QSE} &\approx \left(\frac{g_X\, b\, B_X c_\rho^{1/2}\, T_{RH}^3}{c_1^{1/2}\Gamma_X m_\phi M_{pl}}\right)\Phi\,;\; b \approx \begin{cases} 1; \langle\sigma v\rangle \ll \langle\sigma v\rangle_* \\ 2\left(\frac{\langle\sigma v\rangle^c}{\langle\sigma v\rangle}\right)^{1/2}; \langle\sigma v\rangle \gg \langle\sigma v\rangle_* \end{cases} \end{aligned} \tag{5.26}$$

Physically, the QSE solution for X occurs when moduli decay into X, and X decay into X', balance one another; this explains the dependence of X_{QSE} on Φ. In the above expression,

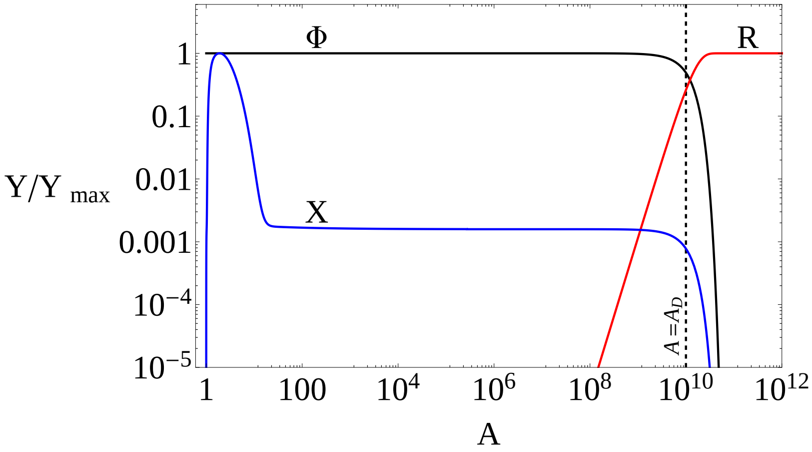

Figure 5.2: Plots of the exact solutions for $Y = \Phi,\ R$ and X (normalized to their maximum values) as functions of the scale factor A. We have taken $H_I = 10^{15}\Gamma_\phi$, $B_X = 0.1$, $\langle\sigma v\rangle = 10^{-7}$ GeV^{-2} and $\Gamma_X = 10^{-5}$ GeV. All other parameters taken to their benchmark values (5.5). The dashed vertical line represents the scale factor $A = A_D$ defined in (5.21), which characterizes the transition between a modulus dominated and a radiation dominated universe.

$\langle\sigma v\rangle_*$ is defined as:

$$\begin{aligned}
\langle\sigma v\rangle_* &\equiv \left(\frac{1}{4g_X^2 B_X}\right)\left(\frac{A^3}{\Phi_I}\right)\sqrt{\frac{c_1}{c_\rho}}\left(\frac{M_{pl}m_\phi {\Gamma_X}^2}{T_{RH}^6}\right) && (5.27)\\
&\approx 4.48\times 10^{24}\ \text{GeV}^{-2} && (5.28)\\
&\quad\times\left(\frac{5}{g_X^2\,B_X}\right)\left(\frac{A}{A_D}\right)^3\left(\frac{m_\phi}{50\,\text{TeV}}\right)\left(\frac{10\,\text{MeV}}{T_{RH}}\right)^6\left(\frac{\Gamma_X}{10^{-5}\,\text{GeV}}\right)^2\left(\frac{10.75}{g_*(T_{RH})}\right)^{3/2}.
\end{aligned}$$

Note that for the benchmark choice of parameters in (5.5), and Γ_X not extremely small, $\langle\sigma v\rangle_*$ is quite large (compared to a WIMP cross-section $\sim 10^{-7} - 10^{-10}\,\text{GeV}^{-2}$). We expect the same qualitative conclusion as long as the portal coupling is not extremely tiny. Thus for Supersymmetric models where X is the LOSP, we expect $\langle\sigma v\rangle \ll \langle\sigma v\rangle_*$, and hence $b \approx 1$ in the QSE solution for X in the second line of (5.26).

Figure 5.2 shows a plot of the solutions for the values of Φ, R and X (normalized to their maximum values) as functions of the scale factor A for the choice of benchmark parameters as in (5.5). As can be seen from (5.12), (5.14) and (5.26), respectively, the solutions for Φ, R and X do not depend on M_X, $M_{X'}$ or $\langle\sigma v\rangle'$ to a good approximation. Moreover the solution for X depends does not depend on $\langle\sigma v\rangle$ for most models of interest in which $\langle\sigma v\rangle \ll \langle\sigma v\rangle_*$ as we have just discussed above.

5.2.2 Classifying Production Mechanisms for Relic Dark Matter

We now move on to studying the main quantity of interest – the Boltzmann equation for X', whose solution will give us the expression for the relic abundance $\Omega_{DM}h^2$ of dark matter X' in terms of a subset of the parameters (5.2) appearing in the Boltzmann equations. More precisely, the X' relic abundance is given by:

$$\Omega_{DM}h^2 = \frac{\rho_{X'}(T_f')}{\rho_R(T_f)}\frac{T_f}{T_{\text{now}}}\Omega_R h^2 = M_{X'}\frac{X'(T_f')}{R(T_f)}\frac{A_f T_f}{T_{\text{now}}T_{RH}}\Omega_R h^2\,. \tag{5.29}$$

In the above expression, T_f is the temperature at any very late time in which the universe has become radiation dominated ($T_f \ll T_D$) and the X' comoving abundance has become constant. The parameters $T_{\text{now}} \approx 2.35 \times 10^{-13}$ GeV and $\Omega_R h^2 \approx 4.17 \times 10^{-5}$ are the present day temperature and radiation relic density. Taking $R(T_f) \approx R_{\text{final}}$ and using (5.16) to relate A_f and T_f, (5.29) can be written as:

$$\Omega_{DM}h^2 \approx L^{-3/4}\frac{X'(T_f')}{\Phi_I}\frac{M_{X'}}{T_{\text{now}}}\Omega_R h^2, \quad L \equiv (1-\eta)(1-B_{\text{eff}})\Gamma(5/3)\left(\frac{3}{2}\right)^{2/3} \tag{5.30}$$

In order to derive semi-analytic approximations for $X'(T_f)$ and $\Omega_{DM}h^2$, we will solve the Boltzmann equation for X' given the approximations stated in the previous sections. In the following we will show that $X'(T_f) \propto \Phi_I$, so $\Omega_{DM}h^2$ is insensitive to Φ_I as mentioned above.

Using the approximate solutions for Φ, R, R' and X in (5.12), (5.14) and (5.26), respectively, we can reduce the system of Boltzmann equations in (5.7) to a single ordinary differential equation for the evolution of X':

$$\frac{dX'}{dA} \approx \frac{c_1^{1/2}\, M_{\text{pl}}T_{RH}\,\langle\sigma v\rangle'\, A^{-5/2}}{\widetilde{H}}({X'_{\text{eq}}}^2 - X'^2) + \frac{c_1^{1/2}\, A^{1/2}}{\widetilde{H}}\left(\frac{c_\rho^{1/2}T_{RH}B_{X'}}{c_1^{1/2}m_\phi}\Phi + \frac{\Gamma_X M_{\text{pl}}}{g_X T_{RH}^2}X_{\text{QSE}}\right) \tag{5.31}$$

where X_{QSE} is defined in (5.26). Note that if X does not decay to X', the X'_{QSE} term in (5.31) is absent. Using a similar definition for the critical annihilation for X' as was used for X in (5.23), one can rewrite (5.31):

$$\begin{aligned} \frac{dX'}{d\log A} &\approx -\left[\frac{X'^2}{X'_{\text{crit}}}\right] + \left[\frac{{X'_{\text{eq}}}^2}{X'_{\text{crit}}} + \frac{A^3}{X'_{\text{crit}}\,\langle\sigma v\rangle'}\left(\frac{c_\rho^{1/2}B_{tot}}{c_1^{1/2}m_\phi M_{pl}}\Phi\right)\right] \qquad (5.32)\\ X'_{\text{crit}}(A) &\equiv \frac{HA^3}{\langle\sigma v\rangle'\, T_{RH}^3} = \frac{\widetilde{H}A^{3/2}}{c_1^{1/2}\, M_{\text{pl}}T_{RH}\,\langle\sigma v\rangle'}, \end{aligned}$$

where $B_{tot} \equiv B_X + B_{X'}$ if X decays to X'[5], and $B_{tot} \equiv B_{X'}$ if X does not decay to X'. Just as for the case of X, if the processes of depletion of X' (first term on the right hand side of (5.32)) and production of X' (second, third and fourth terms on the right hand side of (5.32)) are each greater than X' itself, X' will rapidly reach a quasi-static equilibrium (QSE) attractor solution such that terms on the right hand side of (5.32) cancel among themselves:

$$X'_{\rm QSE}(A) = \left[\frac{A^3}{\langle \sigma v \rangle'} \left(\frac{c_\rho^{1/2} B_{tot}}{c_1^{1/2} m_\phi M_{pl}} \Phi \right) + {X'_{\rm eq}}^2 \right]^{1/2} . \tag{5.33}$$

Comparing (5.32) and (5.33), and using (5.26) for the QSE solution for X, we see that the QSE conditions hold when:

$$X'_{\rm QSE} > X'_{\rm crit} \,. \tag{5.34}$$

Note that in contrast to X for $\langle \Gamma_X \rangle > \Gamma_\phi$, X' does not necessarily enter QSE during the modulus dominated phase. One reason for this is that in contrast to X, which is assumed to be a WIMP, we are exploring a much more general set of possibilities for the mass and interactions of the DM particle X'.

In order to understand better the broad possibilities that could arise for X', it is important to find the conditions necessary for QSE to hold at $A \approx A_D$. If the QSE conditions hold at $A \approx A_D$, then the positive contribution to X' from modulus decay is annihilated away such that X maintains its QSE value. In this case, the final X' abundance is insensitive[6] to modulus decay parameters such as m_ϕ and B_{tot}. Conversely if QSE does not hold at $A \approx A_D$, $\Omega_{X'} h^2$ will be sensitive to contributions from modulus decay, along with other sources for X' production during the modulus dominated era. Comparing (5.32) and (5.33), we see that requiring $X'_{\rm QSE}(A_D) > X'_{\rm crit}(A_D)$ places a lower bound on $\langle \sigma v \rangle'$. Keeping the above statements in mind, it is useful to define a critical annihilation cross section such that $X'_{\rm QSE} = X'_{\rm crit}$ at $A = A_D$, to delineate the various possibilities:

$$\langle \sigma v \rangle'_c \equiv \left(\frac{c_\Gamma^{1/2}}{c_1 \, B_{\rm tot}} \right) \left(\frac{m_\phi}{T_{RH}^2 M_{\rm pl}} \right); \qquad M_{X'} \gg T'_D \tag{5.35}$$

$$\begin{aligned} \langle \sigma v \rangle'_c &\equiv \left(\frac{\pi^2 \, c_\Gamma^{-1/2}}{\theta \, g' \, \zeta(3)} \left(\frac{2}{3} \right)^{1/4} \frac{1}{\Gamma(5/3)^{3/8}} \right) \left(\frac{g'_*(T'_D)}{g_*(T_D) \, \eta} \right)^{3/4} \frac{1}{T_{RH} \, M_{\rm pl}}; \qquad M_{X'} \ll T'_D \\ &\approx 2.35 \left(\frac{3.0}{\theta \, g} \right) \left(\frac{g'_\star(T'_D)}{\eta} \right)^{3/4} \left(\frac{10.75}{g_\star(T_{RH})} \right)^{1/4} \frac{1}{T_{RH} \, M_{\rm pl}} \end{aligned} \tag{5.36}$$

---

[5] Note that as discussed below (5.27), $\langle \sigma v \rangle \ll \langle \sigma v \rangle_*$ for most models where X is a LOSP, for which $b \approx 1$ from (5.26). Therefore, we have used the expression for $X_{\rm QSE}$ with $b \approx 1$ in (5.32).

[6] Modulo logarithmic sensitivity, as will be discusssed in Section 5.2.3.1.

where we have approximated $\widetilde{H} \approx \Phi_I$ at $A = A_D$. In the above expressions, $c_\Gamma \equiv \left(\frac{45}{4\pi^3\, g_\star(T_{RH})}\right)$, g' is the degrees of freedom of X', and $\theta = 1\,(3/4)$ for bosonic (fermionic) X'. The above expressions were obtained by taking $X'_{\rm eq} \to 0$ in the $M_{X'} \gg T'_D$ case and $X'_{\rm QSE} = X'_{\rm eq}$ in the $M_{X'} \ll T'_D$ case.

In the following sections, we will classify production mechanisms for X' according to whether or not $\langle\sigma v\rangle'|_{T'=T'_D} > \langle\sigma v\rangle'_c$, or equivalently whether or not X' annihilations are efficient at T'_D. *To simplifiy the following analysis, we will assume that $\langle\sigma v\rangle'$ is temperature independent.* The generalization of our results to temperature dependent $\langle\sigma v\rangle'$ is presented in Appendix F.

5.2.3 Efficient Annihilation at T'_D: $\langle\sigma v\rangle' > \langle\sigma v\rangle'_c$

If $\langle\sigma v\rangle' > \langle\sigma v\rangle'_c$, X' tracks its QSE value until $X'_{\rm QSE}$ drops below $X'_{\rm crit}$ at $A \gtrsim A_D$. When $X'_{\rm QSE}$ drops below $X'_{\rm crit}$, annihilations are no longer efficient and the comoving X' abundance becomes constant. The dynamics of this process, along with the resulting parametrics for $\Omega_{X'}$, depends on whether or not the freeze-out temperature for X', $\hat{T}'_{FO}$, is larger than T'_D. Here $\hat{T}'_{FO}$ is the X' freeze-out temperature, which is computed assuming a radiation dominated universe (5.39). If $\hat{T}'_{FO} > T'_D$ we can neglect $X'_{\rm eq}$ in $X'_{\rm QSE}$ for $T \sim T_D$; in this case $X'_{\rm QSE} \propto \Phi^{1/2}$, and $X'_{\rm QSE}$ drops below $X'_{\rm crit}$ when the modulus decays at $T' \sim T'_D$. If instead $T'_D > \hat{T}'_{FO}$, X' remains in thermal equilibrium during the onset of radiation domination ($X'_{\rm QSE} \approx X'_{\rm eq}$ for $T' \lesssim T'_D$). In this case the X' relic abundance is determined by the standard freeze-out mechanism.

5.2.3.1 Non-relativistic quasi-static equilibrium

First consider the case where $\hat{T}'_{FO} > T'_D$ such that $X'_{\rm eq}$ can be neglected for $T' \gtrsim T'_D$. Assuming $\langle\sigma v\rangle' > \langle\sigma v\rangle'_c$, X' tracks $X'_{\rm QSE} \propto \Phi^{1/2}$ until $A \gtrsim A_D$, after which the ratio $X'_{\rm QSE}/X'_{\rm crit}$ begins to drop exponentially due to the decay of Φ according to (5.12). The final X' value is given by $X'_{\rm QSE}(A_c)$, where A_c is determined by solving the transcendental equation:

$$\begin{aligned} X'_{\rm QSE}(A_c) &= \frac{1}{\kappa}X'_{\rm crit}(A_c) \Rightarrow \left(\frac{\Phi}{\widetilde{H}^2}\right)\Bigg|_{A_c} = \frac{\langle\sigma v\rangle'_c}{\kappa^2\,\langle\sigma v\rangle'} \\ \log\left[\tilde{A}_c\right] &= \frac{2}{3}c_\rho^{1/2}\left[\tilde{A}_c\right]^{3/2} + \log\left[\left(\frac{3}{2}\right)^{2/3}\frac{\Gamma(5/3)}{{c_\rho}^{1/3}}\right] - \log\left[\left(\frac{\kappa^2\,\langle\sigma v\rangle'}{\langle\sigma v\rangle'_c} - 1\right)\right]. \end{aligned} \tag{5.37}$$

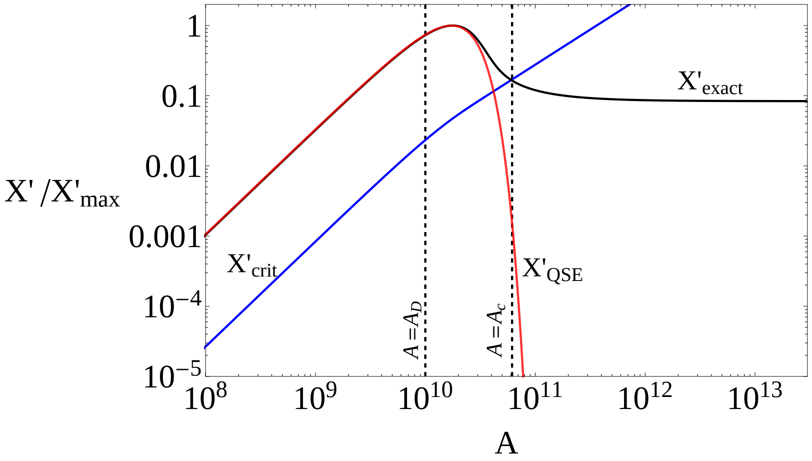

Figure 5.3: Plot of the exact solution of the Boltzmann equations for X' (normalized to its maximum value) as a function of the scale factor A corresponding to the $QSE_{\rm nr}$ mechanism. We have taken $H_I = 10^{15}\Gamma_\phi$, $\langle\sigma v\rangle' = 10^{-6}\,{\rm GeV}^{-2}$ and $M_{X'} = 10$ GeV, with all other parameters set to the benchmark values (5.5). We have also plotted $X'_{\rm crit}$ (5.32) and $X'_{\rm QSE}$ (5.33). The horizontal dashed line corresponding to $A = A_c$ is determined by solving the transcendental equation (5.37) for A_c.

We have defined $\tilde{A}_c \equiv A_c\,{\Phi_I}^{1/3}$ and have used the approximation $R(A_c) \approx R_{\rm final}$. Taking $\kappa \approx 2$ gives close agreement with the full numerical result. We denote the above mechanism for DM production as $QSE_{\rm nr}$.

Upon solving (5.37) for $\tilde{A}_c$, it is straightforward to compute $\Omega_{DM}h^2$ using (5.30) with $X'(T'_f) = \kappa^{-1}X'_{\rm crit}(A_c)$:

$$\begin{aligned}\Omega\, h^2\,[QSE_{\rm nr}] &\approx \frac{B_{\rm tot}^{1/2}}{L^{3/4}c_\Gamma^{1/4}}\,\frac{\tilde{A}_c^{3/2}\exp\left(-\frac{1}{3}c_\rho^{-1/2}\tilde{A}_c^{3/2}\right)}{(M_{\rm pl}m_\phi\,\langle\sigma v\rangle')^{1/2}}\left[\frac{M_{X'}}{T_{\rm now}}\right]\left[\Omega_R h^2\right] \\ &\approx \left[\frac{(\Gamma(\frac{5}{3})\,(\frac{3}{2})^{2/3})^{1/2}}{\kappa\, c_\rho^{1/6}\; c_1^{1/2}L^{3/4}}\right]\left[\frac{\tilde{A}_c}{M_{X'}M_{\rm pl}\,\langle\sigma v\rangle'}\frac{M_{X'}}{T_{RH}}\right]\left[\frac{M_{X'}}{T_{\rm now}}\right]\left[\Omega_R h^2\right].\end{aligned} \tag{5.38}$$

In the above, we have made the approximation $e^{-\frac{2}{3}\left[\frac{c_\rho}{\Phi_I}\right]^{1/2}} \approx 1$, see discussion below (5.12). Also, in the second line, we have used (5.37) to get rid of the exponential factor in the first line. The factor $\tilde{A}_c$ in the numerator depends logarithmically on both $\langle\sigma v\rangle'$ and $\langle\sigma v\rangle'_c$.

5.2.3.2 Standard freezeout during radiation domination

Now consider the case where $\hat{T}'_{FO} < T'_D$ with $\langle\sigma v\rangle' > \langle\sigma v\rangle'_c$. Then, as discussed above, $X'_{\rm QSE}(T'_D) \approx X'_{\rm eq}(T'_D)$, which implies that X' is in thermal equilibrium at $T' \approx T'_D$ and freezes out at some $\hat{T}'_{FO} < T'_D$ when $X'_{\rm eq}$ drops below $X'_{\rm crit}$. *The universe is radiation dominated for $T' \lesssim T'_D$; thus the X' relic abundance is determined by the standard thermal freeze-out mechanism.* Furthermore, there are two possible sub cases - i) non-relativistic freezeout during radiation domination when $T'_D > M'_X > \hat{T}'_{FO}$, which we denote as $FO^{\rm rad}_{\rm nr}$, and ii) relativistic freezeout when $T'_D > \hat{T}'_{FO} > M_{X'}$, which we denote as $FO^{\rm rad}_{\rm r}$. The relic abundance in the two cases are given by (5.29) with $T_f = \hat{T}_{FO}$, $T'_f = \hat{T}'_{FO}$ and $\rho_{X'}(\hat{T}'_{FO})$ determined by the standard freeze-out calculation. Specifically, $\rho_{X'}(\hat{T}'_{FO}) = \rho_{X'_{\rm eq}}(\hat{T}'_{FO})$, where $\hat{T}'_{FO}$ is defined by $n'_{\rm eq}(T'_{FO}) \equiv H/\left<\sigma v\right>'$. Assuming non-relativistic freeze-out, $\hat{T}'_{FO}$ is given by solving the transcendental equation:

$$\hat{x}'_F \equiv \frac{M_{X'}}{T'_{FO}} = \log\left(\frac{3}{8\pi^3}\sqrt{\frac{10\,\eta}{g'_*(T'_{FO})}}\,\left<\sigma v\right>'\,g' M_{X'} M_{\rm pl}(\hat{x}'_F)^{1/2}\right) \tag{5.39}$$

and the resulting relic abundance is given by:

$$\frac{\Omega\, h^2\;[FO^{\rm rad}_{\rm nr}]}{\Omega_R\, h^2} \approx \left[\frac{4\sqrt{5}\eta^{1/4}}{\sqrt{\pi}\,(1-\eta)^{3/4}}\right]\left[\frac{1}{g_*(T_{FO})g'_*(T'_{FO})}\right]^{1/4}\left[\frac{\hat{x}'_F}{T_{now}\,M_{pl}\,\left<\sigma v\right>'}\right] \tag{5.40}$$

If instead $\hat{x}'_F \lesssim 3$, X' freeze-out occurs relativistically, and:

$$\frac{\Omega\, h^2\;[FO^{\rm rad}_{\rm r}]}{\Omega_R\, h^2} \approx \left[\frac{30\,\zeta(3)}{\pi^4}\right]\left[\frac{\eta g_*(T_{FO})}{(1-\eta)\,g'_*(T'_{FO})}\right]^{3/4}\left[\frac{c_\xi}{g_\star(T_{FO})}\right]\left[\frac{M_{X'}}{T_{\rm now}}\right] \tag{5.41}$$

where $c_\xi = g'\;(3g'/4)$ for bosons (fermions).

Note that although the *mechanism* for DM production discussed here is standard thermal freezeout, the relevant parametric region is very different compared to that of usual thermal WIMP freezeout. In particular, here $\hat{T}'_{FO}$ is smaller than $T'_D \approx T_{RH}\,(\eta)^{1/4}\,\left(\frac{g_\star(T_D)}{g'_\star(T'_D)}\right)^{1/4} \lesssim (0.1-0.5)\,T_{RH}$ for reasonable choices of parameters. This implies that $M_{X'} < \hat{x}'_F T'_D \lesssim 10 \times T_{RH}$. Furthermore, for the cosmological scenarios described in the introduction and in Section 5.3, one expects T_{RH} to be in the range: few MeV $\lesssim T_{RH} \lesssim 100$ MeV. *Thus, the DM in this case is much lighter than a typical electroweak-scale WIMP, even if the underlying mechanism is non-relativistic freezeout during radiation domination ($FO^{\rm rad}_{\rm nr}$).* On the other hand, DM undergoing *relativistic* thermal freezeout in the dark sector ($FO^{\rm rad}_{\rm r}$) is qualitatively similar to the case of neutrino decoupling in the visible sector. We reiterate that in all other regions of $M_{X'}$ and $\left<\sigma v\right>'$ parameter space, the standard thermal freeze-out calculation will not be valid.

5.2.4 Inefficient Annihilation at T'_D: $\langle \sigma v \rangle' < \langle \sigma v \rangle'_c$

We now consider the case where $\langle \sigma v \rangle' < \langle \sigma v \rangle'_c$ such that X' is not in QSE for $T \gtrsim T_D$. In contrast to the previous case, the X' relic abundance will be sensitive to both early-time X' production during the modulus dominated era and the modulus branching ratio B_{tot}. Because the annihilation rate $\Gamma(X') \sim n_{X'}^2 \langle \sigma v \rangle'$ is much smaller than the Hubble parameter for $T' \gtrsim T'_D$, the X'^2 term in (5.31) can be neglected for $T' \gtrsim T'_D$. The Boltzmann equation for X' becomes linear in this limit, and the contributions to Ω_{DM} can be separated into two sources:

$$\Omega_{DM}\, h^2 = \Omega_{\rm ann}\, h^2 + \Omega_{\rm decay}\, h^2. \tag{5.42}$$

The first term, $\Omega_{\rm decay}\, h^2$, is the contribution from modulus and X decays. This term can be computed by taking $\widetilde{H} = {\Phi_I}^{1/2}$ and integrating the second term in the RHS of (5.31) to $A = A_f \gg A_*$. Taking $\exp(-2c_\rho^{1/2}/3{\Phi_I}^{1/2}) \approx 1$, equation (5.30) gives:

$$\Omega_{\rm decay}\, h^2 \approx L^{-3/4} \left[B_{\rm tot}\, \frac{T_{RH}}{m_\phi} \right] \frac{M_{X'}}{T_{\rm now}} \left[\Omega_R\, h^2 \right] \tag{5.43}$$

On the other hand, as the name suggests, $\Omega_{\rm ann}\, h^2$ parameterizes contributions to X' production which arise from the annihilation term in (5.31). This has been discussed in [105] in models with a single sector. There are two qualitatively different cases regarding the parameterics of $\Omega_{\rm ann}\, h^2$.

The first case arises when the DM particle X' attains equilibrium at high temperatures (but $\langle \sigma v \rangle'$ is still smaller than $\langle \sigma v \rangle'_c$) and freezes out during *modulus domination*; hence $T'_{\rm max} > T'_{FO} > T'_D$. Here T'_{FO} is the X' freeze-out temperature computed assuming a *modulus* dominated universe (5.44). Now, one might naively think that both non-relativistic and relativistic thermal freezeout may be possible during modulus domination, just as they are during radiation domination (see section 5.2.3.2). However, as noted in [105], relativistic freeze-out cannot occur during modulus domination if $\langle \sigma v \rangle' \propto (T')^n$ with $n < 6$. To see this, note that the term in (5.32) corresponding to $R'R' \to X'X'$ inverse annihilations scales like ${X'_{\rm eq}}^2 \langle \sigma v \rangle' / X'_{\rm crit} \propto (T')^{(-6+n)}$ when X' is relativistic. Thus if X' decouples from the thermal bath of dark radiation while relativistic at some temperature $T'_{\rm dec}$, the X' comoving abundance will continue to grow for $T' < T'_{\rm dec}$ due to inverse annihilations, provided $n < 6$. In this work we will only consider $n < 6$; thus for the models considered here, freeze-out during modulus domination occurs only if $T'_{\rm max} > T'_{FO} > T'_D$ *and* $M_{X'} > T'_{FO}$.

The second case arises when $T'_{FO} > T'_{\rm max} > T'_D$ (X' never reaches equilibrium) or when $T'_{\rm max} > T'_{FO} > M_{X'}$ (X' decouples while relativistic). In this case, it turns out that

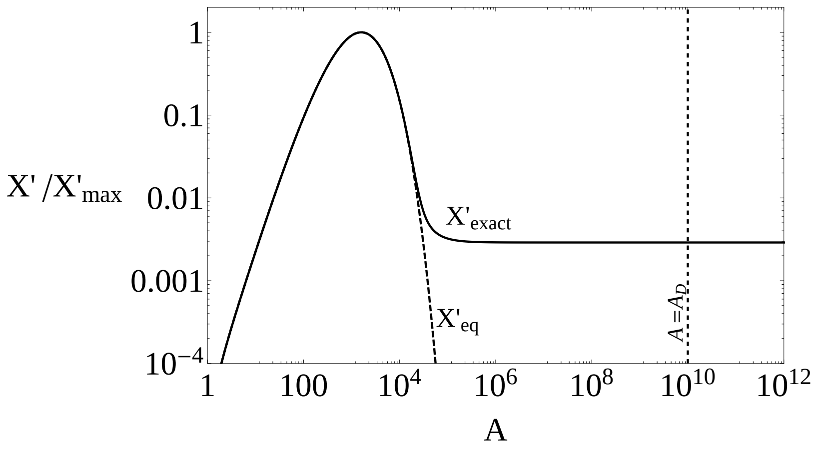

Figure 5.4: Plot of the exact solution for X' (normalized to its maximum value) as a function of the scale factor A corresponding to the $FO^{\rm mod}_{\rm nr}$ mechanism. We have taken $H_I = 10^{15}\Gamma_\phi$, $\langle\sigma v\rangle' = 10^{-6}\,{\rm GeV}^{-2}$, $M_{X'} = 10$ GeV as in Figure 5.3, but have instead chosen $B_{tot} = 0$ so that the QSE condition is not satisfied, see (5.35). All other parameters set to benchmark values (5.5). For comparison we have also plotted the comoving X' equilibrium number density X'_{eq}.

the contribution to DM abundance comes predominantly from *inverse annihilations* via $R'R' \to X'X'$, as will be seen shortly.

5.2.4.1 Non-relativistic freezeout during modulus domination

Let us first consider the case where X' reaches chemical equilibrium and then undergoes freeze-out during modulus domination ($T'_{\rm max} > T'_{FO} > T'_D$). From the arguments above, we note that freezeout can only occur when DM is non-relativistic, hence we denote this mechanism as $FO^{\rm mod}_{\rm nr}$. The X' freezeout temperature, defined as T'_{FO} such that $n^{\rm eq}_{X'}(T'_{FO})\,\langle\sigma v\rangle \equiv H(T'_{FO})$, is given by solving the following transcendental equation for $x'_F \equiv \frac{M_{X'}}{T'_{FO}}$:

$$x'_F = \ln\left[\left(\frac{3}{2\sqrt{10}\pi^3}\right)\left(\frac{g' g_*(T_{RH})^{1/2}}{g'_*(T'_{FO})}\right)\left(\frac{M_{\rm pl}}{M_{X'}}\right)\left[T^2_{RH}\,\langle\sigma v\rangle'\right]\eta\, {x'_F}^{5/2}\right] \tag{5.44}$$

where $x'_F \equiv \frac{M_{X'}}{T'_{FO}}$. Note that the above equation, and hence the parameters T'_{FO} and x'_F, are valid only if $T'_{\rm max} > T'_{FO} > T'_D$ and $M_{X'} > T'_{FO}$, i.e. $1 < x'_F < \left(\frac{M_{X'}}{T'_D}\right)$.

Then $\Omega_{\rm ann}h^2$ is given by (5.30) with $X'(T_f) = X'_{\rm eq}(T'_{FO})$:

$$\frac{\Omega_{\rm ann}\, h^2\ [FO^{\rm mod}_{\rm nr}]}{\Omega_R\, h^2} \approx \left[\frac{8\,\eta}{\sqrt{5\pi}\, L^{3/4}}\right] \left[\frac{g_*(T_{RH})^{1/2}}{g'_*(T'_{FO})}\right] \left[\frac{T_{RH}}{M_{X'}}\right]^3 \left[\frac{{x'_F}^{4}}{T_{now}\, M_{\rm pl}\, \langle\sigma v\rangle'}\right] \tag{5.45}$$

where x'_F is the solution of (5.44). From (5.44), it can be seen that the condition $x'_F > 1$ is equivalent to $\langle\sigma v\rangle' > \langle\sigma v\rangle'_0$ or $M_{X'} < M_0$ where:

$$\begin{aligned} \langle\sigma v\rangle'_0 (M_{X'}) &\equiv \left[\frac{2e\sqrt{10}\pi^3}{3}\right] \left[\frac{g'_*(T'_{FO})}{g' g_*(T_{RH})^{1/2}}\right] \left[\frac{M_{X'}}{M_{\rm pl}\, T_{RH}^2\, \eta}\right] \\ M_0\left(\langle\sigma v\rangle'\right) &\equiv \left[\frac{3}{2e\sqrt{10}\pi^3}\right] \left[\frac{g' g_*(T_{RH})^{1/2}}{g'_*(T'_{FO})}\right] \left[M_{\rm pl} T_{RH}^2\, \langle\sigma v\rangle'\ \eta\right] \end{aligned} \tag{5.46}$$

In addition, x'_F must be smaller than $M_{X'}/T'_D$, which puts an additional constraint on the parameters. Thus the parameter space for viable $FO^{\rm mod}_{\rm nr}$ is rather limited, as we will show in Section 5.3.

5.2.4.2 Non-relativistic and relativistic inverse annihilation

Finally, let us consider the situation when one of the conditions in the previous subsection, i.e. $T'_{\rm max} > T'_{FO} > T'_D$ or $M_{X'} > T'_{FO}$, is *not* satisfied. In this case, X' is instead populated by $R'R' \to X'X'$ inverse annihilations. This occurs if X' never reaches equilibrium for $T' < T'_{max}$, or if X' decouples from the thermal bath while relativistic. In either case ${X'}^2 \ll {X'_{eq}}^2$ for $T' \lesssim M_{X'}$, allowing us to neglect the ${X'}^2$ term in (5.31). Integrating the first term on the right hand side of (5.31) from $A = A_0 \equiv (8/3)^{2/5}$ to some scale factor $A = A_f$, one gets[7]:

$$X'(A_f) \approx c_1^{1/2}\, M_{\rm pl}\, \langle\sigma v\rangle'\, {T_{RH}}^{-5} \int_{A_0}^{A_f} dA\, \frac{A^{7/2}\, {n'_{\rm eq}}^2}{\widetilde{H}}\,. \tag{5.47}$$

While X' is relativistic, the integrand of (5.47) grows like $A^{5/4}$ in the modulus dominated phase ($\widetilde{H} \approx {\Phi_I}^{1/2}$) and falls like A^{-3} in the radiation dominated phase ($\widetilde{H} \approx \sqrt{R/A}$). Thus if $M_{X'} > T'_D$, X' production occurs predominantly when X' first becomes non-relativistic, while if $M_{X'} < T_{D'}$ X' production occurs predominantly at the transition between modulus domination and radiation domination.

In either case the important dynamics for X' production approximately occurs during

---

[7] A_0 corresponds to the scale factor at which $T = T_{\rm max}$, see (5.18).

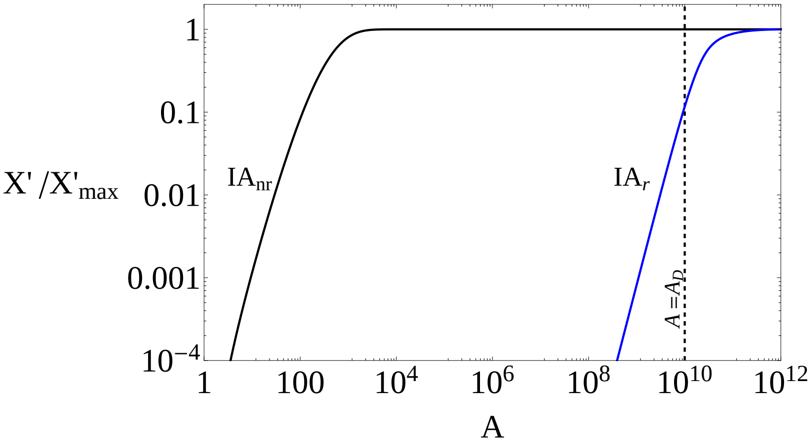

Figure 5.5: Plot of the exact solution of the Boltzmann equations for X' (normalized to its maximum value) as a function of the scale factor A corresponding to the IA_{nr} and IA_{r} mechanisms. We have chosen $\langle\sigma v\rangle' = 10^{-16}\,\mathrm{GeV}^{-2}$, $M_{X'} = 10$ GeV for IA_{nr}, and $\langle\sigma v\rangle' = 10^{-16}\,\mathrm{GeV}^{-2}$, $M_{X'} = 10^{-4}$ GeV for IA_{r}, with $B_{tot} = 0$ and $H_I = 10^{15}\Gamma_\phi$; all other parameters taken to their benchmark values (5.5).

modulus domination; thus taking $\widetilde{H} \approx {\Phi_I}^{1/2}$ we can use (5.17) to rewrite (5.47) as:

$$X'(T'_f) \approx \eta^3 \left[\frac{192}{(125\pi^7)^{1/2}}\right] \left[\frac{{g_\star}^{3/2}(T_{RH})}{{g'_\star}^{3}(T'_\star)}\right] \left[\frac{{T_{RH}}^7\, M_{\mathrm{pl}}\, \langle\sigma v\rangle'\ \Phi_I}{M_{X'}^{12}}\right] \int_{\frac{M_{X'}}{T'_{\max}}}^{\frac{M_{X'}}{T'_f}} dx'\, {x'}^{11}\, {n'_{\mathrm{eq}}}^{2}\,, \tag{5.48}$$

where we have defined $x' \equiv M_{X'}/T'$. Here T'_* is defined as the temperature at which the integrand of $\int dx' {x'}^{11} {n'_{eq}}^2$ is peaked, and T'_f is a temperature chosen such that $X'(T')$ is essentially constant for $T' < T'_f$. For relativistic X', the integrand of (5.47) peaks at $T' \approx T'_D/1.75$. Thus we will henceforth take $T'_f \approx T'_D/1.75$, though if $M_{X'} \gg T'_D$ the integrand of (5.47), (5.48) falls rapidly well before T'_f.

The evaluation of the integral in (5.48) is different in different regimes. If $M_{X'} > T'_D$, we can evaluate (5.48) assuming X' satisfies Maxwell-Boltzmann statistics. The integral in (5.48) can then be expressed as:

$$\int_{\frac{M_{X'}}{T'_{\max}}}^{\frac{M_{X'}}{T'_f}} dx' {x'}^{11} {n'_{\mathrm{eq}}}^{2} = \frac{{g'}^2 M_{X'}^6}{4\pi^4} \int_{\frac{M_{X'}}{T'_{\max}}}^{\frac{M_{X'}}{T'_f}} dx' {x'}^{9} K_2(x')^2\,. \tag{5.49}$$

The function ${x'}^9 K_2(x')^2$ peaks at $x'_\star \approx 3.6$, corresponding to $T'_* \approx 0.28\, M_{X'}$. Thus the maximum X' production takes place when X' is non-relativistic, justifying our assumption of Maxwell-Boltzmann statistics. Finally, if $\frac{M_{X'}}{T'_{\max}} > x'_\star$, then (5.49) will be exponentially suppressed, in particular by $\exp(-2M_{X'}/T'_{\max})$. We denote the above mechanism of DM production via non-relativistic inverse annihilations as $IA_{\rm nr}$. We remind the reader that for $M_{X'} > T_{D'}$, (5.48) is valid if $T'_{FO} > T'_{\max}$ or if $T'_{FO} > M_{X'}$ where T'_{FO} is given by (5.44); otherwise $\Omega_{\rm ann}h^2$ is determined by non-relativistic freeze-out during modulus domination as described in Section 5.2.4.1.

What happens when $M_{X'} < T'_D$? In this case, X' production peaks when X' is relativistic at $T'_* = T'_D/1.75$, and Fermi-Dirac or Bose-Einstein statistics must be taken into account. The integral in (5.49) can then be expressed as:

$$\int_{\frac{M_{X'}}{T'_{\max}}}^{\frac{M_{X'}}{T'_f}} dx' x'^{11} {n'_{\rm eq}}^2 = \frac{\zeta(3)^2 {c_\xi}^2 {M_{X'}}^6}{\pi^4} \int_{\frac{M_{X'}}{T'_{\max}}}^{\frac{M_{X'}}{T'_f}} dx' x'^5 \approx \frac{1.75^6\, \zeta(3)^2 {c_\xi}^2 {M_{X'}}^{12}}{6\pi^4 {T'_D}^6} \tag{5.50}$$

where again $c_\xi = g'\,(3g'/4)$ for bosons (fermions). We denote the above mechanism of DM production via relativistic inverse annihilations as $IA_{\rm r}$.

Given (5.30) and (5.48)-(5.50), the relic abundance from inverse annihilations can be readily computed:

$$\frac{\Omega_{\rm ann}\, h^2\; [IA_{\rm nr}]}{\Omega_R\, h^2} \approx \left[\frac{48\, g'^2\, \chi\, \eta^3}{125^{1/2}\pi^{15/2}\, L^{3/4}}\right] \left[\frac{{g_\star}^{3/2}(T_{RH})}{{g'_\star}^3(T'_\star)}\right] \left[\left(\frac{T_{RH}}{M_{X'}}\right)^7 \frac{M_{\rm pl} {M_{X'}}^2\, \langle\sigma v\rangle'}{T_{now}}\right] \tag{5.51}$$

$$\frac{\Omega_{\rm ann}\, h^2\; [IA_{\rm r}]}{\Omega_R\, h^2} \approx \left[\frac{32\, {c_\xi}^2\, \zeta(3)^2\, (1.75)^6}{125^{1/2}\pi^{15/2}\, L^{3/4}}\right] \left[\frac{\eta^{3/2}}{{g'_\star}^{3/2}(T'_D)}\right] \left[\left(\frac{T_{RH}}{M_{X'}}\right) \frac{M_{\rm pl} {M_{X'}}^2\, \langle\sigma v\rangle'}{T_{now}}\right] \tag{5.52}$$

where $\chi \equiv \int_{\frac{M_{X'}}{T'_{\max}}}^{\frac{M_{X'}}{T'_D}} dx' x'^9 K_2(x')^2$ and we have taken $g_*(T_D) = g_*(T_{RH})$ and $g'_*(T'_D) = g'_*(T'_f)$ in (5.52). Of all the production mechanisms we have studied, the only scenario where the X' relic abundance depends on T'_{max} is $IA_{\rm nr}$ in the case where $M_{X'} > T'_{max}$.

Note that we have assumed above that $\langle\sigma v\rangle'$ is independent of temperature. For the $QSE_{\rm nr}$, $FO^{\rm rad}_{\rm nr}$, $FO^{\rm mod}_{\rm nr}$ and $IA_{\rm nr}$, the processes which determine the DM relic abundance occur when X' is non-relativistic. Thus for these mechanisms, a temperature-independent $\langle\sigma v\rangle'$ is typically a good assumption for s-wave annihilation (p-wave annihilations are considered in Appendix F). However for $IA_{\rm r}$, the relevant process responsible for the DM abundance (inverse annihilation) takes place when X' is relativistic[8]. Since $IA_{\rm r}$ requires $\langle\sigma v\rangle' < \langle\sigma v\rangle'_c$, it is expected that $\langle\sigma v\rangle'$ in this case is schematically given by $\langle\sigma v\rangle' = \frac{T^n}{\Lambda^{n+2}}$ for some heavy mediator scale Λ and positive integer n. The temperature-independent $\langle\sigma v\rangle'$ case studied here corresponds to $n = 0$. Another well motivated case is $n = 2$,

---

[8] The process responsible for DM abundance for $FO^{\rm rad}_{\rm r}$ does take place when X' is relativistic, but in this case the DM abundance is independent of $\langle\sigma v\rangle'$, see (5.41).

corresponding to fermionic X' annihilating via a heavy bosonic mediator. We consider this possibility in Appendix F, and show that the $n = 2$ case can be recovered from (5.52) by making the replacement $\langle\sigma v\rangle' \to 0.17 \times {T'_D}^2/\Lambda^4$.

5.2.5 Summary of Results

	DM Production Mechanism	Parametric Region
I. Efficient Ann. at T'_D $\langle\sigma v\rangle' > \langle\sigma v\rangle'_c$	A. Non-Relativistic QSE $[QSE_{\rm nr}]$	$M_{X'} > \hat{x}'_F T'_D$
	B. FO During Radiation Domination $[FO^{\rm rad}_{\rm nr}$ & $FO^{\rm rad}_{\rm r}]$	$M_{X'} < \hat{x}'_F T'_D$
II. Inefficient Ann. at T'_D $\langle\sigma v\rangle' < \langle\sigma v\rangle'_c$	A. FO During Matter Domination + Modulus Decay $[FO^{\rm mod}_{\rm nr}]$	$\{T'_{\rm max}, M_{X'}\} > T'_{FO} > T'_D$ $\left[\langle\sigma v\rangle' > \langle\sigma v\rangle'_0\right]$
	B. Inverse Ann. ($R'R' \to X'X'$) + Modulus Decay $[IA_{\rm nr}$ & $IA_{\rm r}]$	IIA condition not satisfied $\left[\langle\sigma v\rangle' < \langle\sigma v\rangle'_0\right]$

Table 5.1: Summary of the different parametric regimes for $\Omega_{DM}h^2$ as discussed in Section 5.2.2. The quantity $\langle\sigma v\rangle'_c$ is defined in (5.35) and $\langle\sigma v\rangle'_0$ in (5.46). The temperatures $T'_{\rm max}$ is defined in (5.18), T'_D in (5.20), and T'_{FO} above (5.44).

In this section, we summarize the results of this section for the benefit of the reader. There are four qualitatively distinct parametric regimes for $\Omega_{DM}h^2$ in the framework considered. These different regimes are summarized in Table 5.1; $\langle\sigma v\rangle'$ is defined in (5.35), T'_D is defined in (5.20), and T_{max} is defined in (5.18). The quanitites $\hat{T}'_{FO}$ and T'_{FO} are respectively the X' freezeout temperatures during radiation domination (5.39) and modulus domination (5.44). Here we briefly review the parametrics for $\Omega_{DM}h^2$ in these different regimes, and collect the semi-analytic expressions for $\Omega_{DM}h^2$ derived earlier. In the following expressions we will set $g_*(T_{RH}) = g_*(T_D) = 10.75$, which is the SM value for $g_*(T)$ at $T \sim 10$ MeV. We also assume a fermionic DM candidate and set $g' = 2$. Note that the various mechanisms are valid in different parameteric regions; this is reflected in the different fiducial values for $M_{X'}$ and $\langle\sigma v\rangle'$ chosen in the expressions below. In Appendix E we compare our approximate expressions with numerical solutions to the Boltzmann equations (5.7) and find close agreement.

- **I.A: Non-Relativistic QSE (**$QSE_{\rm nr}$**):**
  DM annihilations are large enough to drive X' to its *quasi-static equilibrium* (QSE) value until T' is close to T'_D, soon after which QSE is lost and the comoving DM abundance becomes constant. The relic abundance in this regime is given by (5.38):

  $$\Omega\, h^2\,[QSE_{\rm nr}] \;\;\approx\;\; 5.2\times(1-\eta)^{-3/4}\left(\frac{\tilde{A}_c}{3}\right)\left(\frac{M_{X'}}{10\,{\rm GeV}}\right)\left(\frac{10\,{\rm MeV}}{T_{RH}}\right)\left(\frac{10^{-8}\,{\rm GeV}^{-2}}{\langle\sigma v\rangle'}\right)$$

  $\tilde{A}_c$ is defined below (5.37), and lies in the range : $1\lesssim\tilde{A}_c\lesssim 5$ for $\langle\sigma v\rangle'_c\lesssim\langle\sigma v\rangle'\lesssim 10^5\,\langle\sigma v\rangle'_c$. *$QSE_{\rm nr}$ is the precise generalization of the "non-thermal WIMP miracle" studied in [69, 98], and also captures the sub-dominant logarithmic dependence on $\langle\sigma v\rangle'$ and $\langle\sigma v\rangle'_c$ via $\tilde{A}_c$ which was not considered in [69, 98].*

- **I.B: Freeze-out during radiation domination (**$FO^{\rm rad}_{\rm nr}\,\&\,FO^{\rm rad}_{\rm r}$**):**
  X' tracks its equilibrium value until after $T'\approx T'_D$, and freezes-out *after* the modulus decays and the Universe becomes radiation dominated. Both non-relativistic ($FO^{\rm rad}_{\rm nr}$) and relativistic ($FO^{\rm rad}_{\rm r}$) thermal freezeout are possible. $FO^{\rm rad}_{\rm nr}$ is the dark sector analogue of standard WIMP freeze-out during radiation domination, while $FO^{\rm rad}_{\rm r}$ is the dark analogue of neutrino decoupling in the visible sector. This mechanism occurs only for $M_{X'}\lesssim T'_D$; see Table 5.1. The relic abundances are given by (5.40) and (5.41):

  $$\Omega\, h^2\;[FO^{\rm rad}_{\rm nr}] \;\;\approx\;\; 0.13\times\left(\frac{\eta}{(1-\eta)^3\,g_*(\hat{T}_F)g'_*(\hat{T}'_F)}\right)^{1/4}\left(\frac{\hat{x}'_F}{17.5}\right)\left(\frac{10^{-8}\,{\rm GeV}^{-2}}{\langle\sigma v\rangle'}\right)$$

  $$\Omega\, h^2\;[FO^{\rm rad}_{\rm r}] \;\;\approx\;\; 100\times\left(\frac{\eta^3}{(1-\eta)^3\,g_*(\hat{T}_F)g'_*(\hat{T}'_F)^3}\right)^{1/4}\left(\frac{M_{X'}}{1\,{\rm KeV}}\right)$$

  $\hat{x}'_F$ is defined in (5.39) and captures the standard logarithmic sensitivity to $\langle\sigma v\rangle'$ for thermal freezeout.

- **II.A: Freeze-out during modulus domination and production from modulus decay (**$FO^{\rm mod}_{\rm nr}$**):**
  X' reaches its equilibrium value and then freezes out during the modulus dominated

phase. After freeze-out, modulus decay continues to populate X' until $T \lesssim T_D$. As discussed in Section 5.2.4, non-relativistic freeze-out during modulus domination occurs only if $T'_{\rm max} > T'_{FO} > T'_D$ and $M_{X'} > T'_{FO}$. This implies $1 < x'_F < \frac{M_{X'}}{T'_D}$, and $\langle\sigma v\rangle'_0 < \langle\sigma v\rangle' < \langle\sigma v\rangle'_c$ where $\langle\sigma v\rangle'_0$ is given in (5.46). The relic abundance is given by $\Omega_{DM}\, h^2 = \Omega_{\rm decay}\, h^2 + \Omega_{\rm ann}\, h^2$ where $\Omega_{\rm decay}\, h^2$ and $\Omega_{\rm ann}\, h^2$ are given respectively by (5.43) and (5.45) :

$$\begin{aligned}\Omega_{\rm decay}\, h^2 &\approx& 0.31 \times \left(\frac{B_{tot}}{(1-\eta)^{3/4}}\right)\left(\frac{M_{X'}}{10\,\mathrm{MeV}}\right)\left(\frac{T_{RH}}{10\,\mathrm{MeV}}\right)\left(\frac{50\,\mathrm{TeV}}{m_\phi}\right) \\ \Omega_{\rm ann}\, h^2\; [FO^{\rm mod}_{\rm nr}] &\approx& \left(\frac{1.1\times 10^{-6}\,\eta}{g'_*(T'_{FO})\,(1-\eta)^{3/4}}\right)\left(\frac{x'_F}{19}\right)^4\left(\frac{T_{RH}}{10\,\mathrm{MeV}}\right)^3\left(\frac{10\,\mathrm{GeV}}{M_{X'}}\right)^3\left(\frac{10^{-8}\,\mathrm{GeV}^{-2}}{\langle\sigma v\rangle'}\right)\end{aligned}$$

x'_F is defined in (5.44) and is logarithmically sensitive to $\langle\sigma v\rangle'$.

- **II.B: Inverse annihilation and production from modulus decay** ($IA_{\rm nr}\,\&\,IA_{\rm r}$):
  X' does not undergo freezeout during modulus domination. DM production takes place predominantly by inverse annihilations as well as production from modulus decay. Specifically, $\Omega_{DM}\, h^2 = \Omega_{\rm decay}\, h^2 + \Omega_{\rm ann}\, h^2$ where $\Omega_{\rm decay}\, h^2$ is given above, while $\Omega_{\rm ann}\, h^2$ gets contributions from inverse annihilations. There are two different parametrics for $\Omega_{\rm ann}\, h^2$ depending on whether $M_{X'} > T'_D$ or vice versa.

  (i) $M_{X'} > T'_D$: The inverse annihilation contribution peaks at $T'_* \approx 0.28\, M_{X'}$ and:

$$\Omega_{\rm ann}\, h^2[IA_{\rm nr}] \approx \left(\frac{6.2\times 10^{-7}\,\eta^3}{(1-\eta)^{3/4} g'_*(T'_*)^3}\right)\left(\frac{\chi}{292}\right)\left(\frac{T_{RH}}{10\,\mathrm{MeV}}\right)^7\left(\frac{10\,\mathrm{GeV}}{M_{X'}}\right)^5\left(\frac{\langle\sigma v\rangle'}{10^{-16}\,\mathrm{GeV}^{-2}}\right)$$

  where χ is defined below (5.52). To a good approximation, $\chi \approx 292$ if $T'_{\rm max} > T'_* > T'_D$. On the other hand, if $T'_* > T'_{\rm max}$ ($M_{X'}$ is very large), χ will become suppressed by a factor of $\exp(-2M_{X'}/T'_{\rm max})$.

  ii) $M_{X'} < T_{D'}$: The inverse annihilation contribution peaks at $T'_* \approx T'_D/1.75$, and:

$$\Omega_{\rm ann}\, h^2\; [IA_{\rm r}] \approx 95\times\left(\frac{\eta^{3/2}}{(1-\eta)^{3/4} g'_*(T'_D)^{3/2}}\right)\left(\frac{T_{RH}}{10\,\mathrm{MeV}}\right)\left(\frac{M_{X'}}{1\,\mathrm{KeV}}\right)\left(\frac{\langle\sigma v\rangle'}{10^{-16}\,\mathrm{GeV}^{-2}}\right)$$

5.2.5.1 Reducing to a Single Sector

Though the results derived in this Section assume a two-sector cosmology as described in Section 5.1, it is straightforward to reduce these expressions to the single sector case. To see this, we define a temperature $T^0 \equiv T^0_{\rm max}\left(A^{-3/2} - A^{-4}\right)^{-1/4}$ where:

$$T^0_{\rm max} \equiv \left(\frac{3}{8}\right)^{2/5}\left(\frac{5}{\pi^3}\right)^{1/8}\left(\frac{g_*(T_{RH})^{1/2}}{g_*(T_{\rm max})}\right)^{1/4}(M_{\rm pl}H_I T_{RH}^2)^{1/4}\,. \tag{5.53}$$

T^0 corresponds to the temperature for a given value of A in single sector cosmologies (see eq. (15) in [105]). Reducing our expressions to the single sector case amounts to replacing both T and T' with T^0 in the above expressions for $\Omega_{DM}h^2$. Comparing (5.53) to (5.17)-(5.20), this amounts to making the replacements $(1-\eta) \to 1$ and $\eta/g'_*(T') \to 1/g_*(T)$ in the above expressions.

5.3 Implications for UV-motivated Supersymmetric Theories

In this section, we examine the implications of the results obtained in Section 5.2 for UV-motivated Supersymmetric theories that contain moduli fields, and identify regions of parameter space which yield suitable DM candidates. As discussed in Section 5.1 the DM relic abundance in these models is fixed by the following parameters:

$$T_{RH},\, m_\phi, B_{tot},\, \eta,\, g_*(T),\, g'_*(T'), M_{X'}, \langle\sigma v\rangle' \tag{5.54}$$

To simplify our analysis, we will henceforth assume that $g_*(T)$ and $g'_*(T')$ are constant, and take $g_*(T) = g'_*(T') = 10.75$. We also fix $\eta = 0.1$, which is a reasonable value assuming the modulus couplings are not sequestered from the dark sector[9]. Relaxing these assumptions will change the computed relic abundance as per the formulae in Section 5.2.2, but will not qualitatively effect the results presented here.

As mentioned in Section 5.1, the parameters T_{RH}, m_ϕ and B_{tot} can be viewed as inputs from the UV theory, and are fixed by the couplings and masses of the moduli fields. For a particular UV framework, these quantities are constrained to lie within a particular range of values. We will focus here on UV completions which contain gravitationally coupled moduli fields while also yielding TeV scale Supersymmetry. If the modulus interacts gravitationally, dimensional analysis suggests that $\Gamma_\phi = c_1 {m_\phi}^3/M_{pl}^2$, and T_{RH} as defined in

---

[9] For this value of η, the latest CMB bound on N_{eff} requires that all dark radiation particles have masses greater than ~ 1 eV. Otherwise, η must be smaller. The qualitative features of our results will be the same for smaller η as well.

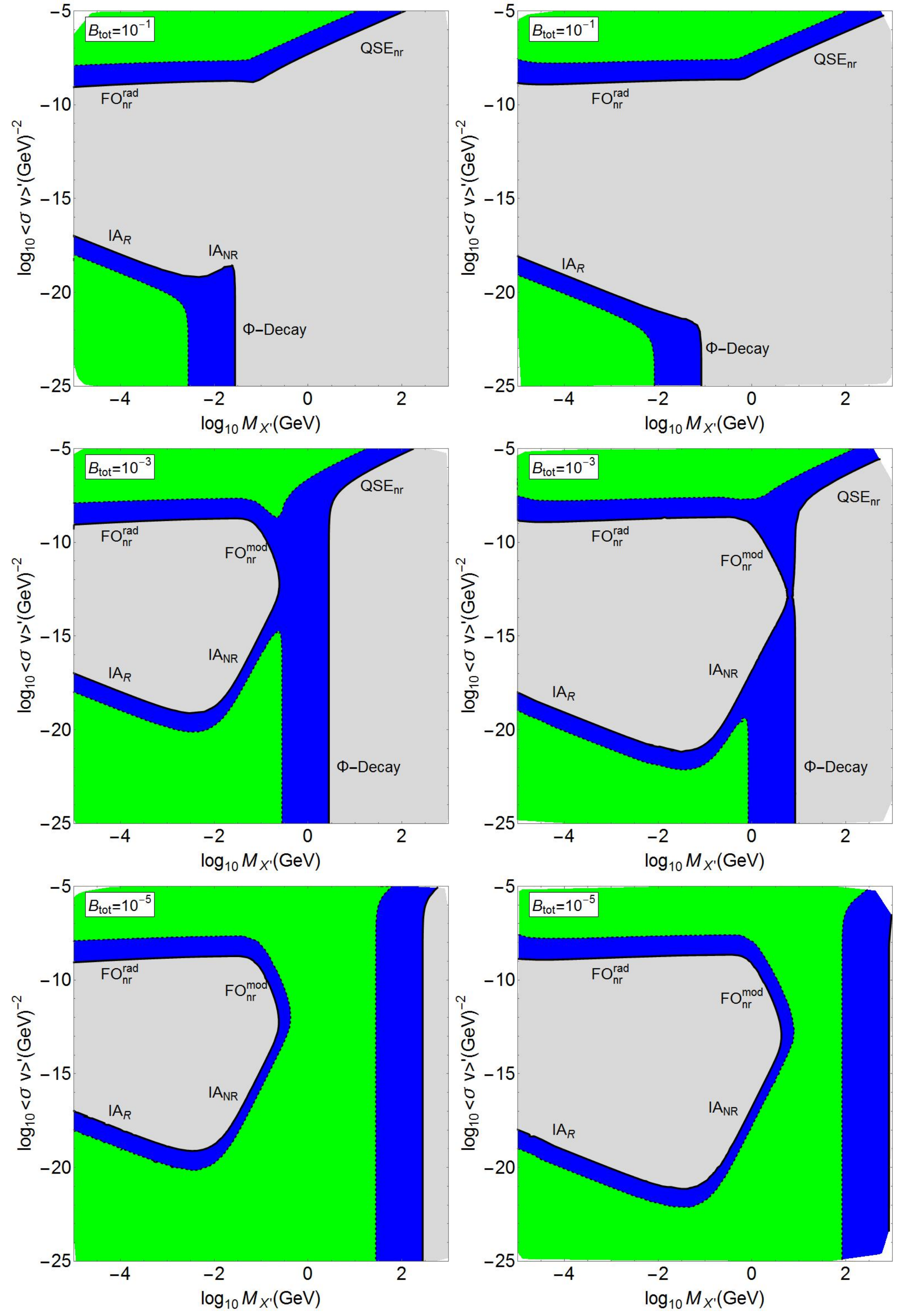

Figure 5.6: Left column: scan of the $\langle \sigma v \rangle'$, $M_{X'}$ parameter space with $T_{RH} = 10$ MeV, $m_\phi = 50$ TeV, and various values of B_{tot}. Right column: similar plots with $T_{RH} = 100$ MeV, $m_\phi = 150$ TeV. All other parameters are fixed to the benchmark values (5.5). Solid (dashed) contours correspond to $\Omega_{DM} h^2 = 0.12\,(0.012)$. Green, blue and gray regions represent $\Omega_{DM} h^2 < 0.012$, $0.012 < \Omega_{DM} h^2 < 0.12$ and $0.12 < \Omega_{DM} h^2$.

(5.3) is related to the modulus mass via:

$$T_{RH} \approx 14\,\mathrm{MeV} \times \left(\frac{m_\phi}{50\,\mathrm{TeV}}\right)^{3/2} {c_1}^{1/2} \tag{5.55}$$

Thus the BBN bound $T_{RH} \gtrsim$ MeV places a lower bound on m_ϕ in the tens of TeV range.

The range of values for m_ϕ is further restricted by imposing the requirement of TeV scale Supersymmetry. We focus here on models in which SUSY breaking is mediated to the visible sector via gravitational interactions; this arises naturally in theories containing moduli. In the minimal case (i.e. no sequestering or large volume suppression of SUSY breaking), the lightest modulus mass is order the gravitino mass $m_{3/2}$, which sets the scale of the SUSY breaking parameters [33, 65, 99, 100]. For many such models, the scalar superpartner masses will be comparable to $m_{3/2}$, while the gauginos may be parametrically lighter by roughly a loop factor. The lightest superpartners in the visible sector will then be gauginos whose masses are suppressed with respect to $m_{3/2}$. This is true for Type II and heterotic models with KKLT-type moduli stabilization, M-theory compactifications with stabilized moduli, and also for spectra with pure anomaly mediation. Thus for these SUSY models, the requirement of TeV scale Supersymmetry along with constraints from BBN imply:

$$30\,\mathrm{TeV} \lesssim m_\phi \lesssim \mathcal{O}(100)\,\mathrm{TeV}, \quad 5\,\mathrm{MeV} \lesssim T_{RH} \lesssim \mathcal{O}(100)\,\mathrm{MeV}, \tag{5.56}$$

assuming $c_1 \sim \mathcal{O}(1)$. This justifies our choice of benchmark parameters in (5.5). If the DM is an MSSM particle there is a tension between (5.56) and indirect detection constraints, which require $T_{RH} \gtrsim 1$ GeV [59, 101].

The quantity B_{tot} is more difficult to constrain from a theoretical point of view, as it depends on the precise interactions between the modulus and visible/dark sector particles. Nevertheless, if the canonically normalized lightest modulus contains a non-trivial fraction of the modulus that determines the gauge coupling of the visible and/or dark sector, then one expects a contribution to B_{tot} by operators of the form $\int d^2\theta\, \Phi\, W_\alpha\, W^\alpha$ where W_α is the chiral gauge superfield of either the visible or dark sector[10]. Therefore, in M-theory compactifications [56] and also roughly isotropic Type II compactifications, B_{tot} is expected to be $\mathcal{O}(0.1)$. However, in anisotropic compactifications in which the visible and dark sectors are localized at different regions of the internal manifold, it is possible that B_{tot} is suppressed, see [108, 109] for example. We will consider below a wide range of values for B_{tot} to perform as general an analysis as possible.

In the following, we fix T_{RH}, m_ϕ and B_{tot} to particular values, and scan over $\langle \sigma v \rangle'$

---

[10] This allows the lightest modulus to decay to visible or dark sector gauginos, which would then cascade decay to the DM X'.

and $M_{X'}$ to give a fairly model-independent characterization of the viable regions of DM parameter space. All other parameters are taken to their benchmark values (5.5). In Figure 5.6, we have scanned over the $\langle \sigma v \rangle'$, $M_{X'}$ parameter space for various values of B_{tot}, with $T_{RH} = 10$ MeV, $m_\phi = 50$ TeV for the left column and $T_{RH} = 100$ MeV, $m_\phi = 150$ TeV for the right column (consistent with the $T_{RH} \propto {m_\phi}^{3/2}$ scaling manifest in (5.55)).

B_{tot} determines both the cross section required for QSE_{nr} (see (5.35)), and the size of the modulus decay contribution (5.43) in the inefficient annihilation region. Thus the available parameter regions are quite sensitive to orders of magnitude changes in B_{tot}. For $B_{tot} = 0.1$, the viable parameter space effectively splits into two regions. In the upper region $\langle \sigma v \rangle' \gtrsim 10^{-9}\,\mathrm{GeV}^{-2}$, the relic DM abundance is produced via either QSE_{nr} or FO_{nr}^{rad}, while in the lower region $\langle \sigma v \rangle' \lesssim 10^{-17}$ and the relic DM abundance is populated via inverse annihilations and/or modulus decay. In the inefficient annihilation regime, most of the parameter space with $M_{X'} > T_{RH}$ results in an overabundance of DM due to the modulus decay contribution for $B_{tot} = 0.1$ (see (5.43)). The value of $M_{X'}$ where the modulus decay contribution (5.43) saturates $\Omega_{DM} h^2 = 0.12$ scales like ${B_{tot}}^{-1}$; thus for smaller values of B_{tot}, much more of the $M_{X'} > T_{RH}$ parameter space becomes available. Particularly, for $B_{tot} \lesssim 10^{-3}$ both the FO_{nr}^{mod} and IA_{nr} mechanisms can give the correct relic abundance for a significant portion of the parameter space. These mechanisms are absent for $B_{tot} = 0.1$, as the DM masses required would result in too large a contribution from modulus decay.

5.4 Experimental/Observational Consequences

In this section, we discuss potential experimental probes of the framework analyzed above. As one can imagine, since our analysis covers a large range of values for the mass and couplings of DM in $M_{X'}$ and $\langle \sigma v \rangle'$, there are variety of interesting possibilities for observations. A detailed analysis of the various experimental signatures which can arise in this framework is beyond the scope of this chapter. Instead, we will limit ourselves here to making some general and preliminary remarks which will be relevant for future studies.

A nice schematic illustration of the framework studied here is provided in Figure 5.1. From there we see that there are three different kinds of couplings, denoted as: $\{\lambda_{V-V},\ \lambda_{V-D}$ and $\lambda_{D-D}\}$. Now, the very assumption that the visible and dark sectors are 'separate' sectors implies that the "portal" couplings of type λ_{V-D} are parametrically smaller than the $\{\lambda_{V-V}, \lambda_{D-D}\}$ couplings. When this is true, $\langle \sigma v \rangle$ dominantly depends on λ_{V-V}, while $\langle \sigma v \rangle'$ depends mostly on λ_{D-D}. *However, within this framework, it is the portal couplings of type λ_{V-D} that determine the signals for all "standard" searches for dark matter, such as* *direct-detection, indirect-detection, and collider experiments*. The portal couplings λ_{V-D} can cover a huge range. At one extreme, it is possible to have $\lambda_{V-D} \simeq \lambda_{grav}$, the latter corresponding to gravitational strength couplings suppressed by the Planck scale. In this case, the decay width of the LOSP X, Γ_X, is comparable to that of the modulus Γ_ϕ [11]. In our work, we have *not* focused on this case for both theoretical and experimental reasons, see Appendix D. At the other extreme, it is possible that λ_{V-D} is large enough so that the two sectors are in thermal equilibrium with each other and thus combine to form one sector. As mentioned above, we have also not focused on such a regime.

Nevertheless, the models considered here can still accommodate a huge range of values $1 \gg \lambda_{V-D} > \lambda_{grav}$ for the portal coupling λ_{V-D}, which in turn allows for a wide variety of DM signals (or lack thereof) in direct detection, indirect detection and collider searches. For this range of portal couplings, our results from Section 5.2.2 show that the relic abundance for the dark matter X' does not depend on the properties of the LOSP X – $\{M_X, \Gamma_X, \langle\sigma v\rangle\}$, or equivalently the portal couplings λ_{V-D}. Thus, in order to characterize the "standard" DM signals which arise in this framework, one must consider explicit dark sector models in which the size of the portal couplings λ_{V-D} are calculable. We save this exercise for future work, except for making some comments about the consequences of a decaying LOSP.

The LOSP X, being a visible sector particle, can be produced at colliders. Since it is unstable, it is possible that the LOSP is charged and/or colored. Prospects for detecting a charged/colored LOSP at the LHC are much better than that for a neutral LOSP, as a charged/colored LOSP will interact with detector materials and slow down considerably relative to a neutral LOSP. Charged/colored LOSP decay widths in the range: $10^{-13}\,\mathrm{GeV} \gtrsim \Gamma_X \gtrsim 10^{-31}\,\mathrm{GeV}$ can be measured in principle. However, subject to model-dependent details, large windows in the above range are now disfavored [110]. On the other hand, only decay widths larger than around 10^{-17} GeV ($\tau_X \lesssim 10^{-9}$ s) can be measured for a neutral LOSP because then a sizable fraction of LOSP particles decay inside the detector. The LOSP decay width Γ_X can be parameterized as:

$$\Gamma_X \sim \frac{\lambda_{V-D}^2}{16\pi} M_X. \tag{5.57}$$

Thus, one requires $\lambda_{V-D} \gtrsim 10^{-9}$ in order for a weak scale neutral LOSP to significantly decay inside the detector so that its decay products could be measured in principle. Otherwise the neutral LOSP is stable for collider purposes, and manifests itself as missing energy.

---

[11] This is because the modulus also couples with gravitational strength to both the visible and dark sectors

We now describe some possible signatures of the framework that do not depend on portal couplings between the visible and dark sectors.

5.4.1 Cosmological/Astrophysical Effects

Here, we comment on astrophysical and cosmological effects arising from two sources – i) that from DM couplings of type λ_{D-D}, i.e. from interactions within the dark sector, and ii) from the presence of a modulus-dominated phase in the early Universe. *Since these effects are independent of λ_{V-D} couplings, the observables which arise are independent of the pattern of "standard" signals for DM*. As such, they provide additional observables to probe DM and its properties. Some interesting examples of such effects include:

- Observables sensitive to power spectrum of density fluctuations of dark matter.
- Observables sensitive to the morphology of galactic DM halos.

Understanding these and other observables is becoming increasingly important, both because of the realization that interactions in dark sector can affect these observables, as well as from the fact that the quantity and quality of cosmological and astrophysical data has been getting steadily better. Here, we briefly discuss the following issues:

- *Sensitivity to Modulus-Dominated Era*:
  The presence of a modulus-dominated era in the early Universe can have important implications. As pointed out in [102, 111], this can lead to substantial linear growth of sub-horizon DM perturbations during the modulus-dominated era. More precisely, the presence of a (low) reheat temperature sets a new cosmological length scale, $L_{RH} \equiv (a_{RH}\,H_{RH})^{-1}$, the comoving horizon at the time of reheating. Therefore, *in the absence of other effects*, DM perturbations on length scales $l < L_{RH}$ grow linearly during the modulus dominated phase, and could have interesting observable effects. However, presence of other relevant scales can affect whether such sub-horizon growth of DM perturbations are observable or not. These scales are described below.

- *Damping of DM Perturbations due to Acoustic Oscillations $\&$ Free-Streaming*:
  It is well known that *chemical* equilibrium is in general different from *kinetic* equilibrium. In the context of DM interactions, the former is set by *number-changing* interactions in which DM number is not preserved, while the latter is set by *number-preserving* interactions in which DM number is conserved. For example, within the

standard WIMP paradigm, chemical decoupling leaving to thermal freezeout happens much earlier than kinetic decoupling since the interaction rate for the latter is enhanced by the relativistic abundance of light SM species in interactions of the type: $DM + SM \to DM + SM$.

There are two important scales related to kinetic decoupling that determine the length scale at which DM perturbations get damped or suppressed:

i) Scale arising due to the coupling of DM to the dark radiation fluid (and also to the visible radiation and baryons in general). The effect of coupling of DM to *visible* baryons and radiation is also present for standard WIMPs in general [112], but qualitatively different effects may arise here due to the presence of dark radiation (DR) in addition [113, 114]. It is expected that the DM-DR interactions will give rise to damped oscillatory features in the DM power spectrum with a characteristic length scale denoted as L_d, given by.

$$L_d = \frac{\eta_{kd}}{x_d}, \tag{5.58}$$

where η_{kd} is the conformal time at kinetic decoupling, and x_d is a numerical factor of $\mathcal{O}(1)$ (we take $x_d \approx 7$, see [112, 113] for example).

ii) Scale arising due to the free-streaming of particles after kinetic decoupling. This length scale is defined as $L_{fs} \equiv \int_{t_*}^{t_0} v/a\, dt$, where v is the average DM velocity, a is the scale factor, t_0 is the current age of the Universe, and t_* is a characteristic time which is different for different mechanisms and will be discussed shortly. If the universe is radiation dominated at t_*, then L_{fs} is given by (see e.g. [111]):

$$L_{fs}^{rad} \approx \frac{1}{H_0\sqrt{\Omega_R}} \int_{a_*}^{1} \left[\left(1 + \left(\frac{M_{X'} a}{p_* a_*} \right)^2 \right) \left(1 + \frac{a}{a_{eq}} \right) \right]^{-1/2} da \tag{5.59}$$

where $a_{eq} \approx 2.9 \times 10^{-4}$ and $H_0 \approx 1.5 \times 10^{-42}$ GeV. If the universe is modulus dominated at t_*, L_{fs} is instead given by:

$$L_{fs}^{mod} \approx \frac{a_{RH}^{1/2}}{H_0\sqrt{\Omega_R}} \int_{a_*}^{a_{RH}} a^{-1/2} \left(1 + \left(\frac{M_{X'} a}{p_* a_*} \right)^2 \right)^{-1/2} da + L_{fs}^{rad}\Big(a_* \to a_{RH},\, p_* \to p_{rh} \Big) \tag{5.60}$$

where we have taken $H = H_{RH} \left(a_{RH}/a \right)^{3/2}$ during modulus domination. Here a_{RH} corresponds to the scale factor at which $H = \Gamma_\phi$, normalized such that $a = 1$ today.

Both scales above are present in general, and the damping scale is determined by $L_{cut} = \mathbf{max}(L_d, L_{fs})$. The scale L_{cut} is relevant in determining the mass of the smallest DM proto-halos: $M_{proto} \propto L_{cut}^3$.

As discussed above, DM perturbations on length scales l such that $L_{cut} < l < L_{RH}$ grow linearly during modulus domination *and* the growth during this era is *not* washed out by free-streaming and/or acoustic damping effects. Thus, these perturbations could have interesting and novel effects. For example, as pointed out in [102], a low reheat temperature of order 10 MeV or so can give rise to an abundance of earth-mass dark matter microhalos in the early Universe containing a significant fraction of dark matter. A possible way to observe these microhalos is via their strong gravitational lensing effects on quasars [115, 116], or via their impact on pulse arrival times from millisecond pulsars [117]. Furthermore, if the portal couplings λ_{V-D} are large enough, these DM microhalos can annihilate to γ-rays, thereby acting as γ-ray point sources and contributing to the γ-ray background [118, 119, 120]. It is worthwhile to explore these possibilities in more detail.

In the case where $L_{cut} > L_{RH}$ such that the growth of DM perturbations during modulus domination is washed out, the damping of DM perturbations below the scale L_{cut} can still give rise to observable effects. Notably, "warm" dark matter with $L_{cut} = L_{fs} \sim 1-100$ Kpc can reconcile many of the discrepancies between ΛCDM cosmology and observations on galactic/sub-galactic scales [121, 122, 123]. If the damping scale becomes too large i.e. $L_{cut} \gtrsim 1$ Mpc, bounds from Lyman-α will start to apply [124].

5.4.2 Prospects for the Framework

What can be said about the effects mentioned above *vis-a-vis* the framework considered? Qualitatively, there are two different scenarios which are determined by whether or not T'_{kd} is larger than T'_D. If $T'_{kd} < T'_D$, then X' kinetically decouples during radiation domination after the modulus has decayed. Depending on the mass and kinetic decoupling temperature, either L_{fs} or L_d will determine the damping scale L_{cut}. Alternatively, if $T'_{kd} > T'_D$ then the DM kinetically decouples during the modulus dominated phase; L_{fs} will then determine L_{cut} for most of the relevant parameter space.

In order to discuss observational signatures for the framework considered here, it is pertinent to consider what range of values for T'_{kd} is expected, given the DM production mechanisms discussed in Section 5.2.2. Generically, one expects that crossing symmetry relates the $X'X' \to R'R'$ annihilation cross section ($\langle\sigma v\rangle'$) to the ($X'R' \to X'R'$) elastic scattering cross section (σ'_{el}). In the case of fermionic DM annihilating into fermionic R' through a massive bosonic mediator, $\langle\sigma v\rangle' \sim ({M_{X'}}^2 + T'^2)/\Lambda^4$ and $\sigma'_{el} \sim T'^2/\Lambda^4$ where Λ

is the mediator mass scale (see e.g.[125, 126]). If this is the only $X' - R'$ scattering process, X' kinetically decouples when the scattering rate $\Gamma_{el} \sim \sigma'_{el} n'_{eq}\, \omega$ drops below the Hubble rate, where $\omega = 1$ $(T'/M_{X'})$ for relativistic (non-relativistic) X'. Taking the benchmark parameters (5.5) for this example, $T'_{kd} < T'_D$ implies $\Lambda \lesssim 800$ GeV $(250 {M_{X'}}^{-1/4}$ GeV) if X' kinetically decouples while relativistic (non-relativistic).

However, in a more realistic model there may be other (e.g. inelastic) processes which also keep X' in kinetic equilibrium; thus the precise relationship between $\langle \sigma v \rangle'$ and T'_{kd} is fairly model-dependent. In the following, we will treat T'_{kd} as a free parameter, though it will be useful to keep the above toy example in mind as a benchmark scenario.

Kinetic Decoupling During Radiation Domination: In this case, the DM particle X' is in kinetic equilibrium until $T' < T'_D$. The kinetic decoupling temperature will then determine the length scales L_d in (5.58) and L_{fs} in (5.59). Specifically, L_{fs} is computed using (5.59) with $T'(t_*) = T'_{kd}$ and $p_* = \sqrt{3} T'_{kd}\, \omega^{1/2}$ where $\omega = 1\, (M_{X'}/T'_{kd})$ for $M_{X'} < T'_{kd}$ $(M_{X'} > T'_{kd})$. From Figure 5.7, we see that for larger DM masses 10^{-2} GeV $\lesssim M_{X'} \lesssim 10^{2}$ GeV and smaller kinetic decoupling temperatures $T'_{KD} < 0.1\, T'_D$, L_D is larger than L_{fs} and determines L_{cut} and the mass of the smallest proto-halos. All of this parameter space is consistent with the upper bounds arising from the observables studied in [114]. In the complementary parameter space, L_{cut} is determined by L_{fs}. A large region of this parameter space is consistent with the Lyman-α forest upper bound on L_{fs} of about 1 Mpc. Finally, for most of the parameter space $L_{cut} = \mathbf{max}(L_d, L_{fs})$ is greater than L_{rh}, implying that growth of DM perturbations in the modulus-dominated era is washed out. Only in a very small region of parameter space with $1 \lesssim M_{X'} \lesssim 100$ GeV and $0.1\, T'_D \lesssim T'_{KD} \lesssim T'_D$, one has $L_{cut} < L_{RH}$ so that the memory of growth of DM perturbations on length scales l with $L_{cut} < l < L_{RH}$, is retained. This can have interesting implications as mentioned previously.

Kinetic Decoupling During Modulus Domination: In this case, X' kinetically decouples before the beginning of radiation domination such that $T'_{kd} > T'_d$. If kinetic decoupling occurs *after* X' production, L_{fs} is given by (5.60) with $T'(t_*) = T'_{kd}$ and $p_* = \sqrt{3} T'_{kd}\, \omega^{1/2}$. Note that this scenario requires $M_{X'} > T'_D$, as for $M_{X'} < T'_D$ DM production occurs predominantly when $T' \lesssim T'_D$ (see Section 5.2.5). For the allowed parameter regions depicted in Figure 5.6, one finds in this case that $L_d < L_{RH} < L_{fs} \ll 1$ Mpc, assuming a single DM particle accounts for all of the dark matter.

If kinetic decoupling occurs *before* X' production, $T'(a_*)$ is the characteristic temperature at which X' production occurs, and p_* depends on the mechanism for X' production. The production mechanisms which allow for X' to be produced out of kinetic equilibrium are (see Section 5.2.2):

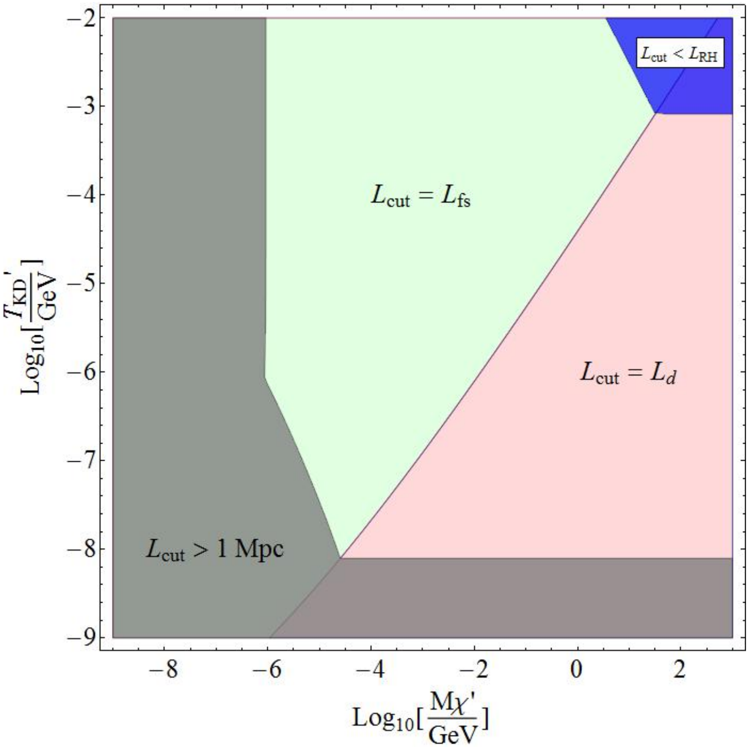

Figure 5.7: Hierarchies among the cosmological length scales L_{fs}, L_d, L_{RH} shown in the $M_{X'} - T'_{KD}$ plane, assuming $T'_{kd} < T'_D$. The pink region corresponds to $L_d > L_{fs}$, the green region corresponds to $L_{fs} > L_d$, the blue region corresponds to $L_{RH} > L_{cut}$, and the brown region corresponds to $L_{cut} > 1$ Mpc. The other relevant parameters are set to their benchmark values, see (5.5).

- *Inverse annihilation*: As discussed in Section 5.2.4.2, DM production from inverse annihilations peaks at $T'_* \approx T'_D/1.75$ for IA_r and $T'_* \approx 0.28 M_{X'}$ for IA_{nr}. We then take $p_* \approx \sqrt{3} T'_*$ in computing L_{fs}.
- *Production from Modulus Decay*: If the DM abundance comes predominantly from modulus decay (i.e. $\Omega_{DM} h^2 \approx \Omega_{decay} h^2$ (5.43)), then $T'_* \approx T'_D$ and $p_* \approx m_\phi/2$ assuming 2-body modulus decays.

To be precise, if X' kinetically decouples before X' production occurs, one must replace X' in the Boltzmann equations with an integral over the X' phase space distribution function. However for the inverse annihilation and modulus decay production mechanisms, terms involving X' can be neglected in the X' Boltzmann equation; thus the results in Section 5.2.4 are still valid despite this departure from kinetic equilibrium[12] Nonetheless, in order to properly compute p_* and L_{fs}, a precise knowledge of the DM phase space distribution

---

[12] One additional subtlety is that if X' is out of kinetic equilibrium, we are no longer justified in assuming $E_{X'} \approx \sqrt{3T'^2 + M_{X'}{}^2}$ in (5.7). However if $B_{X'} \lesssim 0.1$, this subtlety will not significantly effect our results.

function at T'_* is required. In lieu of a more precise computation we will use the approximate values for p_* quoted above, with the understanding that our results for L_{fs} are meant to be qualitative.

Figure 5.8 summarizes the cosmological length scales which can arise in the case where X' is produced out of kinetic equilibrium. Because X' is not coupled to the dark radiation bath when produced, there is no acoustic damping effect to consider; thus $L_{cut} = L_{fs}$. We see from Figure 5.8 that for the IA_r case, most of the parameter space easily avoids Lyman-α constraints. The IA_r scenario can also naturally accomodate warm DM candidates, with $L_{fs} \sim 1 - 100$ kpc. Perhaps more interestingly, we see that for a majority of the IA_{nr} parameter space, $L_{fs} < L_{RH}$. Thus, the linear growth of DM perturbations during modulus domination is *not* washed out for a large portion of the IA_{nr} parameter space, leading to potentially interesting effects as discussed above.

Finally, let us comment on the case where relic DM is produced from modulus decay. If DM particles in this scenario are kinetically decoupled at T'_D, they will be highly boosted when produced from modulus decay. If the modulus decay contribution is the dominant contribution to the overall DM abundance, DM masses within the range 10^{-3} GeV $\lesssim M_{X'} \lesssim$ few GeV are at odds with Lyman-α bounds $L_{fs} \lesssim 1$ Mpc; this is evident from Figure 5.8. Thus if the relic DM is predominantly produced via modulus decays, Lyman-α constraints require $M_{X'} \gtrsim \mathcal{O}(1)$ GeV; this in turn implies $B_{tot} \lesssim 10^{-3}$ as can be seen from (5.43).

To summarize, we find that there are various interesting possibilities for cosmological/astrophysical observables which can probe the framework considered, both in terms of providing constraints on the parameter space as well as by providing insights for potential signals. *In particular, we find that there is sensitivity to the modulus domination era for a large portion of the IA_{nr} parameter space.* This is in contrast to the result obtained in [111], primarily because the framework considered here encompasses a wider variety of DM masses and couplings compared to the analysis in [111, 127]. The results obtained in this section are largely qualitative. It would therefore be interesting to carry out a more detailed and comprehensive analysis of the constraints and potential observations which have been suggested in this section.

5.5 Summary and Future Directions

In this work, we have provided a general classification of dark matter models in a Universe which undergoes a phase of pressure-less matter (modulus) domination. Such non-thermal cosmological histories are predicted in a wide class of UV completions to the Standard

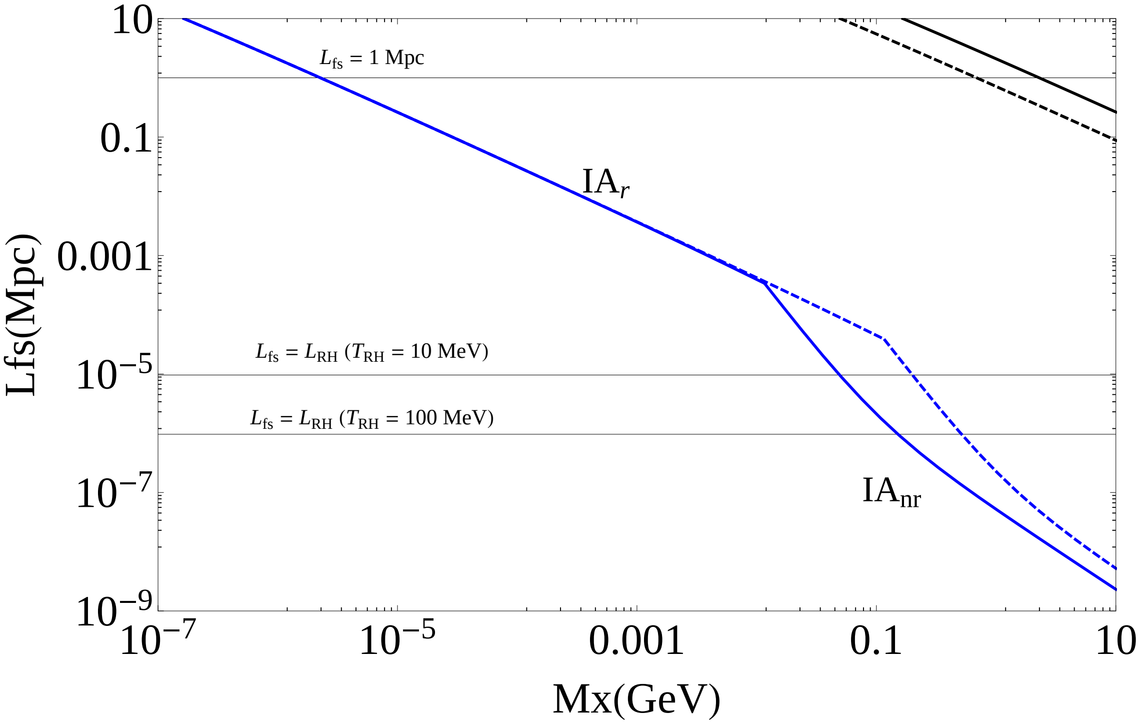

Figure 5.8: Plot of the free-streaming length L_{fs} in Mpc. The blue lines correspond to DM produced predominantly via inverse annihilations, while the black lines correspond to DM produced predominantly via modulus decay. The solid lines were obtained for $T_{RH} = 10$ MeV, $m_\phi = 50$ TeV while the dashed lines were obtained for $T_{RH} = 100$ MeV, $m_\phi = 150$ TeV. The other relevant parameters are chosen as in (5.5).

Model (e.g. compactified string theories), and are also phenomenologically viable provided that the matter dominated phase ends before BBN. Our analysis generalizes previous works by going far beyond the standard WIMP paradigm. In particular:

- We consider DM masses and annihilation cross sections which span several orders of magnitude above and below the electroweak scale.
- We allow the possibility that DM in thermal equilibrium with a 'dark sector', whose temperature need not be the same as that of the visible sector.

Upon analyzing the relevant Boltzmann equations, we classify the mechanisms by which relic DM can be produced. We find four distinct mechanisms ($QSE_{\rm nr}$, $FO^{\rm mod}_{\rm nr}$, $IA_{\{\rm r,nr\}}$ and $FO^{\rm rad}_{\{\rm r,nr\}}$), each of which have different parametrics for $\Omega_{DM}h^2$. *The first three mechanisms are different from standard thermal freeze-out*. We derive semi-analytic approximations for these various production mechanisms, and discuss their regimes of validity. For the convenience of the reader, these results are summarized in Section 5.2.5.

Our results have interesting implications for Supersymmetric theories containing moduli fields such as the compactified string theories which have been central to this thesis. As discussed in Sections 5.1 and 5.2, $\Omega_{DM}h^2$ does not depend on the masses or couplings of the (unstable) lightest visible sector superpartner (LOSP), provided the LOSP decays before the end of modulus domination[13]. Once the modulus mass and couplings are fixed and the dark relativistic degrees of freedom $g'_*(T')$ are specified, $\Omega_{DM}h^2$ depends only on $M_{X'}$ and $\langle\sigma v\rangle'$. In Section 5.3, we fixed the modulus mass and couplings by considering models with gravity mediated SUSY breaking in which m_ϕ is of order the gravitino mass. We mapped out the parameter space of these models by scanning over $M_{X'}$, $\langle\sigma v\rangle'$ for various values of B_{tot}, see Figure 5.6. Here B_{tot} is the branching ratio of the modulus decay into DM, including contributions from intermediate states. For $B_{tot} \sim \mathcal{O}(0.1)$, the viable DM parameter space splits into two seperate regions: large annihilation cross section $\langle\sigma v\rangle' \gtrsim 10^{-9}$ GeV^{-2}, or small annihilation cross section $\langle\sigma v\rangle' \lesssim 10^{-17}$ GeV^{-2}. Intermediate values of $\langle\sigma v\rangle'$ result in DM overproduction. Moreover in the $\langle\sigma v\rangle' \lesssim 10^{-17}$ GeV^{-2} region, the DM mass must be $\lesssim 100$ MeV to avoid being overproduced by moduli decay. If however the modulus branching ratio to DM is suppressed i.e. $B_{tot} \ll 1$, much more of the DM parameter space becomes available. These features can easily be inferred from Figure 5.6.

We have also briefly discussed potential experimental signatures for the theoretical framework considered here. Since $\Omega_{DM}h^2$ is insensitive to the portal couplings between the visible and dark sectors for the models considered, the "standard" DM signals in direct detection, indirect detection and collider experiments, which crucially depend on portal couplings between the visible and dark sectors, can cover a wide range of possibilities are rather model-dependent. On the other hand, observables which involve couplings within the dark sector yield more robust predictions, as these couplings are correlated with the DM relic abundance. One such set of observables involves the power spectrum of DM density perturbations. If the DM kinetically decouples during the radiation dominated era after BBN, the sensitivity of DM density perturbations to the modulus dominated phase is maintained only for a very small region of parameter space, as shown in Figure 5.7. On the other hand, when DM kinetically decouples during modulus domination, the power spectrum of DM density perturbations depends on the mechanism by which relic DM is produced:

- If DM is produced by annihilation of thermal bath particles while the DM is non-relativistic (we call this case $IA_{\rm nr}$, see Section 5.2.5), the free-streaming length is smaller than the comoving horizon at T_{RH}. The linear growth of DM density pertur-

---

[13] The contrary case is briefly considered in Appendix D.

bations during modulus domination is *not* washed out, leading to potentially interesting astrophysical signatures as discussed in [102].

- If DM is produced by annihilation of thermal bath particles while the DM is relativistic (we call this case $IA_{\rm r}$, see Section 5.2.5), the free-streaming length is larger than the comoving horizon at T_{RH}. Even though the growth of DM perturbations during modulus domination is erased, a large region of parameter space yields $L_{\rm fs} \sim 1-100$ Kpc which leads to signatures similar to warm DM.
- If DM is dominantly produced by modulus decay, then the DM has large free streaming lengths $L_{\rm fs} \gtrsim 1$ Mpc, which is in tension with constraints on warm dark matter from Lyman-α measurements.

There are many opportunities for future research. From the point of view of the Boltzmann equations, including $n \to 2$ annihilation processes where $n \geq 3$ would be worth understanding in this framework (this would be the non-thermal analog of [128]). From the point of view of model-building, it would be worthwhile to study explicit models of DM candidates and portal interactions within the general framework so that detailed predictions for “standard” DM signals (e.g. direct and indirect detection) could be made. Finally, our discussion in Section 5.4 of the astrophysical/cosmological effects of DM interactions within its own sector has been largely qualitative. A more precise analysis would involve solving for the DM phase space distribution at kinetic decoupling in order to determine the appropriate transfer function relevant for the power spectrum of DM density fluctuations. We hope that future studies in these directions will help shed important light on the nature of dark matter.

CHAPTER 6

Conclusion

The field of theoretical particle physics has always pursued a theory which unifies all known fundamental interactions (SM + gravity). In this thesis we have studied the possibility that string theory provides a unified, UV complete theory of quantum gravity. In particular we have focused on identifying testable experimental signatures predicted by realistic string theories. This branch of particle physics is known as "string phenomenology". An interesting aspect of string phenomenology is that string theory predicts 10/11 spacetime dimensions. Thus in order for a string theory to plausibly describe our world, these additional spacetime dimensions must be compactified to reproduce an effective 4-dimensional universe.

As discussed in Chapter 1, a significant difficulty in string phenomenology arises from the "string landscape" . The string landscape refers to the multitude of inequivalent ways in which an 10/11-dimensional string theory can reproduce our 4-dimensional world. Without knowledge of the dynamics for selecting a particular vacuum, it is *a priori* difficult to make concrete experimental predictions from an underlying string theory. In the subsequent chapters of this thesis, we have demonstrated how one can leverage known experimental data to help navigate the string landscape. The general idea is to use all known experimental constraints to exclude large portions of the string landscape. Within the remaining subset of realistic vacuaa, one can make concrete experimental predictions for beyond Standard Model physics.

In Chapters 2 and 3, we have demonstrated the utility of this approach in the context of a particular string theory: the G_2-MSSM. This theory is motivated by 11-dimensional M-theory compactified on a 7-dimensional manifold with G_2 holonomy. In Chapter 2 we showed how hidden sector strong dynamics in the G_2-MSSM stabilizes all moduli fields and breaks Supersymmetry[1]. The gravitino mass, which sets the scale of observable superpartners, is calculated to be $\mathcal{O}(50)$ TeV. In Chapter 3 we further narrowed the G_2-MSSM

---

[1] Chapter 2 also contains a brief introduction to Supersymmetry which plays a central role in this thesis.

landscape by requiring consistency with the measured Higgs and W/Z boson masses. This allowed us to make concrete G_2-MSSM predictions for LHC physics, where the entire particle spectrum is determined by a single unknown parameter. Choosing a benchmark value of $M_{3/2} = 35$ TeV, we obtained a spectrum with a 1.5 TeV gluino and ~ 20 TeV scalar superpartners. This benchmark spectrum illustrates a generic feature of the G_2-MSSM, namely that the gluino is within reach of LHC-14, while the scalar superpartners are not.

Chapters 4 studies future collider signatures in compactified string theories. As stated above, the G_2-MSSM predicts an $\mathcal{O}(\mathrm{TeV})$ gluino and $\gtrsim 20$ TeV scalar superpartners. Such a "mini-split" spectrum is predicted in many compactified string theories. Although the heavier squarks predicted in these models are inaccessible at the LHC, they can be probed at a 100 TeV future collider via squark-gluino associated production. Assuming a light $\lesssim 2$ TeV gluino is present in the spectrum, a 100 TeV proton-proton collider can discover squark masses up to ~ 32 TeV. This channel is currently the only known avenue for directly producing the heavy squarks predicted in many string theories.

Having discussed collider phenomenology in the preceding chapters, Chapter 5 instead focuses on dark matter in compactified string theories. As discussed in the introduction of Chapter 5, recent indirect detection constraints have shown that dark matter in compactified string theories must reside within a hidden sector to avoid fine-tuning. This implies that dark matter was in thermal equilibrium with a "hidden sector" in the early universe which may not have been in thermal equilibrium with the bath of SM particles. In order to classify the potential dark matter production mechanisms, we solved the corresponding Boltzmann equations for dark matter evolution in a two-sector system in the presence of moduli. We identified four distinct parametric regimes for relic dark matter productions, and derived semi-analytic solutions for the dark matter relic abundance. These results are summarized in Section 5.2.5. As shown in Section 5.3, much of the compactified string theory parameter space is ruled out due to dark matter overproduction. This again demonstrates the utility of leveraging experimental constraints to reduce the string landscape.

There are many promising directions for expanding upon the research described in this thesis. The best case scenario would be the discovery of a superpartner at the LHC. Such a discovery would provide a powerful constraint on the string landscape. In the case of the G_2-MSSM, the discovery of a single superpartner (e.g. the gluino) would yield a concrete prediction for the remainder of the spectrum. This results in numerous concrete predictions which can be tested in future collider experiments. On the dark matter side, an open problem is to determine how the dark matter models analyzed in Chapter 5 can be embedded into string-motivated UV completions. This will help sharpen predictions for dark matter detection experiments. For recent work along these directions, see [129].

APPENDIX A

Constraints from EWSB and M_h

In this appendix, we discuss how both EWSB and with consistency with $M_h = 125.2 \pm 0.4$ GeV are imposed to reduce the dimensionality of the $M_{3/2}, \mu, C$ parameter space. We begin by consider the EWSB conditions, given by:

$$\frac{M_Z^2}{2} = \frac{\overline{m}_{H_d}^2 - \overline{m}_{H_u}^2 \tan^2\beta}{\tan^2\beta - 1} - \mu^2 \tag{A.1}$$

$$B\mu = \frac{1}{2}\sin 2\beta \left(\overline{m}_{H_u}^2 + \overline{m}_{H_d}^2 + 2\mu^2\right) \tag{A.2}$$

where $\overline{m}_{H_u}$ and $\overline{m}_{H_d}$ are the tadpole corrected H_u, H_d soft masses, and all parameters are evaluated at the renormalization scale $Q_{EWSB}^2 = m_{\tilde{t}_1} m_{\tilde{t}_2}$. For the M-theory models we consider, we expect $\mu \lesssim 0.1 M_{3/2}$.

There are two independent arguments for such a suppression of μ with respect to $M_{3/2}$. The first is a top-down argument, which is related to the doublet-triplet splitting mechanism [5] discussed in Section 5.5. This mechanism results in a geometric symmetry which forbids the μ term, which is broken by moduli stabilization to generate μ via the Giudice-Masiero mechanism [130]. Thus generically μ is suppressed with respect to $M_{3/2}$ by moduli *vev*'s [61]. This suppression was estimated by [61] to be roughly an order of magnitude, though current theoretical uncertainties preclude a precise estimate. Another argument for $\mu \lesssim 0.1\, M_{3/2}$ is motivated by electroweak naturalness. A measure of fine-tuning in EWSB is the degree to which the two terms on the right hand side of (A.1) are required to cancel in order to obtained the measured value of M_Z. Thus electroweak naturalness favors $\mu^2 \ll M_{3/2}^2$, which mitigates the cancellation in (A.1) required to obtain $M_Z \approx 90$ GeV [64].

In addition to $\mu \lesssim 0.1\, M_{3/2}$, we also expect $0 < \overline{m}_{H_u}^2 \ll \overline{m}_{H_d}^2$, as $m_{H_u}^2$ runs significantly between $Q = M_{GUT}$ to $Q = Q_{EWSB}$ due to the top Yukawa coupling, while the running of $m_{H_d}^2$ is small for moderate $\tan\beta \lesssim 10$. The lower bound $0 < \overline{m}_{H_u}^2$ is required for consistency with $\mu \lesssim 0.1 M_{3/2}$, as can be seen from (A.1). Taking the $B\mu, \overline{m}_{H_d}^2 \gg \mu^2$, $\overline{m}_{H_u}^2$

and $\sin 2\beta \approx 2/\tan\beta$ limit, (A.1) can be written as [64]:

$$\mu^2 \approx \frac{\overline{m}^2_{H_d}}{B^2 - \overline{m}^2_{H_d}} \left(\overline{m}^2_{H_u} + \frac{M_Z^2}{2} \right) \tag{A.3}$$

where $B \approx 2\, M_{3/2}$ at $Q = M_{GUT}$ [29] and $B \approx 1.7 M_{3/2}$ at $Q = Q_{EWSB}$ [64]. Taking $\overline{m}^2_{H_d} \approx m_0^2$ and $\overline{m}^2_{H_u} = M^2_{3/2} f(C)$ where $f(C)$ accounts for the running of m_{H_u} due to the top trilinear A_t, we can recast (A.3) in a more suggestive form:

$$\mu^2 \approx \frac{M^2_{3/2}(1-C)}{B^2 - M^2_{3/2}(1-C)} \left(M^2_{3/2}\, f(C) + \frac{M_Z^2}{2} \right). \tag{A.4}$$

Note that $f(C)$ decreases monotonically as C increases [64]. Thus we have used EWSB conditions to obtain a constraint on the allowed $M_{3/2}, \mu, C$ space; we use one-loop RGE's and one-loop effective potential corrections [131] to compute $f(C)$ for Figure 3.1. In order to minimize large logarithmic corrections, we run α_s and y_t using a 2-step procedure which explicity accounts for the decoupling of squarks at $Q = Q_{EWSB}$.

We now discuss how the constraint on M_h is incoporated in our analysis. The mass of the lightest Higgs boson in the MSSM decoupling limit is given schematically by:

$$M_h^2 = M_Z^2 \cos^2 2\beta + \delta M_h^2 \tag{A.5}$$

where δM_h^2 denotes radiative corrections from both SM and MSSM particles; the value of δM_h^2 is fixed for given values of $M_{3/2}, \mu, C$. We can then use the EWSB condition (A.2) in the $B\mu, \overline{m}^2_{H_d} \gg \mu^2$, $\overline{m}^2_{H_u}$ and $\sin 2\beta \approx 2/\tan\beta$ limit to express $\tan\beta$ in terms $M_{3/2}, C$ and μ:

$$\tan\beta \approx \frac{m_0^2}{B\mu} \approx \frac{M_{3/2}(1-C)}{B\mu} \tag{A.6}$$

Thus combining (A.5) and (A.6) with $M_h = 125.2 \pm 0.4$ GeV, we obtain an additional constraint in the $M_{3/2}, \mu, C$ parameter space. To compute M_h for given $M_{3/2}, \mu, C$, we use the "match-and-run" procedure, outlined for example in [132, 31]. Note that some of the authors here made an error in [31] regarding SM radiative corrections to M_h; correcting this error increases M_h by ~ 1.5 GeV. Our calculation here uses 3-loop RGE's and 2-loop threshold corrections for the matching procedure [133]. From Figure 3.1, we see that the slice of parameter space consistent with $M_h = 125.2 \pm 0.4$ has a non-negligible width. This is due predominantly to experimental uncertanties in M_t, α_s and M_h [31]; more precise measurements of these quantities will sharpen constraints on this parameter space.

APPENDIX B

Event generation

Signal events were generated using `MADGRAPH5` [71], with showering and hadronization implemented via `PYTHIA6.4` [134]. We do not perform MLM for the signal events. We have validated this approximation by performing MLM with 2 additional jets for a number of benchmark spectra. We use the simulated Snowmass backgrounds [135], processed with `Delphes3.1.2` [136] supplemented by the Snowmass detector card [137] for a $\sqrt{s} = 100$ TeV hadron collider. Production cross sections for squark-gluino associated production are computed at NLO using `PROSPINO2` [72]. For squark-Wino/Bino production we use the LO result computed by `MADGRAPH5`.Event analysis is performed with `MadAnalysis`5 [138]. We expect our kinematic cuts to effectively remove any contamination from QCD backgrounds and pileup effects, so we neglect both of these in our analysis. Note that for squark-gluino associated production in the $m_{\tilde{q}} \gg m_{\tilde{g}}$ region, the dijet background may not be negligible for non-compressed spectra. For these spectra, jet substructure techniques can help distinguish signal events from the QCD background [139].

APPENDIX C

Justification of Approximations for R, R'

In Section 5.2.1, analytic approximations for R and R' were obtained assuming that all other terms aside from the modulus decay term can be neglected in dR'/dA and dR/dA if $M_{X'}, M_X \ll m_\phi$. In this appendix, we will justify this approximation. Note from (5.7) that the modulus decay terms in dR'/dA and dR/dA grow like $A^{3/2}$ during the modulus domination phase, and peak when $T \sim T_D$. Thus in determining whether or not certain terms in dR'/dA and dR/dA are negligible compared to the modulus decay term, it is sufficient to focus on the Boltzmann equations at temperatures near T_D.

First, consider the $X \to X' + ...$ decay term in dR'/dA and dR/dA. At $T \gtrsim T_D$, X has already reached QSE, assuming $\langle \Gamma_X \rangle > \Gamma_\phi$. Taking $X = X_{\text{QSE}}$ with $b \approx 1$, the $X' \to X + ...$ decay terms are given by:

$$\begin{aligned}
\widetilde{H}\frac{dR}{dA} &= B_X B_{X\to X'R}\, c_\rho^{1/2} \left(\frac{E_X - E_{X'}}{m_\phi}\right) A^{3/2}\Phi + ... \\
\widetilde{H}\frac{dR'}{dA} &= B_X B_{X\to X'R'}\, c_\rho^{1/2} \left(\frac{E_X - E_{X'}}{m_\phi}\right) A^{3/2}\Phi + ...
\end{aligned} \tag{C.1}$$

Here $B_{X\to X'R}$ and $B_{X\to X'R'}$ are the branching fractions of X into $X'R$ and $X'R'$. Thus we see that the $X \to X' + ...$ decay terms are suppressed with respect to the modulus decay term by a factor of $(E_X - E_{X'})/m_\phi$; a similar conclusion holds if X does not decay to X'. Next, consider the annihilation terms. For the $\langle\sigma v\rangle$ term in dR/dA, $X_{\text{eq}} \approx 0$ and $X \approx X_{\text{QSE}}$ for $T \sim T_D$. Thus for temperature-independent $\langle\sigma v\rangle$, the annihilation term in dR/dA falls like $A^{-3/2}$ for $T \gtrsim T_D$, and will be numerically insignificant at T_D due to suppression by negative powers of the scale factor.

The argument for the $\langle\sigma v\rangle'$ term in dR'/dA is less straightforward. First, consider the case where $\langle\sigma v\rangle' > \langle\sigma v\rangle'_c$ such that X' reaches QSE at $T' \sim T'_D$. If $X'_{\text{QSE}} \approx X'_{\text{eq}}$, the annihilation term vanishes and is trivially negligible. If instead X'_{eq} is negligible in X'_{QSE} (5.33) at $T' \sim T'_D$ (as is the case for QSE_{nr}), we can take $X' \approx X'_{QSE}$ and write the $\langle\sigma v\rangle'$

term as:

$$\widetilde{H}\frac{dR'}{dA} = c_\rho^{1/2} B_{\rm tot}\left(\frac{2E_{X'}}{m_\phi}\right) A^{3/2}\Phi + ... \tag{C.2}$$

which is suppressed with respect to the modulus decay term by a factor of $E_{X'}/m_\phi$. Now consider the case where $\langle\sigma v\rangle' < \langle\sigma v\rangle'_c$ such that X' is not in QSE at T'_D. As discussed in Section 5.2.4, we can write X' at $T' \gtrsim T'_D$ as $X' = X'_{\rm mod} + X'_{\rm ann}$, where $X'_{\rm mod}$ comes from integrating the modulus decay term:

$$X'_{\rm mod} = \frac{2}{3}{c_\rho}^{1/2}\frac{T_{RH}B_{\rm tot}}{m_\phi}A^{3/2}\Phi^{1/2} \tag{C.3}$$

and $X'_{\rm ann}$ is determined by the $\langle\sigma v\rangle'$ term. In the case where $M_{X'} > T_{D'}$, $X'_{\rm ann}$ is negligible compared to $X'_{\rm mod}$ unless $B_{\rm tot} \ll 1$ (see Sections 5.2.4.1 and 5.2.4.2). Taking $X' \approx X'_{\rm mod}$, the $\langle\sigma v\rangle'$ term in dR'/dA can be written as:

$$\widetilde{H}\frac{dR'}{dA} = \frac{4}{9}{c_\rho}^{1/2}\left(2\frac{B_{\rm tot}E_{X'}}{m_\phi}\right)\frac{\langle\sigma v\rangle'}{\langle\sigma v\rangle'_c}A^{3/2}\Phi + ... \tag{C.4}$$

Thus in the case where $\langle\sigma v\rangle' < \langle\sigma v\rangle'_c$ and $M_{X'} > T'_D$, the $\langle\sigma v\rangle'$ term in dR'/dA is suppressed by at least a factor of $E_{X'}/m_\phi$ with respect to the modulus decay term.

Finally, consider the case where $\langle\sigma v\rangle' < \langle\sigma v\rangle'_c$ and $M_{X'} < T'_D$, corresponding to the $IA_{\rm r}$ scenario (see Section 5.2.4.2). In this case $X' \ll X'_{eq}$ and we can write the $\langle\sigma v\rangle'$ annihilation term as:

$$\widetilde{H}\frac{dR'}{dA} \approx c_1^{1/2}\, M_{\rm pl}\,\eta^2\,\frac{48\, g_*(T_{RH})\, {c_\xi}^2\, \zeta(3)^2 E_{X'}\,\langle\sigma v\rangle' \,T_{RH}^2}{5\pi^6 g'_*(T')^2\, T'^2}\Phi_I A^{3/2} + ... \tag{C.5}$$

where we have used (5.17)-(5.19) to relate A and T'. Evaluating (C.5) at $T' = T'_D$, we obtain:

$$\begin{aligned}\widetilde{H}\frac{dR'}{dA}\Big|_{T'=T'_D} &\approx c_1^{1/2}\, M_{\rm pl}\, T_{RH}\,\eta\left(\frac{\eta\, g_*(T_{RH})}{g'_*(T'_D)}\right)^{3/4}\left(\frac{48\sqrt{3}\, {c_\xi}^2\zeta(3)^2\,\langle\sigma v\rangle'}{5\pi^6\, g'_*(T')}\right)\Phi_I A^{3/2} + ...\\ &\approx c_\rho^{1/2}\,\eta\left(\frac{0.16\, c_\xi\,\zeta(3)}{g'_*(T'_D)}\right)\left(\frac{\langle\sigma v\rangle'}{\langle\sigma v\rangle'_c}\right)\Phi_I A^{3/2} + ...\end{aligned} \tag{C.6}$$

Thus the $\langle\sigma v\rangle'$ term in dR'/dA is suppressed with respect to the modulus decay term by a factor of the order of $0.1\,\langle\sigma v\rangle' / \langle\sigma v\rangle'_c$.

To summarize, the above arguments show that the approximations made in solving the equations for R and R' in solving (5.7) are justified, as can also be confirmed by the agreement of the approximate and exact solutions in Appendix E.

APPENDIX D

A Very Long-lived X Particle

For most of this work, we have assumed $\Gamma_X > \mathcal{O}(1)\,\Gamma_\phi$ such that X decays are efficient before the end of modulus domination. This assumption is well-motivated from both theoretical and phenomenological points of view. To see this, note that the modulus decays through Planck suppressed operators such that the decay width is parametrically given by: $\Gamma_\phi \sim m_\phi^3/M_{\rm pl}^2 \sim 10^{-24}$ GeV for $m_\phi \sim 50$ TeV. Thus, as long as the visible and dark sectors are coupled by larger than gravitational strength interactions, one expects $\Gamma_X \gg \Gamma_\phi$ for a wide class of dark sector models. This is also true if the coupling between the two sectors arises by integrating out Kaluza-Klein (KK) modes of the extra dimensions or heavy GUT multiplets of some underlying GUT model, as even these mediators are lighter than the Planck scale. In addition, from a phenomenological point of view, X decays to visible sector particles can spoil the successful predictions of BBN if $\Gamma_X < H(T_{BBN}) \sim T_{BBN}^2/M_{pl}$ where $T_{BBN} \sim 1$ MeV [140]. To avoid these constraints, for $\Gamma_X \lesssim \Gamma_\phi$, Γ_X should lie in a narrow window:

$$T_{RH}^2 \simeq \Gamma_\phi M_{\rm pl} \gtrsim \; \Gamma_X M_{\rm pl} \; \gtrsim T_{BBN}^2. \tag{D.1}$$

Despite these considerations, for completeness we briefly discuss in this appendix the case where $\Gamma_X \lesssim \Gamma_\phi$. In this case, X is effectively stable during modulus domination (as $H > \Gamma_\phi > \Gamma_X$). Thus for $H > \Gamma_X$ we can treat X as a stable relic. If X is a WIMP, its comoving abundance will become fixed at $T \sim T_D$ via the $QSE_{\rm nr}$ mechanism, which is the precise generalization of the non-thermal WIMP miracle [69, 98]. Once the Hubble parameter drops below Γ_X during radiation domination, the remaining X abundance will decay to yield X' particles. The dynamics of such a process was studied in detail in [107]. From the results of [107], we see that there are three possibilities for the resulting parametrics of $\Omega_{X'}h^2$:

- X' is in equilibrium when $H = \Gamma_X$ (which is only possible for $FO_{\rm nr}^{\rm rad}$ and $FO_{\rm r}^{\rm rad}$).

X' will continue to track its equilibrium abundance until freeze-out. In this case $\Omega_{DM}\, h^2$ is completely insensitive to X decays.

- X' is out of equilibrium when $H = \Gamma_X$, and X decays yield an X' abundance which is less than the critical abundance required for X' annihilations. This gives rise to the *freezeout* & *decay* ($FO\&D$) mechanism described in [107]. In terms of dimensionless comoving variables, $X_{\rm QSE}(A_c) < X'_{\rm crit}\big|_{H=\Gamma_X}$, where $X_{\rm QSE}(A_c)$ is given by the $QSE_{\rm nr}$ mechanism as described in Section 5.2.3.1 and $X'_{\rm crit}$ is defined in (5.23). The resulting contribution to the X' comoving abundance is insensitive to Γ_X, and is given simply by $\Delta X' \approx X_{\rm QSE}(A_c)$. This contribution must be added to the X' abundance which results from the production mechanisms described in Section 5.2.2.

- X' is out of equilibrium when $H = \Gamma_X$, and X decays yield an X' abundance which exceeds the critical abundance required for X' annihilations. In terms of dimensionless comoving variables this occurs if $X_{\rm QSE}(A_c) > X'_{\rm crit}\big|_{H=\Gamma_X}$. The X' particles produced from X decays will then annihilate until $X' \approx X'_{\rm crit}\big|_{H=\Gamma_X}$. This was referred to as the "*freezeout* & *decay and re-annihilation*" ($FO\&D_{\rm r}$) in [107]; the resulting X' relic abundance scales like $\Omega_{DM}\, h^2 \propto \frac{1}{\Gamma_X^{1/2} \langle\sigma v\rangle'}$.

Before concluding this appendix, we remark that the '*freeze-in*' mechanisms (FI and FI_r) described in [141, 107] are not important for the models considered here. Recall that FI is due to $X \to X' + ...$ decays which occur during the radiation domination era when X is still relativistic and in equilibrium. However, it turns out that freeze-in due to X decays is negligible during the modulus dominated era. To see this, consider the X decay term in dX'/dA. We saw in section 5.2.1.3 that X attains QSE at some scale factor A (say A_X) before A_D if $\Gamma_X > \mathcal{O}(1)\,\Gamma_\phi$. For $A < A_X$, X is given by $X \approx X_{\rm eq}$, while for $A_X < A \lesssim A_D$, X is given by $X \approx X_{\rm QSE}$. In the analysis in Section 5.2.1.3, the effect of X decays when $1 < A \leq A_X$ and $X \approx X_{eq}$, which corresponds to freeze-in effects from X decays, was neglected. To see that it is justified to do so, note that the integration of the decay term gives (up to overall constants):

$$\begin{aligned}\int_1^{A_D} dA\, X A^{1/2} &\approx \int_1^{A_X} dA\, X_{\rm eq} A^{1/2} + \int_{A_X}^{A_D} dA\, X_{\rm QSE} A^{1/2} \\ &\approx \frac{c_\xi}{\pi^2 T_{RH}^3} \int_1^{A_X} dA\, A^{7/2} T^3 + \frac{2}{3} {A_D}^{3/2} \left(g_X B_X \frac{\Gamma_\phi T_{RH}}{\Gamma_X m_\phi} \right) \Phi \qquad \text{(D.2)}\end{aligned}$$

where A_X corresponds to the scale factor at which either X becomes non-relativistic or X enters QSE (whichever occurs first). Comparing the first and second terms in (D.2), we find:

$$\frac{\int_1^{A_X} dA\, X_{\rm eq} A^{1/2}}{\int_{A_X}^{A_D} dA\, X_{\rm QSE} A^{1/2}} \sim \left(\frac{T_D}{T_X}\right)^4 \left(\frac{\Gamma_X m_\phi}{B_X \Gamma_\phi T_{RH}^4}\right) \frac{(\kappa T_{\rm max})^8}{{T_X}^5 \Phi_I} \sim \left(\frac{T_{RH}^6 \Gamma_X m_\phi M_{\rm pl}}{{T_X}^9 B_X}\right) \tag{D.3}$$

where we have used $T \approx \kappa T_{\rm max} A^{-3/8}$ and $(\kappa T_{\rm max})^8/\Phi_I \sim {T_{RH}}^8$ (see (5.18)). There are now two possibilities for T_X. If X enters QSE before X becomes non-relativistic, then $T_X \sim (\Gamma_X M_{\rm pl} {T_{RH}}^2)^{1/4} > M_X$. If instead X becomes non-relativistic before QSE is reached, then $T_X \sim M_X$ and $\Gamma_X \lesssim \frac{M_X^4}{{T_{RH}}^2 M_{\rm pl}}$. Since T_X is smaller in the latter case, the ratio (D.3) is maximized for $T_X \sim M_X$, and one gets:

$$\frac{\int_1^{A_X} dA\, X_{\rm eq} A^{1/2}}{\int_{A_X}^{A_D} dA\, X_{\rm QSE} A^{1/2}} \lesssim \frac{T_{RH}^4\, m_\phi}{B_X\, M_X^5} \simeq \frac{10^{-13}}{B_X} \left(\frac{T_{RH}}{10\,{\rm MeV}}\right)^4 \left(\frac{m_\phi}{100\,{\rm TeV}}\right) \left(\frac{100\,{\rm GeV}}{M_X}\right)^5 . \tag{D.4}$$

Thus the freeze-in production of X' from X decays can be neglected for reasonable choices of parameters, provided B_X is not extremely tiny.

APPENDIX E

Accuracy of Approximate Solutions

In this section, we compare the semi-analytic approximations obtained above with the full numerical solution to (5.7). The accuracy of these approximations is depicted in Figures E.1 and E.2. In these plots we use the benchmark values of parameters as in (5.5); however we take $g'_*(T') = 20 \neq g_*(T)$ to ensure that the $g'_*(T')$ dependence has been properly captured. Figure E.1 shows the accuracy of the approximate solutions for $M_{X'} = 10$ GeV and $B_{\rm tot} = 0.1$. In the top plot, the green curve shows the numerical solution, while the black curve in the top plot shows the approximate expression for DM production through QSE_{nr} (5.38). The bottom plot shows the ratio of the approximate $QSE_{\rm nr}$ result to the exact result, which is close to unity if $\langle\sigma v\rangle' \gg \langle\sigma v\rangle'_c$.

Figure E.2 shows the accuracy of the approximate solutions for $B_{\rm tot} = 0$; note that in this case $\langle\sigma v\rangle'_c$ becomes effectively infinite for $M_{X'} > T'_D$, see (5.35). The top plot shows $\Omega_{DM}h^2$ as a function of $\langle\sigma v\rangle'$ for $M_{X'} = 10$ GeV. For these parameters, DM production occurs either via $FO^{\rm mod}_{\rm nr}$ for $\langle\sigma v\rangle' > \langle\sigma v\rangle'_0$ or via $IA_{\rm nr}$ for $\langle\sigma v\rangle' < \langle\sigma v\rangle'_0$ where $\langle\sigma v\rangle'_0$ is defined in (5.46). The green curve shows the numerical solution; the red curve shows the approximation for $IA_{\rm nr}$ (5.51); and the black curve shows the approximation for $FO^{\rm mod}_{\rm nr}$ (5.45). The bottom plot shows a similar plot with $M_{X'} = 10^{-6}$ GeV. In this case DM production occurs via $IA_{\rm r}$ for $\langle\sigma v\rangle' < \langle\sigma v\rangle'_c$ and via thermal freeze-out ($FO^{\rm rad}_{\rm r}$ and $FO^{\rm rad}_{\rm nr}$) for $\langle\sigma v\rangle' > \langle\sigma v\rangle'_c$. The green curve shows the numerical solution, the red curve shows the approximate expression for $IA_{\rm r}$ (5.52), while the black curve shows the approximate expression for $FO^{\rm rad}_{\rm nr}$ (5.40). Within their respective regimes of validity, (5.51), (5.52) and (5.45) are accurate to within $\sim 5\%$, while (5.41) and (5.40) are accurate to within $\sim 15\%$.

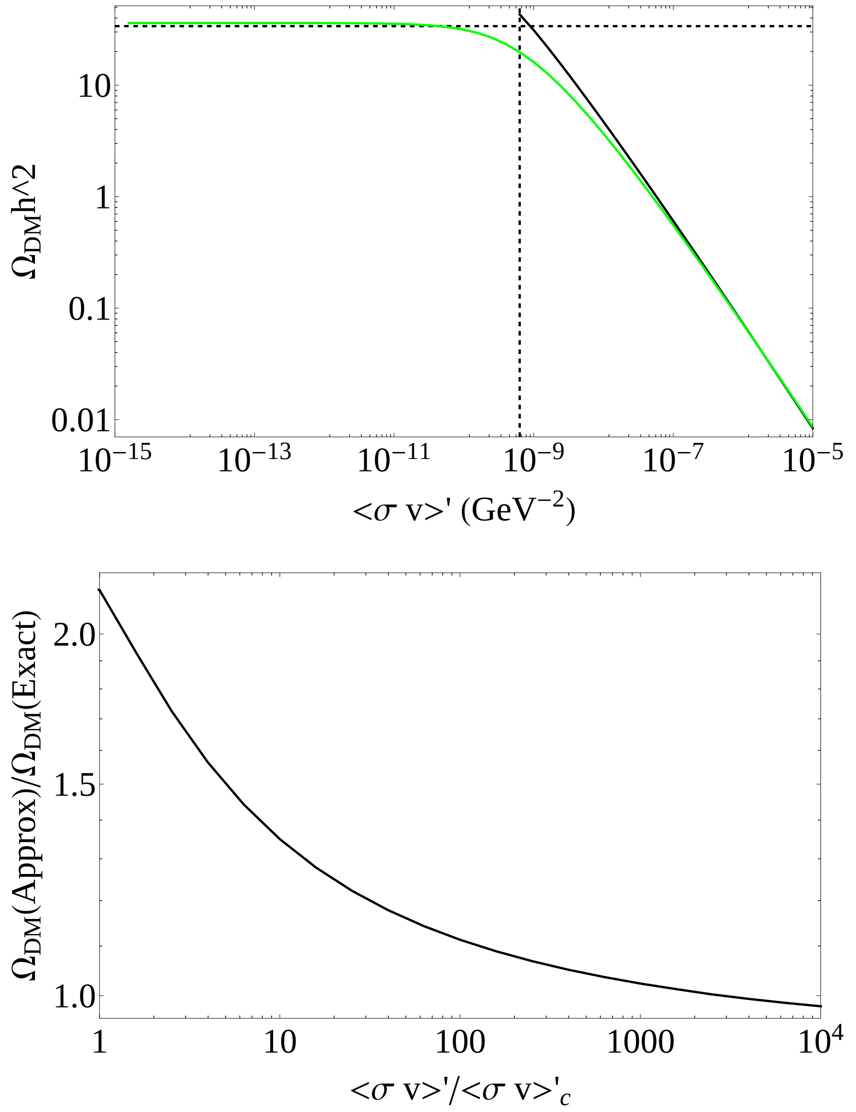

Figure E.1: Top: $\Omega_{DM}h^2$ as a function of $\langle \sigma v \rangle'$ for $M_{X'} = 10$ GeV and $B_{\rm tot} = 0.1$. The green curve shows the numerical solution, while the black curve shows the approximate $QSE_{\rm nr}$ solution (5.35). The vertical dashed line represents $\langle \sigma v \rangle' = \langle \sigma v \rangle'_c$ as defined in (5.35), while the horizontal dashed line shows represents the modulus decay contribution given in (5.43), which is valid for $\langle \sigma v \rangle' < \langle \sigma v \rangle'_c$. Bottom: the ratio of the approximate result for $QSE_{\rm nr}$ to the exact result.

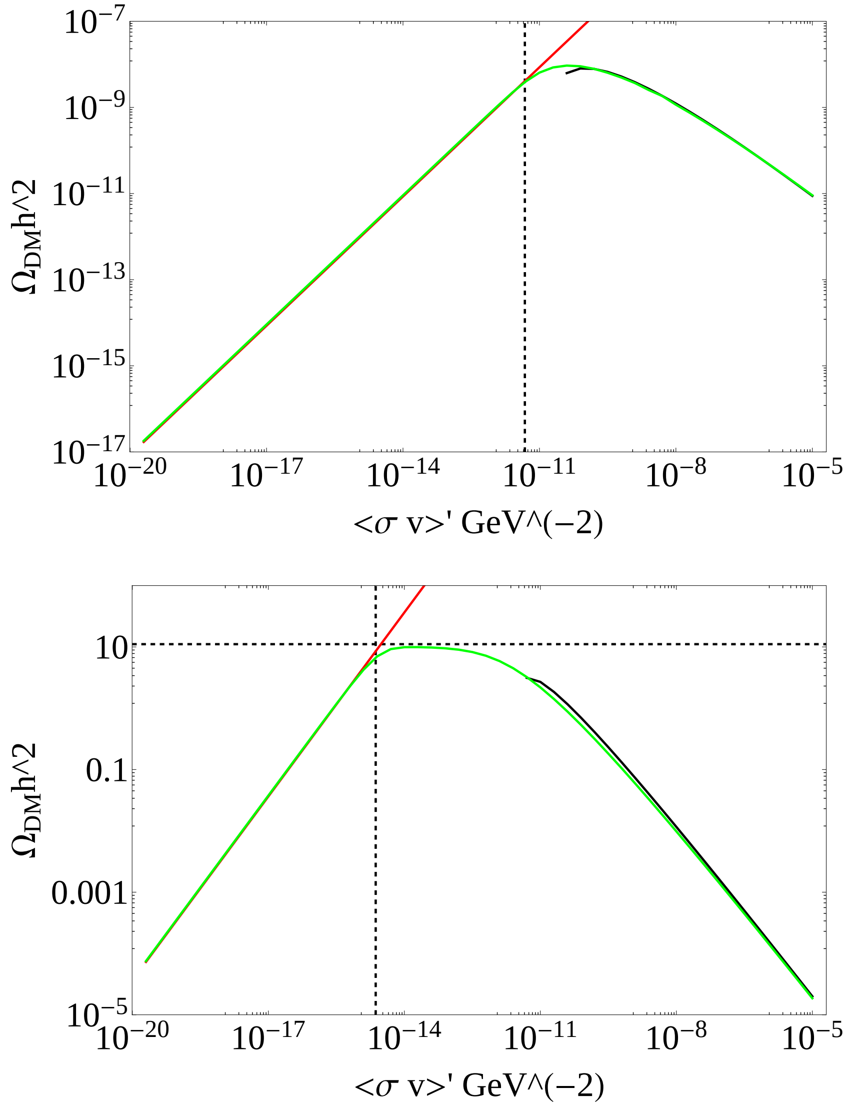

Figure E.2: Top: $\Omega_{DM}h^2$ as a function of $\langle \sigma v \rangle'$ for $M_{X'} = 10$ GeV and $B_{\rm tot} = 0$. Bottom: similar plot for $M_{X'} = 10^{-6}$ GeV and $B_{\rm tot} = 0$. The green curves show the numerical solution, the red curve shows the approximation for $IA_{\rm nr}$ (top) and $IA_{\rm r}$ (bottom), while the black curve shows the approximation for $FO_{\rm nr}^{\rm mod}$ (top) and $FO_{\rm nr}^{\rm rad}$ (bottom). In the left plot the vertical dashed line represents $\langle \sigma v \rangle' = \langle \sigma v \rangle'_0$, defined in (5.46), while in the bottom plot the vertical line represents $\langle \sigma v \rangle' = \langle \sigma v \rangle'_c$ in the case where $M_{X'} < T'_D$ (see (5.35)). The dashed horizontal line in the bottom plot shows the approximate solution for $FO_{\rm r}^{\rm rad}$.

APPENDIX F

Temperature Dependence of the Annihilation Cross Section

In Section 5.2.2, (semi)-analytic expressions for $\Omega_{DM}\, h^2$ were obtained assuming that $\langle \sigma v \rangle'$ is temperature dependent. In this section, we generalize the results of Section 5.2.2 for temperature dependent $\langle \sigma v \rangle'$. For scenarios where the contribution to $\Omega_{DM}\, h^2$ is determined by non-relativistic X' annihilation ($QSE^{\rm nr}$, $FO^{\rm rad}_{\rm nr}$, $FO^{\rm mod}_{\rm nr}$ and $IA_{\rm nr}$) we will consider p-wave annihilations where $\langle \sigma v \rangle' = T'/\Lambda^3$. For scenarios where the contribution to $\Omega_{DM} h^2$ is determined by relativistic annihilations ($IA_{\rm r}$) we consider the case where $\langle \sigma v \rangle' = T^2/\Lambda^4$, corresponding to annihilation through a heavy bosonic mediator. Note that for $FO^{\rm rad}_{\rm r}$, $\Omega_{DM} h^2$ is independent of $\langle \sigma v \rangle'$ so (5.41) holds regardless of the temperature dependence of $\langle \sigma v \rangle'$.

- For $QSE_{\rm nr}$, (5.37) and (5.38) are still valid for p-wave annihilation, provided the annihilation cross section is parameterized as:

$$\langle \sigma v \rangle' = \frac{T'}{\Lambda^3} = \frac{T'_D}{\Lambda^3} \left(\frac{\tilde{A}_D}{\tilde{A}_c} \right) , \tag{F.1}$$

  where in the second equality we have assumed $T' \propto A^{-1}$ as in radiation domination. In order to match the numerical result, we instead use $\kappa = 1.8$ in (5.37) and (5.38).

- For $FO^{\rm rad}_{\rm nr}$, the expression for $\hat{x}'_F$ is given by:

$$\hat{x}'_F \equiv \frac{M_{X'}}{T'_{FO}} = \log \left(\frac{3}{8\pi^3} \sqrt{\frac{10\,\eta}{g'_*(T'_{FO})}} g' \left(\frac{{M_{X'}}^2 M_{\rm pl}}{\Lambda^3} \right) \kappa_p^{\rm rad} (\hat{x}'_F)^{-1/2} \right) \tag{F.2}$$

while $\Omega_{DM} h^2$ is given by:

$$\frac{\Omega\, h^2\ [FO^{\rm rad}_{\rm nr}]}{\Omega_R\, h^2} \approx \left[\frac{4\sqrt{5}}{\sqrt{\pi}}\right] \left[\frac{\eta^{1/4}}{(1-\eta)^{3/4}}\right] \left[\frac{1}{g_*(T_{FO}) g'_*(T'_{FO})}\right]^{1/4} \left[\frac{\kappa_p^{\rm mod}\, (\hat{x}'_F)^2\, \Lambda^3}{M_{X'}\, M_{\rm pl} T_{\rm now}}\right] \tag{F.3}$$

Here $\kappa_p^{\rm rad} = 2$ is a constant which is chosen to match the full numerical result.

- For $FO^{\rm mod}_{\rm nr}$, the expression for x'_F is given by:

$$x'_F = \ln\left[\left(\frac{3}{2\sqrt{10}\pi^3}\right)\left(\frac{g' g_*(T_{RH})^{1/2}}{g'_*(T'_{FO})}\right)\left(\frac{M_{\rm pl} T^2_{RH}}{\Lambda^3}\right) \kappa_p^{\rm mod}\, \eta\, {x'_F}^{3/2}\right] \tag{F.4}$$

while $\Omega_{\rm ann} h^2$ is given by:

$$\frac{\Omega_{\rm ann}\, h^2\ [FO^{\rm mod}_{\rm nr}]}{\Omega_R\, h^2} \approx \left[\frac{8\,\eta}{\sqrt{5\pi}\, L^{3/4}}\right]\left[\frac{g_*(T_{RH})^{1/2}}{g'_*(T'_{FO})}\right]\left[\frac{T_{RH}}{M_{X'}}\right]^3\left[\frac{\kappa_p^{\rm mod} {x'_F}^5 \Lambda^3}{M_{X'}\, M_{\rm pl} T_{\rm now}}\right] \tag{F.5}$$

Here $\kappa_p^{\rm mod} = 5/4$ is a constant which is chosen to match the full numerical result (see also [105]).

- For $IA_{\rm nr}$, it is straightforward to show that for $\langle\sigma v\rangle' = T'/\tilde{M}^3$, the expression analogous to (5.51) is given by:

$$\frac{\Omega_{\rm ann}\, h^2\ [IA_{\rm nr}]}{\Omega_R\, h^2} \approx \left[\frac{48\, {g'}^2\, \chi_p\, \eta^3}{125^{1/2}\pi^{15/2}\, L^{3/4}}\right]\left[\frac{{g_\star}^{3/2}(T_{RH})}{{g'_\star}^3(T'_\star)}\right]\left[\left(\frac{T_{RH}}{M_{X'}}\right)^7\left(\frac{M_{\rm pl} {M_{X'}}^3}{\Lambda^3 T_{\rm now}}\right)\right] \tag{F.6}$$

where χ_p is given by:

$$\chi_p \equiv \int_{\frac{M_{X'}}{T'_{\rm max}}}^{\frac{M_{X'}}{T'_D}} dx' {x'}^8 K_2(x')^2 \tag{F.7}$$

The integrand peaks at $T'_* \approx 0.33 M_{X'}$; if $T'_* \ll T'_{\rm max}$ and $T'_* \gg T'_D$, $\chi_p \approx 80$.

- For $IA_{\rm r}$, we are interested in the case where $\langle\sigma v\rangle' = {T'}^2/\Lambda^4$ (see above). The expression analgous to (5.52) is given by:

$$\frac{\Omega_{\rm ann} h^2}{\Omega_R h^2} = \left[\frac{48 {c_\xi}^2 \zeta(3)^2}{125^{1/2}\pi^{15/2} L^{3/4}}\left(\frac{T'_D}{T'_*}\right)^4\right]\left[\frac{\eta^2 g_*(T_{RH})^{1/2}}{g'_*(T'_D)^2}\right]\left[\frac{{T_{RH}}^3 M_{X'} M_{\rm pl}}{T_{\rm now}\Lambda^4}\right] \tag{F.8}$$

In the above, $T'_* \approx T'_D/1.35$ is chosen to match the numerical result, and is related to the temperature at which the integrand of $\int dA\, {T'}^2 A^{7/2} {n'_{\rm eq}}^2 \widetilde{H}^{-1}$ peaks. Note that we can recover (F.8) from (5.52) by making the replacement:

$$\langle \sigma v \rangle' \to 0.17 \times \left(\frac{\eta^{1/2} g_*(T_{RH})^{1/2}}{\Lambda^4 g'_*(T'_D)^{1/2}} \right) T_{RH}^2 \tag{F.9}$$

BIBLIOGRAPHY

[1] B. S. Acharya, "M theory, Joyce orbifolds and superYang-Mills," *Adv. Theor. Math. Phys.*, vol. 3, pp. 227–248, 1999.

[2] B. S. Acharya, "On Realizing N=1 superYang-Mills in M theory," 2000.

[3] B. S. Acharya and E. Witten, "Chiral fermions from manifolds of G(2) holonomy," 2001.

[4] E. Witten, "Anomaly cancellation on G(2) manifolds," 2001.

[5] E. Witten, "Deconstruction, G(2) holonomy, and doublet triplet splitting," in *Supersymmetry and unification of fundamental interactions. Proceedings, 10th International Conference, SUSY'02, Hamburg, Germany, June 17-23, 2002*, pp. 472–491, 2001.

[6] M. Atiyah and E. Witten, "M theory dynamics on a manifold of G(2) holonomy," *Adv. Theor. Math. Phys.*, vol. 6, pp. 1–106, 2003.

[7] T. Friedmann and E. Witten, "Unification scale, proton decay, and manifolds of G(2) holonomy," *Adv. Theor. Math. Phys.*, vol. 7, no. 4, pp. 577–617, 2003.

[8] B. S. Acharya and S. Gukov, "M theory and singularities of exceptional holonomy manifolds," *Phys. Rept.*, vol. 392, pp. 121–189, 2004.

[9] S. A. R. Ellis, G. L. Kane, and B. Zheng, "Superpartners at LHC and Future Colliders: Predictions from Constrained Compactified M-Theory," *JHEP*, vol. 07, p. 081, 2015.

[10] S. A. R. Ellis and B. Zheng, "Reaching for squarks and gauginos at a 100 TeV p-p collider," *Phys. Rev.*, vol. D92, no. 7, p. 075034, 2015.

[11] G. L. Kane, P. Kumar, B. D. Nelson, and B. Zheng, "Dark Matter Production Mechanisms with a Non-Thermal Cosmological History - A Classification," 2015.

[12] G. Aad *et al.*, "Observation of a new particle in the search for the Standard Model Higgs boson with the ATLAS detector at the LHC," *Phys. Lett.*, vol. B716, pp. 1–29, 2012.

[13] S. Chatrchyan *et al.*, "Observation of a new boson at a mass of 125 GeV with the CMS experiment at the LHC," *Phys. Lett.*, vol. B716, pp. 30–61, 2012.

[14] G. ’t Hooft, “Naturalness, chiral symmetry, and spontaneous chiral symmetry breaking,” *NATO Sci. Ser. B*, vol. 59, p. 135, 1980.

[15] F. Wilczek, “Problem of Strong p and t Invariance in the Presence of Instantons,” *Phys. Rev. Lett.*, vol. 40, pp. 279–282, 1978.

[16] J. Polchinski, *String theory. Vol. 1: An introduction to the bosonic string*. Cambridge University Press, 2007.

[17] J. Polchinski, *String theory. Vol. 2: Superstring theory and beyond.* Cambridge University Press, 2007.

[18] D. Bailin and A. Love, “KALUZA-KLEIN THEORIES,” *Rept. Prog. Phys.*, vol. 50, pp. 1087–1170, 1987.

[19] N. Arkani-Hamed, S. Dimopoulos, and G. R. Dvali, “The Hierarchy problem and new dimensions at a millimeter,” *Phys. Lett.*, vol. B429, pp. 263–272, 1998.

[20] I. Antoniadis, N. Arkani-Hamed, S. Dimopoulos, and G. R. Dvali, “New dimensions at a millimeter to a Fermi and superstrings at a TeV,” *Phys. Lett.*, vol. B436, pp. 257–263, 1998.

[21] J. Conlon, “The What and Why of Moduli,” *Adv. Ser. Direct. High Energy Phys.*, vol. 22, pp. 11–22, 2015.

[22] J. P. Conlon, “The QCD axion and moduli stabilisation,” *JHEP*, vol. 05, p. 078, 2006.

[23] P. Candelas, G. T. Horowitz, A. Strominger, and E. Witten, “Vacuum Configurations for Superstrings,” *Nucl. Phys.*, vol. B258, pp. 46–74, 1985.

[24] L. J. Dixon, J. A. Harvey, C. Vafa, and E. Witten, “Strings on Orbifolds,” *Nucl. Phys.*, vol. B261, pp. 678–686, 1985.

[25] L. J. Dixon, J. A. Harvey, C. Vafa, and E. Witten, “Strings on Orbifolds. 2.,” *Nucl. Phys.*, vol. B274, pp. 285–314, 1986.

[26] M. R. Douglas, “The Statistics of string / M theory vacua,” *JHEP*, vol. 05, p. 046, 2003.

[27] B. S. Acharya, K. Bobkov, G. Kane, P. Kumar, and D. Vaman, “An M theory Solution to the Hierarchy Problem,” *Phys.Rev.Lett.*, vol. 97, p. 191601, 2006.

[28] B. S. Acharya, K. Bobkov, G. L. Kane, P. Kumar, and J. Shao, “Explaining the Electroweak Scale and Stabilizing Moduli in M Theory,” *Phys.Rev.*, vol. D76, p. 126010, 2007.

[29] B. S. Acharya, K. Bobkov, G. L. Kane, J. Shao, and P. Kumar, “The G(2)-MSSM: An M Theory motivated model of Particle Physics,” *Phys.Rev.*, vol. D78, p. 065038, 2008.

[30] G. Papadopoulos and P. K. Townsend, "Compactification of D = 11 supergravity on spaces of exceptional holonomy," *Phys. Lett.*, vol. B357, pp. 300–306, 1995.

[31] G. Kane, P. Kumar, R. Lu, and B. Zheng, "Higgs Mass Prediction for Realistic String/M Theory Vacua," *Phys. Rev.*, vol. D85, p. 075026, 2012.

[32] G. Kane, R. Lu, and B. Zheng, "Review and Update of the Compactified M/string Theory Prediction of the Higgs Boson Mass and Properties," *Int. J. Mod. Phys.*, vol. A28, p. 1330002, 2013.

[33] B. S. Acharya, G. Kane, and P. Kumar, "Compactified String Theories – Generic Predictions for Particle Physics," *Int.J.Mod.Phys.*, vol. A27, p. 1230012, 2012.

[34] B. S. Acharya and K. Bobkov, "Kahler Independence of the G(2)-MSSM," *JHEP*, vol. 1009, p. 001, 2010.

[35] H. K. Dreiner, H. E. Haber, and S. P. Martin, "Two-component spinor techniques and Feynman rules for quantum field theory and supersymmetry," *Phys. Rept.*, vol. 494, pp. 1–196, 2010.

[36] H. E. Haber and G. L. Kane, "The Search for Supersymmetry: Probing Physics Beyond the Standard Model," *Phys. Rept.*, vol. 117, pp. 75–263, 1985.

[37] S. P. Martin, "A Supersymmetry primer," 1997. [Adv. Ser. Direct. High Energy Phys.18,1(1998)].

[38] P. Binetruy, *Supersymmetry: Theory, experiment and cosmology*. 2006.

[39] D. Feldman, G. Kane, E. Kuflik, and R. Lu, "A new (string motivated) approach to the little hierarchy problem," *Phys.Lett.*, vol. B704, pp. 56–61, 2011.

[40] W. de Boer, "Grand unified theories and supersymmetry in particle physics and cosmology," *Prog. Part. Nucl. Phys.*, vol. 33, pp. 201–302, 1994.

[41] G. Papadopoulos and P. Townsend, "Compactification of D = 11 supergravity on spaces of exceptional holonomy," *Phys.Lett.*, vol. B357, pp. 300–306, 1995.

[42] A. Brignole, L. E. Ibanez, and C. Munoz, "Soft supersymmetry breaking terms from supergravity and superstring models," 1997.

[43] C. Beasley and E. Witten, "A Note on fluxes and superpotentials in M theory compactifications on manifolds of G(2) holonomy," *JHEP*, vol. 0207, p. 046, 2002.

[44] T. Friedmann and E. Witten, "Unification scale, proton decay, and manifolds of G(2) holonomy," *Adv.Theor.Math.Phys.*, vol. 7, pp. 577–617, 2003.

[45] B. S. Acharya, "M theory, Joyce orbifolds and superYang-Mills," *Adv.Theor.Math.Phys.*, vol. 3, pp. 227–248, 1999.

[46] B. S. Acharya and E. Witten, “Chiral fermions from manifolds of G(2) holonomy,” 2001.

[47] I. Affleck, M. Dine, and N. Seiberg, “Dynamical Supersymmetry Breaking in Supersymmetric QCD,” *Nucl.Phys.*, vol. B241, pp. 493–534, 1984.

[48] B. S. Acharya and M. Torabian, “Supersymmetry Breaking, Moduli Stabilization and Hidden U(1) Breaking in M-Theory,” *Phys.Rev.*, vol. D83, p. 126001, 2011.

[49] D. Finnell and P. Pouliot, “Instanton calculations versus exact results in four-dimensional SUSY gauge theories,” *Nucl.Phys.*, vol. B453, pp. 225–239, 1995.

[50] L. Randall and R. Sundrum, “Out of this world supersymmetry breaking,” *Nucl. Phys.*, vol. B557, pp. 79–118, 1999.

[51] G. F. Giudice, M. A. Luty, H. Murayama, and R. Rattazzi, “Gaugino mass without singlets,” *JHEP*, vol. 12, p. 027, 1998.

[52] G. Kane, P. Kumar, and J. Shao, “CP-violating Phases in M-theory and Implications for EDMs,” *Phys. Rev.*, vol. D82, p. 055005, 2010.

[53] S. A. R. Ellis and G. L. Kane, “Theoretical Prediction and Impact of Fundamental Electric Dipole Moments,” *JHEP*, vol. 01, p. 077, 2016.

[54] K. Kadota, G. Kane, J. Kersten, and L. Velasco-Sevilla, “Flavour Issues for String-Motivated Heavy Scalar Spectra with a low Gluino Mass: the G2-MSSM Case,” *Eur. Phys. J.*, vol. C72, p. 2004, 2012.

[55] B. S. Acharya, K. Bobkov, and P. Kumar, “An M Theory Solution to the Strong CP Problem and Constraints on the Axiverse,” *JHEP*, vol. 11, p. 105, 2010.

[56] B. S. Acharya, P. Kumar, K. Bobkov, G. Kane, J. Shao, and S. Watson, “Non-thermal Dark Matter and the Moduli Problem in String Frameworks,” *JHEP*, vol. 06, p. 064, 2008.

[57] G. Kane, J. Shao, S. Watson, and H.-B. Yu, “The Baryon-Dark Matter Ratio Via Moduli Decay After Affleck-Dine Baryogenesis,” *JCAP*, vol. 1111, p. 012, 2011.

[58] B. S. Acharya, G. L. Kane, P. Kumar, R. Lu, and B. Zheng, “R-Parity Conservation from a Top Down Perspective,” 2014.

[59] J. Fan and M. Reece, “In Wino Veritas? Indirect Searches Shed Light on Neutralino Dark Matter,” *JHEP*, vol. 1310, p. 124, 2013.

[60] T. Cohen, M. Lisanti, A. Pierce, and T. R. Slatyer, “Wino Dark Matter Under Siege,” *JCAP*, vol. 1310, p. 061, 2013.

[61] B. S. Acharya, G. Kane, E. Kuflik, and R. Lu, “Theory and Phenomenology of μ in M theory,” *JHEP*, vol. 05, p. 033, 2011.

[62] G. Aad *et al.*, "Measurement of the Higgs boson mass from the $H \to \gamma\gamma$ and $H \to ZZ^* \to 4\ell$ channels with the ATLAS detector using 25 fb^{-1} of pp collision data," *Phys. Rev.*, vol. D90, no. 5, p. 052004, 2014.

[63] C. Collaboration, "Precise determination of the mass of the Higgs boson and studies of the compatibility of its couplings with the standard model," 2014.

[64] D. Feldman, G. Kane, E. Kuflik, and R. Lu, "A new (string motivated) approach to the little hierarchy problem," *Phys. Lett.*, vol. B704, pp. 56–61, 2011.

[65] B. S. Acharya, G. Kane, and E. Kuflik, "String Theories with Moduli Stabilization Imply Non-Thermal Cosmological History, and Particular Dark Matter," 2010.

[66] M. Papucci, K. Sakurai, A. Weiler, and L. Zeune, "Fastlim: a fast LHC limit calculator," *Eur. Phys. J.*, vol. C74, no. 11, p. 3163, 2014.

[67] B. C. Allanach, "SOFTSUSY: a program for calculating supersymmetric spectra," *Comput. Phys. Commun.*, vol. 143, pp. 305–331, 2002.

[68] M. Muhlleitner, A. Djouadi, and Y. Mambrini, "SDECAY: A Fortran code for the decays of the supersymmetric particles in the MSSM," *Comput. Phys. Commun.*, vol. 168, pp. 46–70, 2005.

[69] T. Moroi and L. Randall, "Wino cold dark matter from anomaly mediated SUSY breaking," *Nucl. Phys.*, vol. B570, pp. 455–472, 2000.

[70] B. S. Acharya, G. Kane, P. Kumar, R. Lu, and B. Zheng, "Mixed Wino-Axion Dark Matter in String/M Theory and the 130 GeV Gamma-line 'Signal'," 2012.

[71] J. Alwall, R. Frederix, S. Frixione, V. Hirschi, F. Maltoni, O. Mattelaer, H. S. Shao, T. Stelzer, P. Torrielli, and M. Zaro, "The automated computation of tree-level and next-to-leading order differential cross sections, and their matching to parton shower simulations," *JHEP*, vol. 07, p. 079, 2014.

[72] W. Beenakker, R. Hopker, and M. Spira, "PROSPINO: A Program for the production of supersymmetric particles in next-to-leading order QCD," 1996.

[73] W. Beenakker, R. Hopker, M. Spira, and P. M. Zerwas, "Squark and gluino production at hadron colliders," *Nucl. Phys.*, vol. B492, pp. 51–103, 1997.

[74] W. Beenakker, M. Klasen, M. Kramer, T. Plehn, M. Spira, and P. M. Zerwas, "The Production of charginos / neutralinos and sleptons at hadron colliders," *Phys. Rev. Lett.*, vol. 83, pp. 3780–3783, 1999. [Erratum: Phys. Rev. Lett.100,029901(2008)].

[75] T. Cohen, T. Golling, M. Hance, A. Henrichs, K. Howe, J. Loyal, S. Padhi, and J. G. Wacker, "SUSY Simplified Models at 14, 33, and 100 TeV Proton Colliders," *JHEP*, vol. 04, p. 117, 2014.

[76] G. L. Kane, A. A. Petrov, J. Shao, and L.-T. Wang, "Initial determination of the spins of the gluino and squarks at LHC," *J. Phys.*, vol. G37, p. 045004, 2010.

[77] H. Baer, V. Barger, A. Lessa, W. Sreethawong, and X. Tata, “Wh plus missing-ET signature from gaugino pair production at the LHC,” *Phys. Rev.*, vol. D85, p. 055022, 2012.

[78] T. Cohen, R. T. D’Agnolo, M. Hance, H. K. Lou, and J. G. Wacker, “Boosting Stop Searches with a 100 TeV Proton Collider,” *JHEP*, vol. 11, p. 021, 2014.

[79] M. Low and L.-T. Wang, “Neutralino dark matter at 14 TeV and 100 TeV,” *JHEP*, vol. 08, p. 161, 2014.

[80] S. Dawson, A. Ismail, and I. Low, “Redux on When is the top quark a parton?,” *Phys. Rev.*, vol. D90, no. 1, p. 014005, 2014.

[81] S. Jung and J. D. Wells, “Gaugino physics of split supersymmetry spectra at the LHC and future proton colliders,” *Phys. Rev.*, vol. D89, no. 7, p. 075004, 2014.

[82] B. S. Acharya, K. Boek, C. Pongkitivanichkul, and K. Sakurai, “Prospects for observing charginos and neutralinos at a 100 TeV proton-proton collider,” *JHEP*, vol. 02, p. 181, 2015.

[83] S. Gori, S. Jung, L.-T. Wang, and J. D. Wells, “Prospects for Electroweakino Discovery at a 100 TeV Hadron Collider,” *JHEP*, vol. 12, p. 108, 2014.

[84] J. Bramante, P. J. Fox, A. Martin, B. Ostdiek, T. Plehn, T. Schell, and M. Takeuchi, “Relic neutralino surface at a 100 TeV collider,” *Phys. Rev.*, vol. D91, p. 054015, 2015.

[85] G. Grilli di Cortona, “Hunting electroweakinos at future hadron colliders and direct detection experiments,” *JHEP*, vol. 05, p. 035, 2015.

[86] A. Berlin, T. Lin, M. Low, and L.-T. Wang, “Neutralinos in Vector Boson Fusion at High Energy Colliders,” *Phys. Rev.*, vol. D91, no. 11, p. 115002, 2015.

[87] H. Beauchesne, K. Earl, and T. Grgoire, “LHC constraints on Mini-Split anomaly and gauge mediation and prospects for LHC 14 and a future 100 TeV pp collider,” *JHEP*, vol. 08, p. 117, 2015.

[88] J. D. Wells, “Implications of supersymmetry breaking with a little hierarchy between gauginos and scalars,” in *11th International Conference on Supersymmetry and the Unification of Fundamental Interactions (SUSY 2003) Tucson, Arizona, June 5-10, 2003*, 2003.

[89] A. Arvanitaki, N. Craig, S. Dimopoulos, and G. Villadoro, “Mini-Split,” *JHEP*, vol. 02, p. 126, 2013.

[90] I. Hinchliffe, A. Kotwal, M. L. Mangano, C. Quigg, and L.-T. Wang, “Luminosity goals for a 100-TeV pp collider,” *Int. J. Mod. Phys.*, vol. A30, no. 23, p. 1544002, 2015.

[91] S. Profumo and C. E. Yaguna, “Gluino coannihilations and heavy bino dark matter,” *Phys. Rev.*, vol. D69, p. 115009, 2004.

[92] J. Ellis, F. Luo, and K. A. Olive, “Gluino Coannihilation Revisited,” *JHEP*, vol. 09, p. 127, 2015.

[93] P. Fayet, “MASSIVE GLUINOS,” *Phys. Lett.*, vol. B78, p. 417, 1978.

[94] P. J. Fox, A. E. Nelson, and N. Weiner, “Dirac gaugino masses and supersoft supersymmetry breaking,” *JHEP*, vol. 08, p. 035, 2002.

[95] G. Aad *et al.*, “Search for charginos nearly mass degenerate with the lightest neutralino based on a disappearing-track signature in pp collisions at $\sqrt(s)$=8TeV with the ATLAS detector,” *Phys. Rev.*, vol. D88, no. 11, p. 112006, 2013.

[96] G. Bertone, D. Hooper, and J. Silk, “Particle dark matter: Evidence, candidates and constraints,” *Phys. Rept.*, vol. 405, pp. 279–390, 2005.

[97] E. W. Kolb and M. S. Turner, “The Early Universe,” *Front. Phys.*, vol. 69, pp. 1–547, 1990.

[98] B. S. Acharya, G. Kane, S. Watson, and P. Kumar, “A Non-thermal WIMP Miracle,” *Phys.Rev.*, vol. D80, p. 083529, 2009.

[99] F. Denef and M. R. Douglas, “Distributions of nonsupersymmetric flux vacua,” *JHEP*, vol. 0503, p. 061, 2005.

[100] M. Gomez-Reino and C. A. Scrucca, “Locally stable non-supersymmetric Minkowski vacua in supergravity,” *JHEP*, vol. 0605, p. 015, 2006.

[101] N. Blinov, J. Kozaczuk, A. Menon, and D. E. Morrissey, “Confronting the Moduli-Induced LSP Problem,” 2014.

[102] A. L. Erickcek and K. Sigurdson, “Reheating Effects in the Matter Power Spectrum and Implications for Substructure,” *Phys.Rev.*, vol. D84, p. 083503, 2011.

[103] B. Fields and S. Sarkar, “Big-Bang nucleosynthesis (2006 Particle Data Group mini-review),” 2006.

[104] J. Lesgourgues, “Neutrino Cosmology from Planck 2014.” `http://www.cosmos.esa.int/documents/387566/387653/Ferrara_Dec4_11h50_Lesgourgues_NeutrinosReview.pdf`.

[105] G. F. Giudice, E. W. Kolb, and A. Riotto, “Largest temperature of the radiation era and its cosmological implications,” *Phys.Rev.*, vol. D64, p. 023508, 2001.

[106] D. J. H. Chung, E. W. Kolb, and A. Riotto, “Production of massive particles during reheating,” *Phys.Rev.*, vol. D60, p. 063504, 1999.

[107] C. Cheung, G. Elor, L. J. Hall, and P. Kumar, "Origins of Hidden Sector Dark Matter I: Cosmology," *JHEP*, vol. 1103, p. 042, 2011.

[108] M. Cicoli, J. P. Conlon, and F. Quevedo, "Dark radiation in LARGE volume models," *Phys.Rev.*, vol. D87, no. 4, p. 043520, 2013.

[109] T. Higaki and F. Takahashi, "Dark Radiation and Dark Matter in Large Volume Compactifications," *JHEP*, vol. 1211, p. 125, 2012.

[110] V. Khachatryan *et al.*, "Search for decays of stopped long-lived particles produced in proton-proton collisions at $\sqrt{s} = 8$ TeV," 2015.

[111] J. Fan, O. zsoy, and S. Watson, "Nonthermal histories and implications for structure formation," *Phys.Rev.*, vol. D90, no. 4, p. 043536, 2014.

[112] A. Loeb and M. Zaldarriaga, "The Small-scale power spectrum of cold dark matter," *Phys.Rev.*, vol. D71, p. 103520, 2005.

[113] J. L. Feng, M. Kaplinghat, H. Tu, and H.-B. Yu, "Hidden Charged Dark Matter," *JCAP*, vol. 0907, p. 004, 2009.

[114] F.-Y. Cyr-Racine, R. de Putter, A. Raccanelli, and K. Sigurdson, "Constraints on Large-Scale Dark Acoustic Oscillations from Cosmology," *Phys.Rev.*, vol. D89, no. 6, p. 063517, 2014.

[115] R. Schmidt and J. Wambsganss, "Limits on machos from microlensing in the double quasar q0957+561," *Astron.Astrophys.*, vol. 335, p. 379, 1998.

[116] J. Chen and S. M. Koushiappas, "Gravitational Nanolensing from Subsolar Mass Dark Matter Halos," *Astrophys.J.*, vol. 724, pp. 400–410, 2010.

[117] S. Baghram, N. Afshordi, and K. M. Zurek, "Prospects for Detecting Dark Matter Halo Substructure with Pulsar Timing," *Phys.Rev.*, vol. D84, p. 043511, 2011.

[118] T. Oda, T. Totani, and M. Nagashima, "Gamma-ray background from neutralino annihilation in the first cosmological objects," *Astrophys.J.*, vol. 633, pp. L65–L68, 2005.

[119] P. Scott and S. Sivertsson, "Gamma-Rays from Ultracompact Primordial Dark Matter Minihalos," *Phys.Rev.Lett.*, vol. 103, p. 211301, 2009.

[120] N. Afshordi, R. Mohayaee, and E. Bertschinger, "Hierarchy in the Phase Space and Dark Matter Astronomy," *Phys.Rev.*, vol. D81, p. 101301, 2010.

[121] H. de Vega, P. Salucci, and N. Sanchez, "The mass of the dark matter particle from theory and observations," *New Astron.*, vol. 17, pp. 653–666, 2012.

[122] M. R. Lovell, V. Eke, C. S. Frenk, L. Gao, A. Jenkins, *et al.*, "The Haloes of Bright Satellite Galaxies in a Warm Dark Matter Universe," *Mon.Not.Roy.Astron.Soc.*, vol. 420, pp. 2318–2324, 2012.

[123] H. de Vega and N. Sanchez, “Dark matter in galaxies: the dark matter particle mass is about 7 keV,” 2013.

[124] M. Viel, J. Lesgourgues, M. G. Haehnelt, S. Matarrese, and A. Riotto, “Constraining warm dark matter candidates including sterile neutrinos and light gravitinos with WMAP and the Lyman-alpha forest,” *Phys.Rev.*, vol. D71, p. 063534, 2005.

[125] X.-l. Chen, M. Kamionkowski, and X.-m. Zhang, “Kinetic decoupling of neutralino dark matter,” *Phys.Rev.*, vol. D64, p. 021302, 2001.

[126] S. Hofmann, D. J. Schwarz, and H. Stocker, “Damping scales of neutralino cold dark matter,” *Phys.Rev.*, vol. D64, p. 083507, 2001.

[127] R. Allahverdi, M. Cicoli, B. Dutta, and K. Sinha, “Nonthermal dark matter in string compactifications,” *Phys.Rev.*, vol. D88, no. 9, p. 095015, 2013.

[128] Y. Hochberg, E. Kuflik, T. Volansky, and J. G. Wacker, “Mechanism for Thermal Relic Dark Matter of Strongly Interacting Massive Particles,” *Phys.Rev.Lett.*, vol. 113, p. 171301, 2014.

[129] B. S. Acharya, S. A. R. Ellis, G. L. Kane, B. D. Nelson, and M. J. Perry, “The lightest visible-sector supersymmetric particle is likely to be unstable,” 2016.

[130] G. F. Giudice and A. Masiero, “A Natural Solution to the mu Problem in Supergravity Theories,” *Phys. Lett.*, vol. B206, pp. 480–484, 1988.

[131] D. M. Pierce, J. A. Bagger, K. T. Matchev, and R.-j. Zhang, “Precision corrections in the minimal supersymmetric standard model,” *Nucl. Phys.*, vol. B491, pp. 3–67, 1997.

[132] G. F. Giudice and A. Strumia, “Probing High-Scale and Split Supersymmetry with Higgs Mass Measurements,” *Nucl. Phys.*, vol. B858, pp. 63–83, 2012.

[133] P. Draper, G. Lee, and C. E. M. Wagner, “Precise Estimates of the Higgs Mass in Heavy SUSY,” 2013.

[134] T. Sjostrand, S. Mrenna, and P. Z. Skands, “PYTHIA 6.4 Physics and Manual,” *JHEP*, vol. 05, p. 026, 2006.

[135] A. Avetisyan *et al.*, “Methods and Results for Standard Model Event Generation at $\sqrt{s} = 14$ TeV, 33 TeV and 100 TeV Proton Colliders (A Snowmass Whitepaper),” in *Community Summer Study 2013: Snowmass on the Mississippi (CSS2013) Minneapolis, MN, USA, July 29-August 6, 2013*, 2013.

[136] J. de Favereau, C. Delaere, P. Demin, A. Giammanco, V. Lematre, A. Mertens, and M. Selvaggi, “DELPHES 3, A modular framework for fast simulation of a generic collider experiment,” *JHEP*, vol. 02, p. 057, 2014.

[137] J. Anderson *et al.*, "Snowmass Energy Frontier Simulations," in *Community Summer Study 2013: Snowmass on the Mississippi (CSS2013) Minneapolis, MN, USA, July 29-August 6, 2013*, 2013.

[138] E. Conte, B. Fuks, and G. Serret, "MadAnalysis 5, A User-Friendly Framework for Collider Phenomenology," *Comput. Phys. Commun.*, vol. 184, pp. 222–256, 2013.

[139] J. Fan, D. Krohn, P. Mosteiro, A. M. Thalapillil, and L.-T. Wang, "Heavy Squarks at the LHC," *JHEP*, vol. 03, p. 077, 2011.

[140] K. Jedamzik, "Big bang nucleosynthesis constraints on hadronically and electromagnetically decaying relic neutral particles," *Phys.Rev.*, vol. D74, p. 103509, 2006.

[141] L. J. Hall, K. Jedamzik, J. March-Russell, and S. M. West, "Freeze-In Production of FIMP Dark Matter," *JHEP*, vol. 1003, p. 080, 2010.